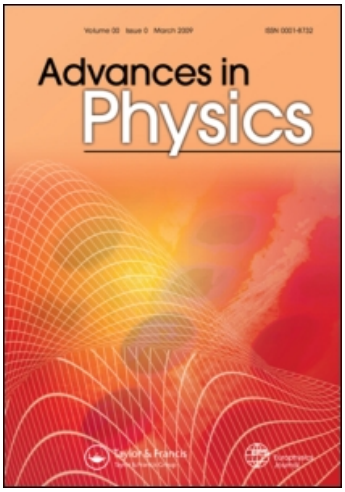

Advances in Physics
Publication details, including instructions for authors and subscription information:
http://www.informaworld.com/smpp/title~content=t713736250

Quantum computing by optical control of electron spins

Ren-Bao Liu[a]; Wang Yao[b]; L. J. Sham[c]
[a] Department of Physics, The Chinese University of Hong Kong, Hong Kong, China [b] Department of Physics and Center for Theoretical and Computational Physics, The University of Hong Kong, Hong Kong, China [c] Department of Physics, University of California San Diego, USA, La Jolla, CA 92093-0319, USA

First published on: 11 August 2010

To cite this Article Liu, Ren-Bao , Yao, Wang and Sham, L. J.(2010) 'Quantum computing by optical control of electron spins', Advances in Physics, 59: 5, 703 — 802, First published on: 11 August 2010 (iFirst)
To link to this Article: DOI: 10.1080/00018732.2010.505452
URL: http://dx.doi.org/10.1080/00018732.2010.505452

Advances in Physics
Vol. 59, No. 5, September–October 2010, 703–802

Taylor & Francis
Taylor & Francis Group

REVIEW ARTICLE

Quantum computing by optical control of electron spins

Ren-Bao Liu[a]*, Wang Yao[b] and L.J. Sham[c]

[a]*Department of Physics, The Chinese University of Hong Kong, Hong Kong, China;* [b]*Department of Physics and Center for Theoretical and Computational Physics, The University of Hong Kong, Hong Kong, China;* [c]*Department of Physics, University of California San Diego, USA, La Jolla, CA 92093-0319, USA*

(*Received 26 June 2009; final version received 29 June 2010*)

We review the progress and main challenges in implementing large-scale quantum computing by optical control of electron spins in quantum dots (QDs). Relevant systems include self-assembled QDs of III–V or II–VI compound semiconductors (such as InGaAs and CdSe), monolayer fluctuation QDs in compound semiconductor quantum wells, and impurity centres in solids, such as P-donors in silicon and nitrogen-vacancy centres in diamond. The decoherence of the electron spin qubits is discussed and various schemes for countering the decoherence problem are reviewed. We put forward designs of local nodes consisting of a few qubits which can be individually addressed and controlled. Remotely separated local nodes are connected by photonic structures (microcavities and waveguides) to form a large-scale distributed quantum system or a quantum network. The operation of the quantum network consists of optical control of a single electron spin, coupling of two spins in a local nodes, optically controlled quantum interfacing between stationary spin qubits in QDs and flying photon qubits in waveguides, rapid initialization of spin qubits and qubit-specific single-shot non-demolition quantum measurement. The rapid qubit initialization may be realized by selectively enhancing certain entropy dumping channels via phonon or photon baths. The single-shot quantum measurement may be *in situ* implemented through the integrated photonic network. The relevance of quantum non-demolition measurement to large-scale quantum computation is discussed. To illustrate the feasibility and demand, the resources are estimated for the benchmark problem of factorizing 15 with Shor's algorithm.

Keywords: quantum computing; quantum dot; spin; optical control

Contents PAGE

*Corresponding author. Email: rbliu@cuhk.edu.hk

ISSN 0001–8732 print/ISSN 1460–6976 online

DOI: 10.1080/00018732.2010.505452
http://www.informaworld.com

1. Introduction

On the basis of the quantum parallelism rooted in the superposition principle of quantum mechanics, quantum computers are expected to dramatically outperform their classical counterpart, particularly with exponential speedup in solving some hard problems such as factoring [1]. Towards the ambitious realization of practical quantum computation, such as factoring a million-bit number, enormous efforts are still to be put on both the design and invention of software (quantum algorithms) and the hardware development (physical implementation). Here we are mostly interested in the latter part. In principle, all quantum systems (which arguably amount to all physical systems) could be considered for the physical realization. But certain qualifications (such as the DiVincenzo criteria [2]) are to be fulfilled for them to be brought into consideration. Still there is a vast range of systems in the candidate pool, including nuclear spins in liquids [3–7], trapped ions or atoms [8–18], atoms in optical lattices [19–24], photons [25–34], superconducting circuits [35–55], electrons suspended over liquid helium surfaces [56–59], molecular magnets [60], nuclear spins in solids [61,62], electron spins in semiconductor quantum dots (QDs) [63–79], hole spins in QDs [80,81], electron spins in impurity centres in semiconductors, such as phosphorus donors in silicon [82–86] and nitrogen-vacancy (NV) centres in diamond [87–100], and non-Abelian anyon excitations in quantum matters with topological orders [101–105]. Here we concentrate on solid-state systems, and in particular on electron spins in semiconductors, while nuclear spins therein are also considered either as an adverse noise source or as a beneficial information storage [106,107]. Electrical, magnetic and/or optical means may be employed to access and/or manipulate the spins. In this review, we discuss the optical operations which may be applied to electron spins in III–V compound semiconductors where the direct bandgaps facilitate controllable optical transitions.

We shall not give an overall review of different schemes under current investigation for quantum computation. A comprehensive review of progresses and challenges in research of different systems may be found, e.g. in the Quantum Computation Roadmap published by Quantum Institute, LANL. It, however, would be useful to have a perspective of the position and connections of the systems under

review in the global picture of quantum computation research. As compared with their 'soft' counterparts, such as trapped atoms or ions, cavity-trapped or flying photons, electrons floating on liquid helium surfaces, and nuclear spins in liquids, the 'hard' solid-state systems as candidates for quantum computers have the advantages of stability and integratability, but have the disadvantages of relatively short coherence time due to interactions with complex environments in solids. The solid-state systems under current investigation include superconducting circuits, nuclear spins in solids and electron spins in semiconductors. While the qubits in superconducting circuits are made of excitations with macroscopic coherence in superconductors under designed confinement, nuclear or electron spins are natural qubit carriers since the information can be encoded in an intrinsic degree of freedom of elementary particles and thus are very stable. For example, while a superconducting qubit may be lost during the measurement and control processes, a spin qubit would always exist unless the hosting particle, such as a nucleus or an electron disappears (by decay, ionization, thermal activation, etc.). Also, a spin does not feel an electrical field directly, which makes spins less vulnerable than superconducting qubits to charge or current noises from environments or operating devices. The decoherence of spin qubits may be caused by coupling to other environmental spins, local magnetic field fluctuations or phonon scattering via spin–orbital interaction, all of which are usually rather weak in semiconductors. So the coherence time of spins are usually very long at low temperature and under a moderately strong magnetic field, varying from microseconds to milliseconds for electron spins (excluding the inhomogeneous broadening effect) [108–111], and longer than seconds for nuclear spins [112–115]. The weak coupling of spins to environments, of course, has also detrimental effects – the control, initialization and measurement of spins are all challenging tasks. In this regard, electron spins are more tractable than nuclear spins. Nuclear spins have longer coherence memory time but slow operating rate and low detection efficiency. Electron spins are relatively more controllable but less resilient to decoherence. Schemes have been pursued to combine the advantages of the two kinds of systems by using nuclei as storage [106,107,116] and electrons as operating units and interfaces [117]. The coupling between nuclear and electron spins is the hyperfine interaction. The hyperfine interaction is a main mechanism causing electron spin decoherence, but it can also be utilized to realize coupled qubit systems.

Electron spin qubits can be formed in various structures, such as doped electrons in QDs and impurities in solids. The fabrication of such systems with designed patterns and structures is possible because of the advances in modern semiconductor technologies and nano-technologies – compatibility with the modern semiconductor industry is an extra advantage of using electron spins as qubits in quantum computation. The direct pump, control and probe of electron spins may be done by electron spin resonance techniques with microwave pulses [88,110,111,117]. For faster operation clock as desired, the electron spin states may be converted to other degrees of freedom through quantum interfacing (the same as one does from nuclear spin states to electron spin states). Then electron spins may be accessed indirectly by control of agents, such as excitons in semiconductors and photons generated by

recombination of excitons [64,68–79,118–120]. Quantum interfacing between spins and photons [119] also makes possible quantum communication between distributed quantum nodes which is required for scalable quantum computation. In this sense, the direct-gap semiconductors, such as InAs and GaAs, where ultrafast optical control and interfacing are possible, have some advantages over the indirect gap materials, such as silicon, where electrical gating and microwave pulses may be the only possible means of control. As compared with silicon, a main concern with the III–V materials is the much shorter spin coherence time due to the abundance of nuclear spins as noisy environments (in GaAs, e.g. the electron spin coherence time is in the order of microseconds, while in silicon, it is in milliseconds, excluding the effects of phonon scattering and inhomogeneous broadening) [121–132]. Fortunately, there already exist various schemes to elongate the spin coherence time by orders of magnitude, via dynamical control [130,133–142], or nuclear state preparation [113–115,143–151].

All these said, we would like to remark that at this point, it would be premature to discourage effort in exploring different physical systems, existing or emerging. It is conceivable that the future quantum computers will be realized by combination of innovative technologies, ideas, concepts, and synthesis of materials and systems. For instance, the idea of topological quantum computation may be implemented with trapped atoms in optical lattice [152]; the systems under the focus of this review involve both stationary electron spins and flying photons [119], which may also be applied to coupled systems of photons and superconducting qubits [47,49–51]; semiconductor chips may provide microtrap for ions; photon-based quantum computation may use quantum lights from trapped ions [153], atoms [154,155], or QDs [156,157] and so on. In the present initial stage of quantum computation technology, it would be highly risky to exclude certain candidates just because of difficulties encountered in the beginning of the adventure, since different systems may have their bottleneck problems at different stages. In particular, solid-state systems, while promising with their large-scale stability and integratability in the future, are still facing severe obstacles of environmental noise and control errors for one or a few qubits. In this review, based on many experimentally demonstrated elements and theoretically proposed schemes, we would like to put forward blue prints of relatively large-scale quantum computing via optical control of electron spins in QDs. We should point out that such targets are by no means easy and still require significant advances of technologies and concepts. Also, although our discussions, to be specific, will be based on electron spins in InAs or GaAs QDs, the schemes with certain modifications, can be applied to a few emerging novel systems, such as hole spins in QDs and NV centres in diamond, where the physics is similar to electron spins in QDs.

There are two main concerns with solid-state systems for quantum computation, when compared with their atomic peers like trapped ions or atoms. One is how to fabricate and construct a large array of reproducible or identical qubit units (such as QDs). And the other one is the many-body problem.

The fabrication issue is even worse for the systems to be discussed in this review, namely QDs under optical control. Most likely, the QDs are formed by molecular

beam epitaxy (MBE) growth process, such as the self-assembled QDs and the fluctuation QDs. Effort is being made on growth process so well-controlled that all the QDs are almost identical and regularly located. There are also such promising systems as impurities in semiconductors, such as phosphorus donors in silicon [83] and NV centres in diamond [158,159] where the nanometre-precision ion implantation technology may allow a patterned array of qubits represented by the electron spins in the impurity centres. In the foreseeable future, however, we may have to live with the problem of the irregularity. On the positive side, we could take advantage of the irregularity produced by the system fabrication. In small systems for demonstration purposes, the varying size and position of QDs may be used as fingerprints by which different qubits may be addressed and individually controlled by light beams which usually have resolution no better than half the wavelength.

The many-body problem raises two related questions: Can an isolated qubit be properly defined at all among so many particles, and will a coherent superposition state of a qubit last long enough for quantum gates before it collapses due to decoherence in the noisy environment?

It turns out [160] that large gaps between valence bands and conduction bands in semiconductors protect elementary excitations, such as excitons and electrons so well that an extra electron doped in a QD is well-defined as a single particle moving with a renormalized effective mass and coupling constants, such as the g-factor, in analogy to a low-energy electron in the Dirac sea. The protective gap sets a fundamental limit on the operation speed of quantum computation in solid systems. Such a limit is far from being approached in current experiments, whether in typical semiconductors where the gap is about 1 eV (for fs-order operation time) or a few millielectron volts in superconductors.

In optical control of spins in QDs, decoherence is caused mainly by three mechanisms, namely coupling to nuclear spins of the host lattice [108,121–132,161], phonon scattering [162–168] and spontaneous photon emission during the optical control [68,169]. For some pseudo-spin qubits with orbital-state dependence (such as the singlet–triplet qubits [108]), the charge fluctuation may also contribute to the environment noise [170,171]. Besides the standard quantum error correction protocols [172], there are specific strategies to deal with various decoherence mechanisms, which are needed anyway to achieve fidelity of quantum gates above the threshold for quantum error correction. The spontaneous photon emission could

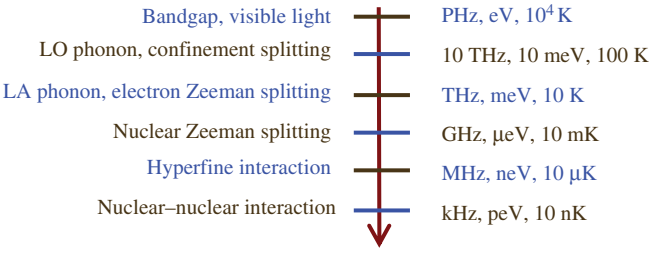

Figure 1. Relevant energy scales for a typical GaAs semiconductor QD, in terms of frequency, energy and temperature. The hyperfine constant refers to the interaction between a single nucleus and an electron.

be suppressed by completing the optical control rapidly or via off-resonance (virtual) excitation [68,72,76,173]. The phonon scattering may be quenched simply by lowering the temperature to a few kelvins [162–165,174–177] or by using light-element materials, such as diamond [87–100] or organic materials [178,179], where the spin–orbital coupling is weak. The nuclear spins, being a slow bath, may have their decoherence controlled by certain dynamical decoupling or disentanglement control [130,133–142]. Again, the normally harmful noise sources could be made useful by design. The photon and phonon baths are rapid entropy dumping pools when certain quantum channels are selectively enhanced [120]. The photon emission, when enhanced by cavities and guided by quantum channels, is an important basis for quantum communication between remotely separated qubits [76,119]. The nuclear spins, having very slow dynamics, are considered as good local quantum memories [106,107,116] with an electron spin in contact acting as a mediator for quantum information operation and transfer.

To achieve large-scale quantum computation, consensus has been reached on several criteria to be fulfilled, known as the 'DiVincenzo criteria' [2]. We quote these criteria below as the guidelines for reviewing the progresses and main challenges towards the realization of quantum computation by optical control of electron spins in QDs:

(1) a scalable physical system with well-characterized qubits;
(2) the ability to initialize the state of the qubits to a simple fiducial state;
(3) long relevant decoherence times, much longer than the gate operation time;
(4) a universal set of quantum gates;
(5) a qubit-specific measurement capability;
(6) the ability to interconvert stationary and flying qubits and
(7) the ability faithfully to transmit flying qubits between specified locations.

The stationary qubits under our focus are well-defined by electron spins in QDs, and the flying qubits carrying quantum information between distributed nodes are photons flying in waveguides. We will discuss in more detail the decoherence of the spin qubits and show that the decoherence time ($\sim 10^{-6}$ s in a typical GaAs QD with the inhomogeneous broadening excluded [108,109,115,147,180,181]) is indeed much longer than the quantum gate operation time ($\sim 10^{-11}$ s [79,181,182]). The one- and two-qubit gates, which form a universal set [172,183,184], are realized by optical excitation of charged excitons. Some fundamental physics issues with the initialization and quantum measurement of qubits will be reviewed. Measurement and initialization are put together because they are related to the same physical process. Initialization disposes of entropy to the environment while in measurement the environment acts as part of a readout device. For a large-scale quantum computation blueprint, we use designs of local nodes of a few qubits and structures of distributed nodes connected by quantum channels which may be realized by photonic elements, such as waveguides and microcavities. Control schemes of quantum interfacing are also an important topic to be covered. To illustrate the feasibility and demands of the quantum computation in the discussed systems, the resources, in terms of the number of optical pulses and operation time (compared with the spin decoherence time), will be estimated for the benchmark problem of factoring 15 with Shor's algorithm.

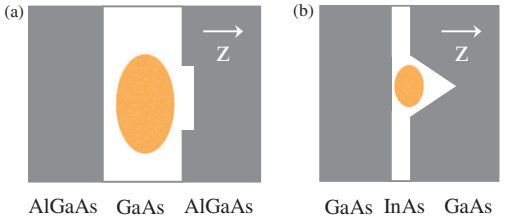

Figure 2. Illustration of two types of optically controllable QDs. The arrows indicate the growth direction. The ellipse regions show schematically the confinement of electrons in the dots. (a) A GaAs fluctuation QD. (b) An InAs self-assembled QD.

2. Spin qubits in QDs

In this section, we begin (in Section 2.1) with a brief review of the confinement of single electrons in optically controllable semiconductor QDs, followed (in Section 2.2) by discussions of QD energy level structures and optical properties. In Section 2.3, we briefly outline recent theoretical and experimental results on the spin coherence properties of single electrons confined in QDs. Both theories and experiments show that, as phonon mechanisms are suppressed at low temperature (~4 K and below), lattice nuclear spins become the dominant cause for the electron spin decoherence. In Section 2.4, we review the theory of electron spin decoherence by interacting nuclear spins in a QD. Coherence protection of electron spin in the interacting nuclear spin bath is possible by applying a sequence of π pulses to the electron, as discussed in Section 2.5. In Section 2.6, an overview of QD electron spins as qubits is given from the perspective of fault-tolerance requirement for scalable quantum computation, and two other promising spin qubit systems, namely hole spins and NV centre spins, are also discussed.

2.1. *Confinement of a single electron in a QD*

Two types of MBE grown QDs formed in direct bandgap III–V compounds offer a great deal of controllability by ultrafast optics and are being investigated as building blocks for optically manipulated quantum computers.

The first is referred to as interface fluctuation formed QDs in GaAs/AlGaAs quantum well structures [185–193]. We will refer them in short as GaAs fluctuation QDs. As illustrated in Figure 2(a) and 3, an electron in such a structure is confined in the growth direction along the z-axis in a low bandgap GaAs layer, with a thickness of tens of Å, between two higher bandgap $Al_xGa_{1-x}As$ layers. In the III–V materials, the conduction band minimum occurs at the Γ point in the momentum space and the heterostructure wavefunction of the electron is constructed from the conduction band Bloch functions in the vicinity of the Γ point. Thus, the difference in energy of the conduction band minimum in the high- and low-bandgap materials form a square well potential for electron in the growth direction. The band discontinuity in the interface of the low and high bandgap materials is typically hundreds of millielectron volts so that the vertical confinement is strong.

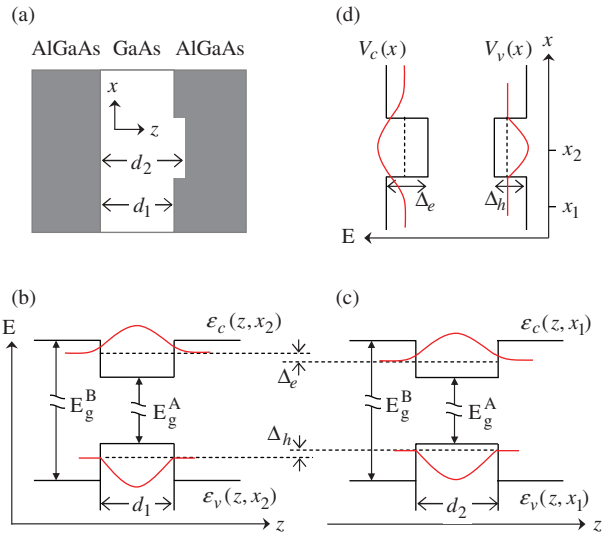

Figure 3. Schematics of the three-dimensional confinement of electrons and holes in a GaAs fluctuation QD. (a) Interface fluctuation, typically of one monolayer, forms a fluctuation dot. The bright region is the GaAs material and the dark regions are AlGaAs. (b) Vertical confinement for electrons and holes in the growth direction (the z-direction) at $x = x_1$ where the quantum well is thinner $d = d_1$. (c) Vertical confinement in the growth direction at $x = x_2$ where the quantum well is one monolayer thicker $d = d_2$. (d) The difference of the energy lift by vertical confinement in regions of different thickness forms a lateral confinement for the electrons and holes.

Growth interruption leads to roughness at the material interfaces, usually a thickness fluctuation of one monolayer. Electron confinement within the plane of the quantum well (in the x and y directions) is caused by the quantum well thickness fluctuation. The energy lift by the quantum confinement in the z-direction is roughly $\frac{\hbar^2}{2m^*}(\frac{\pi}{d})^2$ for the lowest energy state, where m^* is the effective mass of conduction electron and d is the quantum well thickness. This energy lift is larger where the quantum well is thinner. Therefore, lateral confinement is formed where the quantum well has an island. Figure 3 shows schematically how monolayer-size fluctuation in a quantum well gives rise to the localized envelope function in the plane. The energy scale of this lateral confinement is typically of several to tens of millielectron volts in GaAs fluctuation dot. A GaAs fluctuation dot with lateral size ~40 nm can hold several localized energy levels with level spacing of several millielectron volts.

The second type of QDs, referred as InAs self-assembled dots, are formed using the Stranski–Krastanow growth mode which utilizes the strain caused by the lattice mismatch between InAs layers and GaAs substrates. InAs self-assembles into islands which are primarily in the shape of a pyramid (see Figure 2b), with a height of tens of Ångstroms and a base size of tens of nanometres [196–199]. In an InAs self-assembled QD, the lateral confinement is much stronger due to the pyramid structure, and the smaller dot size leads to level spacing of ~10 meV or larger.

For a GaAs fluctuation QD, a single conduction band electron can be incorporated in the dot by modulation Si doping in the barriers [200]. For an

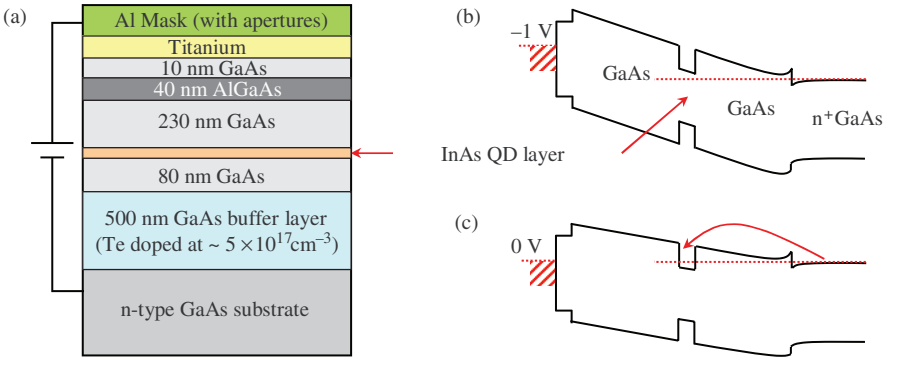

Figure 4. Gate controlled charging of an InAs self-assembled QD in an n^+-intrinsic-Schottky (NIS) diode structure. (a) Schematic illustration of the NIS diode structure given in [194,195]. (b) Band diagram of the NIS diode structure where the InAs QD is uncharged. (c) An InAs QD charged with a single electron.

InAs self-assembled dot, gate voltage tuning in an NIS diode structure is a more controllable way to charge and discharge the QD with a single electron [194,195] (see the schematic illustration in Figure 4). The qubit is typically encoded in the spin subspace of the lowest energy level of the single electron in the QD.

There are other notable systems where single electrons are localized in nanoscale regions in semiconductors. These include the confinement by electric gates on top of two-dimensional electron gas in GaAs [63,201,202], and the localization by impurities, such as phosphorus donors in silicon [82–86] or NV centres in diamond [88,92–98,100,117,203,204]. The spins of single electrons localized in these systems are also under extensive investigation as qubit carriers.

2.2. *Energy levels in a charged QD*

Control of a spin qubit makes use of a larger Hilbert space in a QD, involving optical transitions from valance bands to conduction bands. In this section, we briefly describe the relevant energy level structures and the corresponding optical transition selection rules.

A direct interband transition creates an additional electron in the conduction band by leaving a hole in the valance band. At the Γ point, the fourfold degeneracy of the bulk Γ_8 valance band is lifted by the quantum well confinement effect. The top valance subband is a doublet derived from the $J_z = \pm 3/2$ bulk band, which is also denoted as the 'heavy hole' (HH) band (see Appendix A). Other valance bands are irrelevant in our control schemes as they are always far off-resonance. Electrons can be excited from the valance band states of angular momentum J_z to conduction band states of spin S_z by absorbing a photon, with the selection rule $S_z = J_z + \sigma$ where $\sigma = \pm 1$ corresponds to the circular polarization of light. Therefore, the single electron states are optically coupled to the charged exciton states (also known as trion states) composed of two conduction electrons and one HH. Figure 5 shows schematically two different types of trion states. The two electrons in Figure 5(a) occupy different electronic levels of the QD and the two electrons in Figure 5(b) are

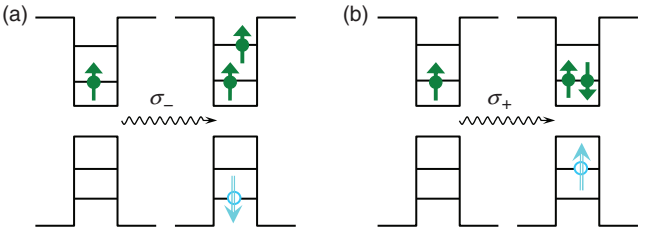

Figure 5. Schematic illustration of the creation of trion states in a QD. The QD initially holds a single conduction band electron with spin up in the lowest state of the confinement potential. (a) By the Pauli exclusion principle, a $\sigma-$ circularly polarized light can create an additional exciton to a higher excited state of the QD. (b) $\sigma+$ polarized light can create the lowest energy trion state with two electrons forming a singlet and a hole in the spin up state.

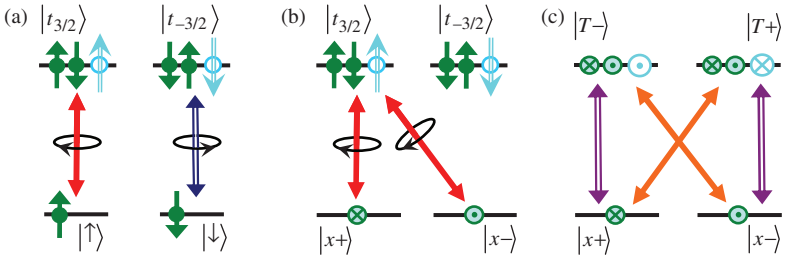

Figure 6. Optical transition selection rules in a QD illustrated in various basis sets. (a) The basis is the eigenstates of $\hat{J}_z$. The solid two-headed arrow denotes σ_+ polarized light and the hollow two-headed one σ_- polarized light. (b) The two electron spin states are transformed to the basis in the x-direction: $|x\pm\rangle \equiv (|\uparrow\rangle \pm |\downarrow\rangle)/\sqrt{2}$. The solid two-headed arrow denotes σ_+ polarized light. (c) The two trion states are also transformed to the basis in the x-direction: $|T\pm\rangle \equiv (|t_{\frac{3}{2}}\rangle \pm ||t_{-\frac{3}{2}}\rangle)/\sqrt{2}$. Here, the hollow two-headed arrow denotes X-polarized light and the solid one Y-polarized light.

in a spin singlet configuration on the same electronic level. The energy spacing between different trion configurations is ~1–10 meV depending on the QD size. The bandwidth and Rabi frequency of the optical field is much smaller than this energy spacing. So when the frequency of the optical field is near the resonance of one type of trion configuration, the remaining trion configurations can be neglected.

Most manipulation schemes use the ground state trions (Figure 5b) to mediate optical control of the spin. In such cases, the relevant Hilbert space is composed of the two single electron spin states and the two ground state trions (Figure 6). For simplicity, we use below the $e^\dagger_\pm$ to denote the creation of a conduction band electron of $S_z = \pm 1/2$ in the lowest energy level of the QD and similarly $h^\dagger_\pm$ to denote the creation of a HH with $J_z = \pm 3/2$ (annihilation of an electron with $J_z = \mp 3/2$). The relevant Hilbert space for optical control of spin is: $|\uparrow\rangle \equiv e^\dagger_+|G\rangle$, $|\downarrow\rangle \equiv e^\dagger_-|G\rangle$, $|t_{\frac{3}{2}}\rangle \equiv e^\dagger_+ e^\dagger_- h^\dagger_+|G\rangle$ and $|t_{-\frac{3}{2}}\rangle \equiv e^\dagger_+ e^\dagger_- h^\dagger_-|G\rangle$ where $|G\rangle$ denotes the configuration with empty conduction bands and full valence bands. The transition selection rule between these four states is shown in Figure 6(a). For different control schemes, the selection rules represented in other basis sets are also useful. In Figure 6(b) and (c),

we have changed the basis for the spin states and the trion states so that the electron spin states are eigenstates along the x-direction and the trion states are $|T\pm\rangle \equiv \left(|t_{3/2}\rangle \pm |t_{-3/2}\rangle\right)/\sqrt{2}$. The selection rule can also be represented with the linearly polarized basis for the optical field as shown in Figure 6(c) [118]. The selective coupling of the QD transitions with light of different polarizations offers sufficient freedom for optical control of the spin. Depending on the polarization and frequency of the optical field, various optical pathways can be established to realize the control in the spin subspace via a second-order process through the trion. For example, if the optical field is σ_+ circularly polarized (Figure 6b), the $|t_{-\frac{3}{2}}\rangle$ trion state is decoupled from optical field and the relevant dynamics is in a Λ-type three-level system. Raman processes in such three-level systems are central to the optical control of spin dynamics as will be discussed in detail later.

2.3. *Spin relaxation and decoherence in QDs*

Coherence properties of qubits are crucial to quantum information processing. Spin decoherence of a single electron in a solid results from the coupling to various environmental modes. Typical optical manipulations of spin qubits in QDs are performed in the Voigt or Faraday geometry with a strong magnetic field (~1–10 T), and at low temperature (~ or <K) to suppress thermal excitations in the environment [205,206]. In this section, we single out the environmental effects that dominate the spin decoherence under these experimental conditions.

We first show the quantum mechanics of decoherence due to the coupling to a general environment [207–209]. The initial state of the electron spin, $|\varphi^s(0)\rangle = C_+|+\rangle + C_-|-\rangle$, is prepared as a coherent superposition of the spin up and down states $|\pm\rangle$ in an external magnetic field. The state of the total system of the spin plus bath at that instant forms an *unentangled* state, $|\Psi(0)\rangle = |\varphi^s(0)\rangle \otimes |\mathcal{J}\rangle$. It evolves over time t to $|\Psi(t)\rangle = C_+(t)|+\rangle \otimes |\mathcal{J}^+(t)\rangle + C_-(t)|-\rangle \otimes |\mathcal{J}^-(t)\rangle$ where the bath states $|\mathcal{J}^+(t)\rangle$ and $|\mathcal{J}^-(t)\rangle$ are generally different. The mixed state of the electron spin is determined by its reduced density matrix obtained by tracing over the environment states $\rho^s_{\sigma,\sigma'}(t) = C^*_{\sigma'}(t)C_\sigma(t)\langle\mathcal{J}^{\sigma'}(t)|\mathcal{J}^\sigma(t)\rangle$. The diagonal element of the reduced density matrix $\rho^s_{\sigma,\sigma'}$ gives the probability of finding the spin in state $|\sigma\rangle$. Either off-diagonal element is a measure of the spin phase coherence. The environment-driven transfer of the probability between the spin states is known as the longitudinal relaxation, while the loss of the off-diagonal element is known as the transverse decoherence. The longitudinal relaxation also contributes to the transverse decoherence. The spin decoherence without longitudinal relaxation is called pure dephasing, characterized by the quantity $\langle\mathcal{J}^+(t)|\mathcal{J}^-(t)\rangle$. Pure dephasing is thus a consequence of system-bath entanglement when the bath evolution $|\mathcal{J}^\pm(t)\rangle$ is conditioned on the system states $|\pm\rangle$. The above discussion can be generalized to the situation where the environment is initially in a mixed state. The single electron plus its environment is then described at the initial time by the density matrix $\rho(0) = |\varphi^s(0)\rangle\langle\varphi^s(0)| \otimes \sum_{\mathcal{J}} P_{\mathcal{J}}|\mathcal{J}\rangle\langle\mathcal{J}|$, where the reduced density matrix for the electron at any moment is $\rho^s_{\sigma,\sigma'}(t) = \sum_{\mathcal{J}} P_{\mathcal{J}} C^*_{\sigma'}(t)C_\sigma(t)\langle\mathcal{J}^{\sigma'}(t)|\mathcal{J}^\sigma(t)\rangle$.

Novel experimental techniques have been developed in the past several years for measurement of the spin relaxation and decoherence in QDs. In GaAs fluctuation dots and InAs self-assembled QDs, optical techniques are commonly used for

measuring the spin T_1 time. These include the time domain measurement by optical generation and detection of non-equilibrium spin population [176], and the frequency domain approach of the coherent phase-modulation spectroscopy [177]. In gate-defined QDs, spin-to-charge conversion can be implemented to trace the time evolution of the initially created spin population [174,175]. In strong magnetic field of ~1–10 T and at low temperature ($\lesssim$1 K), the experimentally measured value $T_1 \sim 10^{-4}$–10^{-2} s [174–177] are in good agreement with the theoretical predictions of the spin longitudinal relaxation induced by phonon [162–165]. In a recent experiment by Amasha *et al.* [210], spin relaxation rate of a single electron in a lateral QD is studied when the orbital wavefunction is manipulated using gate voltages. The measured dependence of T_1 on orbital confinement and magnetic field is in excellent agreement with theory [163,166], which confirms that phonon scattering in the presence of spin-orbit coupling is the dominant cause for spin relaxation in magnetic field down to 1 T. In low magnetic field and when spin-orbit coupling strength is weak, T_1 as long as 1 s is observed [210].

Transverse decoherence may be measured in optically accessible QDs by the frequency domain approach utilizing the Hanle effect [112], or by the time domain pump-probe measurement. In the later approach, a circularly polarized pump pulse initiates spin polarization in the growth direction, whose precession about an in-plane magnetic field is tracked by the differential transmission of a circularly polarized probe beam [205] or the Faraday rotation angle of a linearly polarized probe beam [211]. In a gate-defined double-dot structure, the spin-to-charge conversion process can also be implemented to probe the relative coherence between states of a coupled spin pair, which provides information about the decoherence of a single spin [202,212]. In these experiments, transverse decoherence times of $T_2^* \sim 1-10$ ns were obtained either from measurements on spatial ensembles of QDs [205,211,213] or from time-ensemble measurements of single dots [112,202,212]. Spin echo type of measurement was also performed on the gate-defined single GaAs dot [108,180], which showed an echo decay time of $T_H \sim \mu$s. The sharp difference between T_H and T_2^* suggests that the ensemble dephasing is mainly affected by the inhomogeneous broadening of the local environment of the QDs, which is removed in the spin echo measurement. Greilich *et al.* [109] have shown that by using a periodic train of circularly polarized light pulses to excite an ensemble of InAs self-assembled QDs, spin polarization is amplified only in a subset of the ensemble where the electron spin Zeeman frequency has to be an integer multiple of the pulse repetition frequency. These quasi-discrete spectra lead to constructive interference of the spin precession at each pulse arrival time. As dephasing by inhomogeneous broadening is thus removed, single spin $T_2 \sim \mu$s is obtained [109,124,146,150,151]. Very recently, Hahn echo measurement was also made possible for impurity spins in GaAs where rotations of spins were achieved by ultrafast optical pulses [181]. The measured Hahn echo decay time is 6 μs, consistent with theories and other experiments.

All these experiments show that transverse decoherence times (T_2^*, T_H and T_2) are orders of magnitude faster than the longitudinal relaxation time T_1. On the other hand, theoretical analysis of the phonon mechanisms concludes that pure dephasing due to phonon is well suppressed at the temperature where these experiments are performed ($\lesssim$1 K) [166,167]. As phonon is unlikely to be responsible for the observed

fast transverse decoherence, the remaining possibility is then the nuclear spins sitting on the lattice sites which are coupled to the electrons through the hyperfine interaction [108,121–127,129–132,134,161,214].

2.4. *Decoherence by an interacting nuclear spin bath*

In this section, we discuss the effects of the lattice nuclear spins on the electron spin coherence. In the relevant III–V materials, all stable isotopes have non-zero nuclear spins. The nuclear magneton is about 3 orders of magnitude smaller than the electron Bohr magneton. A strong magnetic field of 10 T only results in a nuclear Zeeman energy of $\sim$mK, much smaller than the experimentally achievable temperatures in cryostats ($\sim$4 K) or even in dilution refrigerators ($\gtrsim$50 mK) (see Figure 1). Therefore, coupling to a thermalized nuclear spin bath will be an inevitable source of decoherence for quantum computation in III–V materials. As the longitudinal spin relaxation of the electron is found to be much slower than the transverse decoherence, we will focus on the pure dephasing of electron spins. In this section, we set the z-direction along the direction of the external magnetic field.

2.4.1. *Single electron in a mesoscopic bath of interacting nuclear spins*

In III–V semiconductors, the electron spin is coupled to the lattice nuclear spins through the contact hyperfine interaction. The averaged magnitude of the coupling to a nucleus is inversely proportional to the total number N of nuclei in the QD. For QDs of all practical sizes ($N \sim 10^5$–10^7), this hyperfine coupling is much stronger ($\sim$MHz) than the mutual interactions between the nuclear spins ($\lesssim$kHz). Therefore, a mesoscopic bath consisting of all nuclear spins within the QD (i.e. in direct contact with the single electron) can be identified (Figure 7) [130]. The coupling between the mesoscopic bath and nuclei outside the boundary can be neglected since such dynamics occurs in a much slower timescale as compared with the electron spin decoherence caused by the mesoscopic bath. The decoherence problem can then be solved by considering the quantum dynamics of the coupled mesoscopic system of electron and nuclear spins. The assumption that this mesoscopic system is well isolated from the back ground lattice has been confirmed in numerical studies where the boundary of the mesoscopic bath is systematically extended and the electron spin coherence shows fast convergence [130]. The nuclear spin bath is typically of a randomized configuration as schematically illustrated in Figure 7 since the experimentally achievable temperature is always much higher than the nuclear Zeeman energy.

We briefly describe below the key ingredients for electron spin decoherence in the high field limit with details given in Appendix B. By the diagonal part of the electron–nuclear hyperfine interaction, the electron Zeeman energy is conditioned on the nuclear spin states (Figure 8a). In a QD ensemble, the different nuclear spin configurations for each ensemble member lead to inhomogeneous broadening of the Overhauser field for the electron spin. This is the dominant cause of ensemble dephasing in the timescale of T_2^* which is inversely proportional to the inhomogeneous broadening. Nuclear–nuclear interactions become relevant due to the non-uniform hyperfine coupling strength between the electron and different nuclear spins.

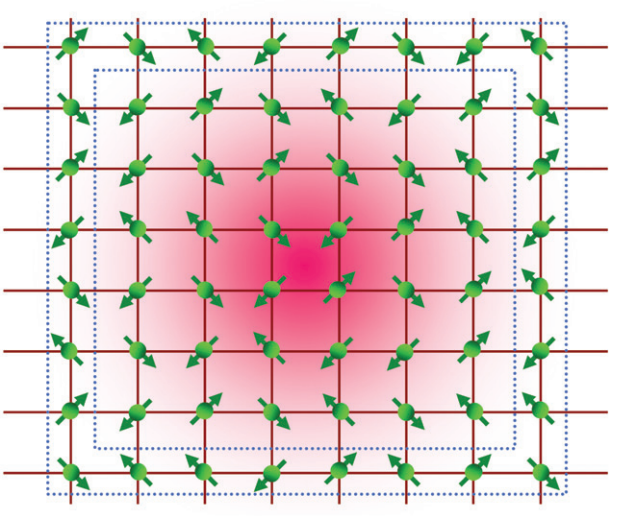

Figure 7. Schematics of an electron (the shadow) and one layer of lattice nuclear spins in a QD. The two boxes in dotted lines indicate two possible choices of boundary of the mesoscopic nuclear spin bath, which are relatively arbitrary due to the interaction between nuclei within and without the boundary. When the hyperfine interaction dominates over the nuclear spin interaction, such arbitrariness has negligible effects on calculation of the electron spin decoherence as long as all the nuclei in direct contact with the electron spin have been enclosed.

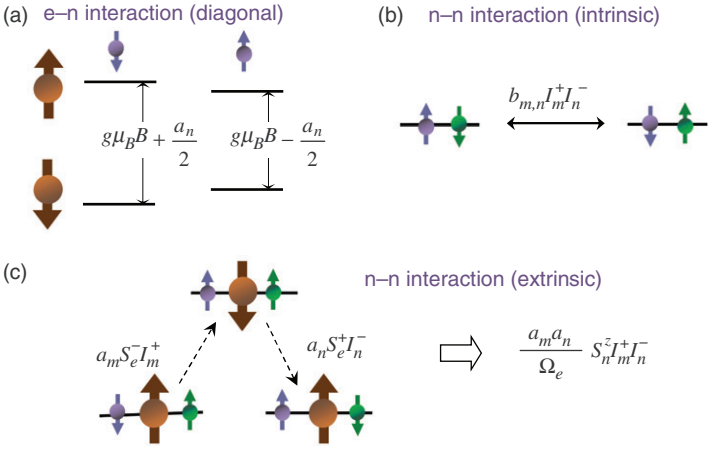

Figure 8. Nuclear spin processes relevant for electron spin decoherence. (a) By the diagonal part of electron nuclear hyperfine interaction (which involves only the spin vector components along the field z-direction), the electron Zeeman energy depends on the nuclear configuration. (b) Nuclear pair-wise flip-flop by the intrinsic nuclear interactions. (c) Nuclear pair-wise flip-flop mediated by two virtual flips of the electron spin, which results in an effective *extrinsic* nuclear interaction. Ω_e is the electron Zeeman energy in the external magnetic field, and a_n is the hyperfine interaction strength between the electron and the nth nuclear spin.

Pair-wise nuclear flip-flops can then lead to dynamical fluctuation of the nuclear Overhauser field (Figure 8b). This is the cause of single electron spin decoherence in the nuclear environment which begins with a pure state (referred as *single-system dynamics* hereafter). Electron–nuclear coupling also has an off-diagonal part which tends to cause flip-flop between the electron and a nuclear spin. Because the electron Zeeman energy is much larger than the strength of the hyperfine interaction, the real process of electron nuclear flip-flop is suppressed [124,127]. However, a second-order process which consists of two virtual flips of the single electron ends up as a flip-flop between two nuclear spins (Figure 8c). This effective nuclear interaction due to the single electron is designated as the *extrinsic* interaction [127,130,134], as opposed to the *intrinsic* nuclear interactions that exist in the semiconductor matrix, e.g. the dipole–dipole coupling and the indirect coupling mediated by virtual interband transitions via the hyperfine interaction [215–219].

The *extrinsic* nuclear interaction couples any two nuclear spins within the mesoscopic bath and is therefore infinitely ranged, i.e., throughout the entire mesoscopic region. By contrast, the *intrinsic* nuclear interaction is finite-ranged. For near neighbors, the intrinsic one is much stronger than the extrinsic one for the field strength under consideration. In addition, for the *extrinsic* nuclear interaction, the magnitude is inversely proportional to the external magnetic field and the sign is conditioned on the electron spin states.

2.4.2. *Nuclear spin pair-flip excitations and pair-correlation approximation*

From the quantum mechanical picture of decoherence (see Section 2.3), pure dephasing of a single quantum system is caused by the bifurcation of environmental evolution under the drive by different system states, or system-bath entanglement. Thus, the nuclear bath evolutions conditioned on different spin states of the electron are key to the solution of electron spin decoherence. The elementary excitations in the nuclear spin bath are pair-flip excitations as shown in Figure 8(b) and Figure 8(c). The flip-pairs are independent of each other if they are well-separated. For a typical QD with $N \sim 10^6$ nuclear spins, the number of pairs that can flip-flop in a random configuration is large. We have $O(N)$ local flip-pairs whose dynamics are dominated by the finite range *intrinsic* nuclear interactions, and $O(N^2)$ non-local flip pairs whose dynamics are dominated by the infinite range *extrinsic* nuclear interactions. On the other hand, the number of pair flips that can occur on the timescale of electron spin decoherence is negligibly small as compared with N. This is due to the slowness in the nuclear spin interacting dynamics. Thus, the probability of two pair flips occurring in the neighborhood of each other is negligibly small and pair flips as elementary excitations can be treated as independent of each other (see Appendix B for details). This approximation is further confirmed by the linked cluster expansion approach [129]. Independent pair-excitation approximation corresponds to keeping the lowest (second) order linked diagrams in the exponential factor. Higher order linked diagrams contain more nuclear interaction lines and are negligible in the relevant timescale because of the weakness of the nuclear interactions as compared with the electron–nuclear coupling. For long time evolution (such as for decoherence under pulse control) and for relatively small spin baths, higher order correlations would be important. The linked cluster

expansion would be increasingly inefficient for calculating higher order correlations. The density matrix cluster expansion is an alternative method which requires no evaluation of higher order Feynman diagrams and is thus quite convenient [220]. For small spin baths, however, it has been shown that the cluster expansion may not converge to the exact results [221]. For a systematic and accurate account of the higher order correlations in spin baths in the qubit decoherence problem, a cluster-correlation expansion method has been developed [221,222], which covers the valid ranges of all the methods mentioned above and in particularly produces the exact results even for a relatively small bath where the standard cluster expansion fails. The cluster correlation expansion is based on the factorization of the bath dynamics into non-factorizable correlations of certain groups of bath spins. The lowest order of the cluster correlation expansion coincides with the independent pair excitation approximation. We also note that recently the higher order effects of the hyperfine interaction (beyond the pair-excitation considered here) have also been considered for a relatively weak external magnetic field while the pure dephasing condition is still satisfied [132,214].

The evolution of independent pair correlations can be described using a geometric representation. A pair flip k can be mapped to a Bloch vector which precesses about a pseudo-field (Figure 9)

$$\mathbf{h}_k^{\pm} \equiv (\pm 2A_k + 2B_k, 0, \pm E_k), \tag{1}$$

where, for the electron spin state $|\pm\rangle$, $\pm A_k$ and B_k are the pair flip transition amplitudes contributed by the extrinsic nuclear interaction and the intrinsic nuclear interaction, respectively, and $\pm E_k$ is the energy cost of the pair flip contributed by the hyperfine interaction (see Appendix B). At the initial time when the electron spin coherence is prepared (see the general formulation of decoherence process in Section 2.3), the Bloch vector for each pair flip points in the pseudo $+z$ direction.

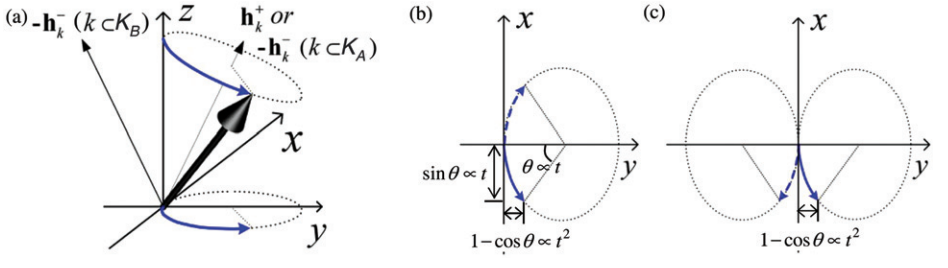

Figure 9. A geometric picture for understanding the free-induction decay (FID). (a) The evolution of pair-excitation illustrated by the rotation of a Bloch vector and the projected trajectory on the pseudo-x–y plane. Direction of the effective pseudo-field $\mathbf{h}_k^{\pm}$ are indicated for the set of non-local pairs K_A and the set of local pairs K_B, respectively. (b) The projection of the Bloch vector trajectories to the pseudo-x–y plane for pair-excitation driven by extrinsic nuclear interaction. The solid (dashed) line denotes the pair evolution conditioned on the electron spin state $|+\rangle$ ($|-\rangle$). As the rotation angle $\theta \propto t$, the distance between the conjugated vectors $\delta_k \propto t$ at short time. (c) The projection of the Bloch vector trajectories to the pseudo-x–y plane for pair-excitations driven by intrinsic nuclear interactions. The distance between the conjugated vectors $\delta_k \propto t^2$ at short time.

As the pseudo-field direction depends on the electron spin state $|\pm\rangle$, the pair evolution takes different trajectories conditioned on the electron spin state, and the distance δ_k (i.e. distinguishability) between the two separated trajectories turns out to be a measure of the electron spin decoherence,

$$\mathcal{L}^{s}_{+,-}(t) \approx \prod_k e^{-\delta_k^2/2}, \tag{2}$$

where $\mathcal{L}^{s}_{+,-}(t)$ is the ratio between the electron spin coherence at time t and at time 0 (see the general formulation of decoherence in Section 2.3). δ_k also quantifies the amount of entanglement between the electron spin and the kth flip pair. The electron spin decoherence is thus the consequence of the entanglement with the pair flip excitations in the interacting nuclear spin bath.

With single system dynamics solved for an arbitrary random configuration, ensemble dynamics is simply the statistical average of the single system dynamics with the nuclear bath initially in all possible configurations. As the number of flip pairs is large ($O(N)$ for local pairs and $O(N^2)$ non-local pairs), the central limit theorem of statistics leads to a factorized form for ensemble spin coherence,

$$\mathcal{L}_{+,-}(t) = \mathcal{L}^{\mathrm{s}}_{+,-}(t) \times \mathcal{L}^{(0)}_{+,-}(t), \tag{3}$$

where $\mathcal{L}^{s}_{+,-}(t)$ is the single-system decoherence in a typical configuration of the nuclear bath, and

$$\mathcal{L}^{(0)}_{+,-}(t) = \sum_{\mathcal{J}} P_{\mathcal{J}} e^{-i\phi_{\mathcal{J}}(t)}, \tag{4}$$

where $\phi_{\mathcal{J}}(t) = (\Omega_e + \mathcal{E}_{\mathcal{J}})t$ in free-induction decay (FID), and the summation runs over all possible nuclear configurations $\mathcal{J}$. Ω_e and $\mathcal{E}_{\mathcal{J}}$ are the electron Zeeman energy resulting from the external magnetic field and from the Overhauser field, respectively, with the latter dependent on the nuclear configuration $\mathcal{J}$. The ensemble effect resides entirely in the factor $\mathcal{L}^{(0)}_{+,-}(t)$, which may be read as the inhomogeneous broadening of the Overhauser field $\mathcal{E}_{\mathcal{J}}$ with a distribution function $P_{\mathcal{J}}$. The inhomogeneous broadening effect dominates the FID in the ensemble dynamics in the form of $\mathcal{L}^{(0)}_{+,-}(t) = e^{-i\Omega_e t - (t/T_2^*)^2}$, with the dephasing time $T_2^* \sim \sqrt{N}\mathcal{A}^{-1} \sim 10\,\mathrm{ns}$ as measured [112,121,124,202,205,212,223], where $\mathcal{A} \sim$ THz is the hyperfine constant of the material.

A sequence of π pulses can be applied to the electron spin to eliminate the effects of the inhomogeneous broadening [110,132,180,224]. In a general scenario where the electron spin is flipped at time $\tau_1, \tau_2, \ldots,$ and τ_n, respectively, we have $\phi_{\mathcal{J}}(t) = (\Omega_e + \mathcal{E}_{\mathcal{J}})\ [\tau_1 - (\tau_2 - \tau_1) + \cdots + (-1)^n(t - \tau_n)]$. When $\tau_1 - (\tau_2 - \tau_1) + \cdots + (-1)^n(t - \tau_n) = 0$ is satisfied, $\mathcal{L}^{(0)}_{+,-}(t) = 1$ and a spin echo is expected. The echo magnitude will be determined by the dynamical part $\mathcal{L}^{s}_{+,-}(t)$. Under the simplest scenario, a single π-pulse is applied at τ and a spin echo is expected at $t = 2\tau$, known as Hahn echo [225]. The spin echo profile, i.e. the echo magnitude $\mathcal{L}^{\mathrm{s}}_{+,-}(2\tau)$ as a function of the echo delay time 2τ, reveals the dynamical processes that leads to decoherence.

It is worth noting that the factorized form of the ensemble spin coherence, Equation (3), allows direct observation of single-system dynamics behavior $\mathcal{L}^{\mathrm{s}}_{+,-}(t)$

from a spatial ensemble measurement when dephasing by inhomogeneous broadening is removed at a general time t. For example, the mode locking experiment reported in [109,211] opens up such possibilities as discussed in Section 2.3, where the single spin T_2 (defined here as the FID timescale of $\mathcal{L}^{\mathrm{s}}_{+,-}(t)$) has been extracted from the experimental data.

2.4.3. *Timescales of single spin decoherence and ensemble spin echo decay*

In FID, the conjugate Bloch vectors precess along opposite directions for non-local pairs ($k \in K_A$), and symmetrically with respect to the pseudo-y–z plane for the near-neighbor pairs ($k \in K_B$) [Figure 9]. The decoherence can be readily grouped by the two different mechanisms as

$$\mathcal{L}^{\mathrm{s}}_{+,-} \cong \prod_{k\in K_B} e^{-\frac{t^4}{2}E_k^2 B_k^2 \mathrm{sinc}^4\frac{h_k t}{2}} \prod_{k\in K_A} e^{-2t^2 A_k^2 \mathrm{sinc}^2(h_k t)}, \tag{5}$$

where $h_k = |\mathbf{h}_k^{\pm}|$. We can see that the extrinsic hyperfine-mediated and the intrinsic couplings lead to the $e^{-(t/T_{2,A})^2}$ and the $e^{-(t/T_{2,B})^4}$ behaviors respectively, in time shorter than the inverse pair-flip energy cost (which corresponds to the width of the excitation spectrum),

$$T_{2,B} \approx b^{-1/2}\mathcal{A}^{-1/2}N^{1/4};\ \ T_{2,A} \approx \Omega_e \mathcal{A}^{-2}N, \tag{6}$$

where b is the typical value of near neighbor intrinsic nuclear coupling strength B_k (see Appendix B). The super-exponential decay behavior of the spin coherence indicates the strong non-Markovian characteristic of the bath dynamics in the short-time limit. In the long-time limit, the super-exponential decay will change to an exponential decay time, which indicates the onset of the Markovian dynamics [130,131,214]. The dynamics in the even longer time limit (which could occur, e.g., in a highly polarized spin bath), determined by the complex structure of the collective modes of the bath, is rather complicated, and power-law decays have been predicted [128,214].

Figure 10 shows the FID in single-system dynamics for a typical dot under various field strengths B_{ext}. The strong field dependence of T_2 demonstrates the significance of the extrinsic hyperfine mediated nuclear coupling up to a strong field ($\sim$10 T). The short-time e^{-t^2} behavior of decoherence by extrinsic nuclear interactions and the e^{-t^4} behavior by intrinsic nuclear interaction hold well within the relevant timescale for single spin FID. The field and dot-size dependence shown in Figure 11, by the intrinsic and extrinsic mechanisms, agrees well with the simple form given in Equations (5) and (6). For a small QD or in a small magnetic field, the extrinsic nuclear interaction dominates, while the intrinsic nuclear interaction dominates otherwise. When the two mechanisms are comparable, the single-system FID begins with the e^{-t^2} behavior and may cross over towards the e^{-t^4} decay as time increases (e.g., see the curve at $B_{\mathrm{ext}} = 12$ T in Figure 10b). The timescale of single spin FID ranges from 0.1 to 10 μs depending on the dot size and external magnetic field, which agrees well with the experimental observation of 3 μs by Greilich *et al*. [109].

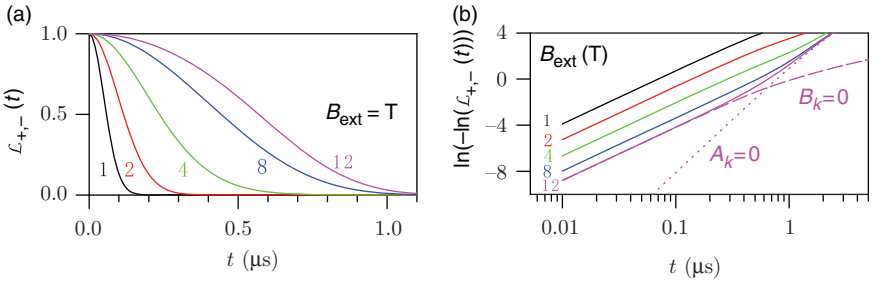

Figure 10. (a) Electron spin coherence as functions of time for various field strengths. (b) The logarithm plot of (a), in which the curve for $B_{ext} = 12\,T$ is compared with the contribution by the extrinsic nuclear interaction (- - -) and that by the intrinsic nuclear interaction (. . .), respectively. The size of the InAs dot is $33 \times 33 \times 3\,nm^3$ and the nuclear-spin initial state $|\mathcal{J}\rangle$ is randomly selected from an ensemble at temperature 1 K. The field strength is indicated by the numbers for each curve. (Adapted from R.B. Liu *et al.* New Journal of Physics, 9 (2007), p. 226 [130]. Copyright © 2007 by the Institute of Physics.).

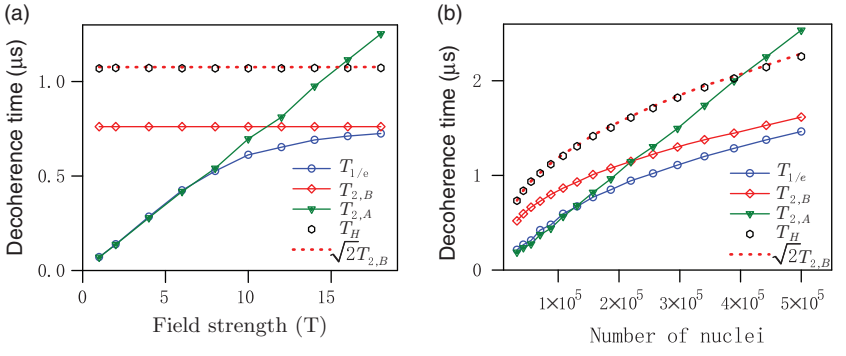

Figure 11. (a) Field dependence of decoherence times with the inhomogeneous broadening effect excluded. The QD is the same as in Figure 10 and the temperature is 1 K. (b) Dot-size dependence of decoherence times with the inhomogeneous broadening excluded. The QD size is varied with fixed width : depth : height ratio 33 : 33 : 6. The field strength is 10 T and the temperature is 1 K. $T_{1/e}$ (—○—) – time for FID to $1/e$ of its initial value, $T_{2,A}$ (—◇—) – FID decoherence time resulting solely from extrinsic hyperfine-mediated pair flips, $T_{2,B}$ (—▽—) – FID decoherence time resulting solely from the intrinsic nuclear spin interaction, and T_H (○) – decay time of the Hahn echo signal. The $\sqrt{2}T_{2,B}$ (- - -) is plotted to compare with the Hahn echo decay time (Adapted from R.B. Liu *et al.* New Journal of Physics, 9 (2007), p. 226 [130]. Copyright © 2007 by the Institute of Physics.).

In the spin echo scenario, as the electron spin is flipped by the π-pulse, the transition amplitude by extrinsic nuclear interaction A_k and the hyperfine energy cost E_k for each pair flip will change sign after the pulse. Thus, the pair-excitations by the extrinsic hyperfine-mediated nuclear coupling will reverse their precession after the pulse and return to the origin at $t = 2\tau$, disentangling the electron spin and the pair excitations (Figure 12a). So the decoherence driven by the extrinsic hyperfine-mediated coupling is largely eliminated in the spin echo configuration as shown by the calculation in Figure 13 [125,127]. For the pair-excitations driven by the intrinsic

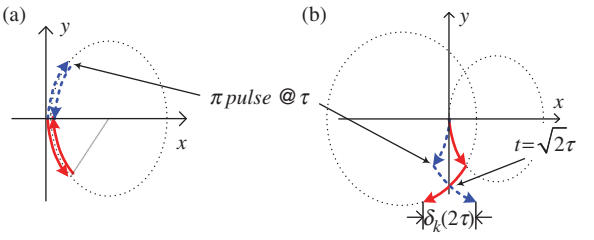

Figure 12. (a) and (b) Evolution of the pair-excitations under the single-pulse control, driven by the extrinsic and intrinsic nuclear spin interactions, respectively. The red solid (blue dashed) trajectories denote the pair evolutions conditioned on the electron spin state $|+\rangle$ ($|-\rangle$).

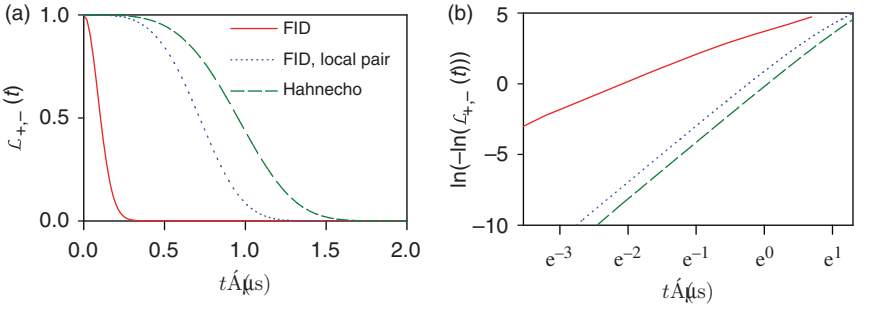

Figure 13. (a) Comparison of the Hahn echo (dashed green line) and the FID (solid red line) signals. The FID signal is also shown with the extrinsic hyperfine-mediated pair flips neglected (dotted blue line). (b) The logarithm plot of (a). The QD is as in Figure 10, with $B_{\text{ext}} = 2\,\text{T}$ (Adapted from R.B. Liu *et al.* New Journal of Physics, 9 (2007), p. 226 [130]. Copyright © 2007 by the Institute of Physics.).

coupling, the conjugate Bloch vectors will switch their precession axes which also reverse the entanglement to some extent but no full recovery is obtained at the echo time (Figure 12b). Finally, the electron spin coherence at the echo time is derived as,

$$\mathcal{L}_{+,-}(2\tau) \cong \prod_{k\in K_B} e^{-2\tau^4 E_k^2 B_k^2 \text{sinc}^4\left(h_k^B \tau/2\right)}. \tag{7}$$

Similar to the analysis for single system FID, the spin echo signal begins with the short-time behavior as $e^{-(2\tau/T_{\text{H}}^{\text{sh}})^4}$.

The ensemble spin echo profile is numerically calculated and compared with the single-system FID for a typical QD in Figure 13. While it has been a common practice to equal the spin echo decay time T_H to the single-system FID time T_2 [123,220], the two timescales can in fact be significantly different since the bath dynamics is modified by the pulse control of the electron spin. And the spin echo decay and the single-system FID follow different temporal behavior [Figure 13]. The spin echo decay time of μs from calculation [127,130] is in agreement with the Hahn echo measurements by Clark *et al.* [181] for impurity spins in GaAs and by Petta *et al.* [108] for gate-defined dot in GaAs.

2.5. *Coherence restoration and protection in the nuclear spin bath*

Protection of the electron spin coherence by active physical control is desired which can result in a better physical qubit before the informatic approaches of quantum error correction may be implemented. This is indeed possible for single electron spins in interacting nuclear spin baths.

By a sequence of π-rotations of the electron spin, the ensemble dephasing by inhomogeneous broadening as well as decoherence by *extrinsically* driven nuclear pair dynamics is efficiently removed at the classical spin echo time, as shown by the previous discussions. Nuclear pair dynamics driven by the *intrinsic* interactions is also affected by such control as shown in Figure 12(b): the two separated trajectories meet again sometime after the π-pulse. This intersection signals the disentanglement of the electron from the pair excitation. Surprisingly, even though different pair excitations have very different precession frequencies h_k, the trajectory separation δ_k is eliminated for all local pairs in the leading order of $B_k t$ at $t = \sqrt{2}\tau$. This leads to a recovery of the electron spin coherence as illustrated by numerical evaluation shown in Figure 14. Remarkably, even when the electron spin is flipped after the coherence has completely vanished in single-system dynamics, the coherence may be well-recovered at time $\sqrt{2}\tau$ whereas no coherence is visible at the conventional spin echo time 2τ [134]. Thus, in this context, the decay of Hahn echo does not mean the irreversible lost of coherence due to the nuclear interacting dynamics. It is simply because the classical spin echo time for phase refocusing in ensemble does not respect the quantum behavior of the interacting dynamics in a mesoscopic bath. When the extrinsic nuclear interaction is significant, the $\sqrt{2}\tau$ echo can also be weakened by the non-local pair dynamics (Figure 14).

The $\sqrt{2}\tau$ coherence echo is observable when the ensemble factor $\mathcal{L}^{(0)}_{+,-}$ has a timescale longer or comparable to the single spin T_2 time. This is possible with the narrowing of inhomogeneous distribution by nuclear state preparation [113–115,143–151] (see Section 2.6). Furthermore, the unusual echo at $\sqrt{2}\tau$ turns out to have a more general occurrence in other echo processes. Months after its first prediction [130,134], such echo behavior is observed in NMR experiments in a ^{3}He gas undergoing Brownian motion in a magnetic field gradient [226].

Disentanglement from bath could be the guiding principle for coherence protection with reduced overhead when the bath dynamics is more or less understood. In the present case of protecting electron spin from the nuclear spin bath, we need a pulse sequence to produce a time where the decoherence from all three sources can be removed. We give here a solution which is a two-pulse control. Figure 14(c) shows that, after a second π pulse at 3τ, the two conjugated paths corresponding to the electron $|\pm\rangle$ states, driven by the intrinsic nuclear interaction, cross-again at 4τ, coinciding with the secondary spin echo time for the other two causes. The electron spin is thus disentangled from the entire nuclear spin bath to the leading order at $t = 4\tau$ (see numerical evaluation in Figure 14b).

The power of concatenation design of pulse sequences has been shown in the context of dynamical decoupling of quantum systems from baths [133]. Similarly, the control of quantum system for disentanglement from the bath may be enhanced by concatenation design. We notice that the pair evolution with the two-pulse control of the electron spin can be constructed recursively from the free-induction evolution

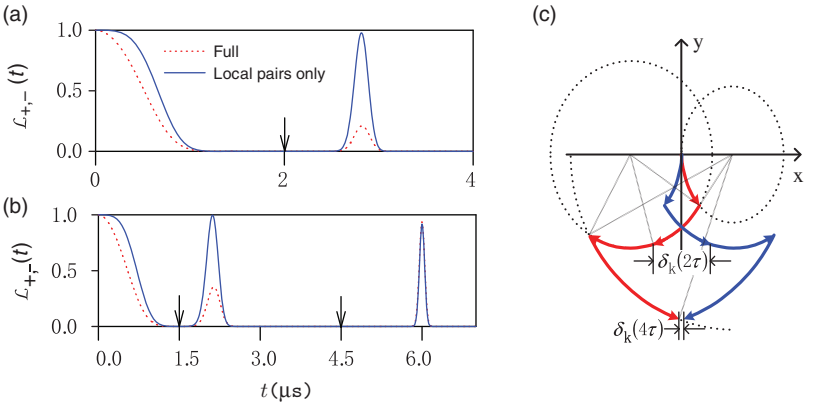

Figure 14. (a) The electron spin coherence under the control of a short π-pulse applied at $\tau = 2\,\mu s$ (when the FID signal has vanished), the recoherence at $\sqrt{2}\tau$ is pronounced while no signal survives at the echo-time 2τ. (b) The electron spin coherence under the control of a Carr–Purcell pulse sequence. The arrows indicate positions of the π pulses. The solid blue (dotted red) lines are calculated with (without) including the extrinsic hyperfine-mediated pair flips. The QD is the same as in Figure 10 with $B_{ext} = 10\,T$. Inhomogeneous broadening is excluded. (c) The projection of the Bloch vector trajectories to the pseudo-x-y plane for intrinsically driven pair-excitations under the 2-pulse Carr–Purcell control (Adapted from R.B. Liu *et al.* New Journal of Physics, 9 (2007), p. 226 [130]. Copyright © 2007 by the Institute of Physics) (Adapted from W. Yao *et al.*, Physical Review Letters 98 (2007), p. 077602 [134]. Copyright © 2007 by the American Physical Society.).

$\hat{U}_0^{\pm}$, by the concatenation, $\hat{U}_l^{\pm} = \hat{U}_{l-1}^{\mp}\hat{U}_{l-1}^{\pm}$, $l = 1, 2$ [130,134]. The process can be extended by iteration to any level as shown in Figure 15(c). Disentanglement from local and non-local pair dynamics both occur at $\tau_l \equiv 2^l\tau$ coinciding with the classic spin echo. The decoherence is reduced by an order of $b^2\tau_l^2$ at τ_l for each additional level of concatenation till saturation at the level $l_0 \approx -\log_2(b\tau)$ [130]. Hence, the coherence echo magnitude scales with the echo delay time according to $\exp(-(\tau_l/T_l)^{2l+2})$ as shown in Figure 15(b), suggesting that short-time decoherence can be arbitrarily suppressed with additional levels of concatenation. Numerical calculation further shows that a proper level of concatenation allows the protection of electron spin coherence by pulse sequences with interpulse interval as large as ~μs (Figure 15a).

The concatenated control of the decoherence can also be optimized in terms of the number of pulses so that the control errors due to imperfections in the controlling pulses is minimized. The invention of the pulse sequences with the minimum possible number of pulses to suppress the short-time decoherence to a given order of the pulse delay time is due to Uhrig [139] in considering the qubit decoherence in a non-interacting boson bath. Later, the Uhrig decoherence control was conjectured [140] and proved [141] to be universal regardless of the bath Hamiltonian. The Uhrig pulse sequences may also be interlaced with the concatenated pulse sequences not only the pure dephasing for control but also the longitudinal spin relaxation [142,227]. All these advances help to clear the obstacle of the qubit decoherence in solid environment.

2.6. *Summary: QD opportunity*

The three-dimensional confinement in QDs leads to the quantized electronic and excitonic energy levels. As a consequence, a QD resembles an atom in terms of the discrete energy levels with long coherence times and well-defined optical transition selection rules, although it is essentially a mesoscopic system. The atom-like electronic and optical properties have been well-established by experiments in the past decades [199,200,205,206,213,228–230], including the initial demonstration of quantum coherent control [231–236].

Experiments also showed that, for single electrons in QDs, spin polarization along an external magnetic field can be preserved for a sufficiently long time ($T_1 \sim 20$ ms reported for InAs self-assembled dot [176]). A major concern has been the inevitable cause of transverse decoherence by the lattice nuclear spins in III–V materials. Due to the extremely small energy scales even in a strong magnetic field, the nuclear spin bath is of high entropy at experimentally achievable temperature. Ensemble dephasing time $T_2^* \sim 1-10$ ns in different types of QDs [112,202], spin echo decay time T_H in the order of μs in gate-defined QDs [108,161] and for impurity spins in GaAs [181], and single spin dephasing time $T_2 \sim 3$ μs in self-assembled QDs [109] have been extracted from various experimental approaches, all in agreement with the theoretical analysis of nuclear spin baths [127,130,237]. As compared with the spin echo decay, FID in single-system dynamics is subject to the additional cause of decoherence from the extrinsic mechanism, which is dependent on the external magnetic field. In a moderate field of 1 T, $T_2 \sim 100$ ns by theory [127,130] is an order smaller than the spin echo decay time. Polarization of the nuclear spin bath can partially suppress this decoherence channel [128,206,238]. However, a substantial increase of electron spin coherence time would require a nuclear polarization over

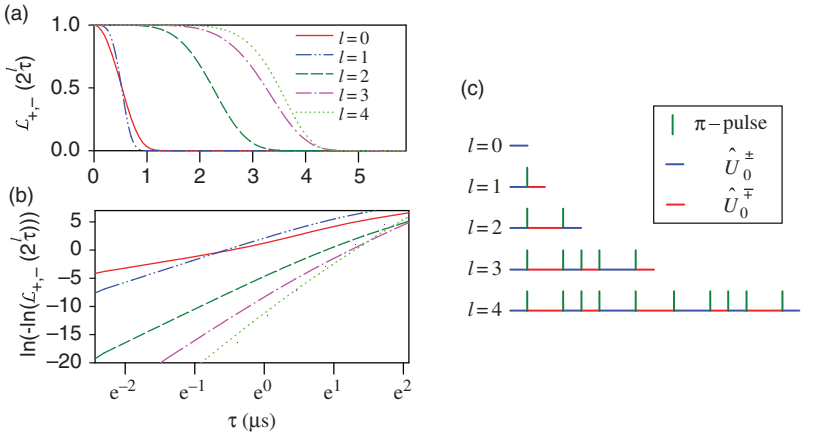

Figure 15. (a) The electron spin coherence under the lth order concatenation control, $l=0,\ldots,4$, as functions of the pulse delay time τ. (b) The logarithm plot of (a). The QD is the same as in Figure 10 with $B_{\text{ext}}=10$ T. Ensemble average is taken at $T=1$ K. (c) Concatenated sequences of π-pulses flipping the electron spin, represented by vertical bars. (Adapted from R.B. Liu *et al.* New Journal of Physics, 9 (2007), p. 226 [130]. Copyright © 2007 by the Institute of Physics.).

99%, which can be extremely difficult. Current experimental capability on nuclear spin polarization in III–V QDs is in the order of 10–70% [112,239–243].

For spin qubits used as quantum memory, dynamical decoupling schemes can be used to decouple system and environment for coherence protection [133,244–247], which typically requires frequent manipulations of the spin qubits. As compared with these schemes designed to deal with a general environment, the available solution to the dynamics of the nuclear spin bath makes possible a different approach aiming at disentanglement of the system from the bath only (their decoupling is a sufficient but not necessary condition for disentanglement) [130,134]. Numerical calculations on realistic QD systems show that designed sequence of π-pulses on the electron can efficiently preserve its spin coherence up to $\sim$100 μs in both single-system and ensemble dynamics. As the interval between adjacent pulses can be as long as microsecond, this disentanglement approach not only substantially reduces the overhead but also avoids the problem of unwanted heating of the system from the frequent manipulations required by the dynamical decoupling schemes.

In the quantum logic control of the spin qubit, T_2^* is the shortest timescale one encounters. Even with the ultrafast optical manipulation timescale $T_{\mathrm{op}} \sim 10$ ps, $T_2^* \sim 1-10$ ns from FID in a thermal nuclear spin bath is not sufficient to satisfy the current fault-tolerant threshold $T_{\mathrm{coh}}/T_{\mathrm{op}} \sim 10^3$–$10^4$ [248–253]. Considering the efficiency of spin echoes in eliminating the dephasing by inhomogeneous broadening, the combination of the desired control action with these coherence protect operations could offer a promising route towards fault-tolerant quantum information processing. Efforts are being devoted towards the search of universal logic control strategies of coherence protected qubits [246].

An alternative approach is to pre-prepare the nuclear spin bath so that the nuclear field inhomogeneous broadening can be squeezed below its thermal value, as suggested by the various nuclear state preparation schemes [114,143–145,148–151]. The resultant enhancement on the T_2^* time can last for seconds or even longer as nuclear spin relaxation is extremely slow. For optically controllable electron spin in self-assembled dot, enhancement of T_2^* up to microsecond by nuclear state preparation has been achieved experimentally for a spin ensemble [146], and very recently for a single spin [147]. For electrically controllable spin qubits, enhancement of T_2^* of a coupled spin pair to microsecond was also reported in a double-dot configuration [115].

When the inhomogeneous broadening effect is suppressed (by spin echo or bath state preparation), dephasing by nuclear interacting dynamics is the limiting factor. Experiments [109] and theories [130] show that, in FID, $T_2 \sim 0.1$–10 μs for typical self-assembled QDs under a moderate magnetic field, which is sufficiently long to satisfy the fault-tolerant threshold. And the spin coherence time can be still elongated further by dynamical decoupling.

As an alternative, the HH spin in a positively charged QD can also play the role of a qubit carrier. For the *p*-type hole bands, the contact hyperfine interaction vanishes and the hole spin is coupled to nuclear spins through the dipolar hyperfine interaction. Theoretical studies shows that the hole–nuclear hyperfine coupling strength is about one order weaker than the electron–nuclear hyperfine coupling [80,81]. Furthermore, unlike the isotropic electron–nuclear hyperfine interaction, the hole–nuclear coupling is strongly anisotropic. In the absence of HH–light hole (LH)

mixing, the hole–nuclear hyperfine interaction is Ising-like with coupling only between spin components along the growth direction [80,81]. Finite hole-mixing effects can lead to the coupling between the hole and nuclear spin components perpendicular to the growth direction. In the absence of magnetic field, pump-probe and time-resolved photoluminescence experiments on *p*-doped self-assembled dot have revealed hole–spin ensemble dephasing time of 14 ns [80]. Most significantly, in a magnetic field perpendicular to the growth direction, coherent population trapping has been observed for a single *p*-doped dot which suggests a transverse dephasing time longer than 100 ns [254]. These experimental findings are consistent with the theoretical studies of the hole–nuclear hyperfine coupling [80,81]. Since the *p*-doped QDs have similar energy level-schemes and transition selection rules to the *n*-doped ones, hole spins in QDs may be manipulated using optical schemes similar to those for electron spins. For example, high fidelity hole spin initialization has already been demonstrated [255], using similar optical pumping schemes previously adopted for electron spin initialization [256,257].

Another kind of solid-state electron spin systems which are under exciting development is NV centres in diamond. An NV centre in diamond is a defect with a C–C bond substituted with a negatively charged N atom, which has a spin-1 at the ground state. NV centre spins are a promising candidate for quantum computing for the following virtues [258]: First, as deep-level defects, they have chemical and thermal stability; second, the spin-orbit coupling in the light C and N atoms is very weak, so the spin decoherence by phonon scattering is negligible even at room temperature [89,94]; third, the natural abundance of isotopes with non-zero spin (C-13) is only about 1% and also the hyperfine interaction between the centre spins and the bath nuclear spins is mostly dipolar which is highly anisotropic and decays rapidly with the distance. Thus the electron spin decoherence by the hyperfine coupling is very slow (coherence time $>50\,\mu s$ in natural samples [89] and $\gtrsim$ milliseconds in C-13 depleted diamond [259]); fourth, the material is optically transparent and the centres are optically active, feasible for optical access [88,92,93,95,204] and coupling with cavities or waveguides [260–263]. The proposal of quantum computing with diamond defects [87] exploded to a hot research field after the experimental demonstration of electron spin Rabi oscillation [90] and two-qubit gates for coupled electron and nuclear spins [91] in single NV centres. Awchalom group [93] demonstrated coherent coupling between a 'bright' NV centre and a 'dark' nitrogen centre. Gaebel *et al.* [94] realized strong coupling between an NV spin and a nitrogen spin at room temperature. Lukin and colleagues [97] showed spin echo of an NV spin and observed coherent coupling between the electron spin and nuclear spins nearby. In 2007, Lukin group [98] managed to isolate and control an NV spin and a strongly coupled nuclear spin. In 2008, Neumann *et al.* [264] claimed multipartite entanglement among C-13 nuclear spin near an NV centre. Most recently, Lukin group [265] and Wrachtrup group [266] independently demonstrated readout of an NV qubit improved by repetitive retrieval of proximal nuclear spin ancillae [265,266].

In the remaining part of this review, we will discuss the optical manipulation schemes for QD electron spin qubits, and we expect that most of them shall be applicable for hole spins and NV centres as well, except the distinctive hyperfine

effects on the optical processes of the hole spins and of the NV centre with its proximity nuclear spin.

3. Physical structure

3.1. *Local nodes*

A local node is composed of a few QDs. The specific QD systems of interest include $In_{1-x}Ga_xAs$ self-assembled QDs and GaAs fluctuation QDs. These III–V compound semiconductors have direct bandgaps and thus are suitable for optical control. A fluctuation QD is formed by width fluctuation in a narrow quantum well grown with certain procedure (such as interruption for introducing interface roughness). This kind of dots has lateral confinement size ($\gtrsim$10 nm) much larger than the growth direction size ($\lesssim$5 nm) and the lateral confinement potential is shallow (usually in the order of a few millielectron volts). Thus a fluctuation QD would not host many bound electronic states and often just one, which is still subject to ionization due to thermal or optical excitation. Nonetheless, the loose lateral confinement makes optical transitions in a fluctuation QD well characterized by selection rules resulting from conservation of angular momentum with respect to the growth direction. The large size of fluctuation QDs also makes the dipole moment for inter-band transitions to be large and therefore enhances the optical coupling which is useful for strong coupling in cavity quantum electrodynamics (QED) and has been utilized in demonstrating optical control of excitonic qubits [231,232]. A self-assembled QD is formed by the spontaneous nucleation of one material (such as InAs) on the surface of a substrate (such as GaAs) which has a slightly different lattice constant. Such a QD is relatively small (with lateral size $\sim$10 nm) and deep confinement potential (in the order of hundreds of millielectron volts) which is defined by the offset between the band edge of the QD material and that of the substrate. As a result, a self-assembled QD could host quite a few stable bound states, providing extra flexibility for quantum control. There is no obvious reason to exclude other types of QDs, such as those formed in II–VI materials and II–VI nanocrystals [267], although they are less comprehensively studied in experiments mostly because of technical difficulties, such as the requirement of UV lasers, strong charge fluctuation around QD surfaces due to low material mobility and complex defects and impurity centres. The optical control schemes discussed in this review can be applied to the NV centres in diamond with some modifications.

In classical electronic computers, the physical layout of logic circuits is planarly extended. It is not hard to expect the planar layout to be used in a quantum computer. In self-assembling growth processes, vertically stacked QDs may be formed to several layers [268]. The vertical structure, however, is not extendable and furthermore, limits the accessibility by optical pulses. Planar distribution is naturally formed both in self-assembled QDs and in fluctuation QDs. Formation of QD molecules or arrays due to lateral coupling is possible [195,269]. With proper growth art, clusters of QDs with certain patterns may be fabricated [270–272]. Remarkably, NV centres in diamond may be implanted by ion beams with position precision in the order of 10 nm [158,159]. Having such technology within the scope of our consideration, we assume a local node in a quantum computer composed of a few

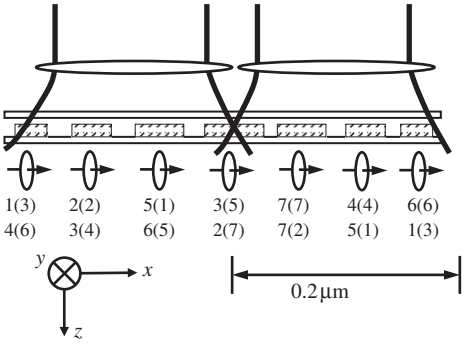

Figure 16. The physical structure of a local node consisting of seven electron spins in a QD cluster. Each QD is identified by a near-field microlens as well as by its characteristic transition energies. The numbers are used to label the qubits for factorizing 15 with the seed number $a = 4$ (top row) and $a = 13$ (bottom row), respectively. The numbers in the parentheses label the qubits at the end of computation (see Section 8.1 for details).

(usually fewer than 10) QDs (or impurities), laterally distributed and coupled. The control of electron spins in QDs is to be designed after a local node consisting a cluster of QDs has been fabricated and characterized. In this sense, the specific layout of a local node, which could be a ring, a line or any other graphs naturally formed, does not make essential difference. But a linearly displaced array would be preferable for its simplicity in coupling and practicality in manufacturing.

A scalable physical structure of a QD-based quantum computer should have the following features: (1) the QDs are placed in an extendable layout; (2) the QDs are connected so that electron spins can be coupled to a common photonic or electronic state and (3) the QDs are individually accessible so that the electron spins are individually controlled. On the one hand, the spatial resolution of near-field optical devices is still not high enough to identify each QD in a cluster. On the other hand, within the limit of current technologies, it is impossible to control the growth of QDs so that they are almost identical. Different sizes and shapes of the QDs would make the exciton transition energies in different QDs different. In this way, the near-field optics and the fingerprint transition frequencies of different QDs may be combined together to individually address each dot or to selectively couple a pair of them. The coupling between spins in general is mediated by virtual tunnelling between different QDs which may be activated by virtual optical excitation of excitons in the presence of extra electrons which bear the spins (more details will be discussed in later sections). For NV centres in diamond, such mechanisms are not yet considered, but other schemes may be applicable, such as coupling through virtual excitation of cavity modes [64], or hyperfine interaction with nuclear spin baths [100].

We show an example in Figure 16 a working module of seven qubits in a linearly displaced array of QDs. With the QDs of the size around 50 nm and about 20 nm apart, the seven dots may be addressed with two microlenses attached to, e.g., optical fibres, with resolution of about 0.2 μm. The QDs addressed by the same optical fibre are distinguished by their signature transition frequencies. Using optical pulses with different frequencies and polarizations, each dot and each adjacent dot pair may

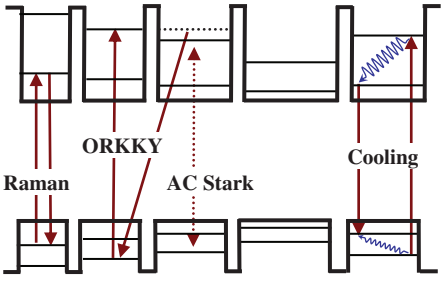

Figure 17. The energy diagram of various optical processes for quantum gates and initialization: 'Raman' for single-spin control or optical pumping and measurement of a single spin, 'ORKKY' for two-spin control, 'AC Stark' for transient shift of energy levels to realize selective resonance, and 'Cooling' for initialization of spins via phonon bath (phonon emission as wavy lines).

be (virtually) excited and various single- and two-qubit gates and initialization could be realized, as illustrated in Figure 17. To realize arbitrary single-spin rotation, a magnetic field is applied along the in-plane direction (denoted as the z-direction). We assume that only neighboring QDs are coupled, for simplicity. Coupling between spins in farther separated dots is to be accomplished by recursively using the nearest neighbor coupling, which increases the number of gates by an amount in the order of the number of dots between the two ends. To minimize the number of operations between separated qubits, the quantum algorithms are compiled by using optimum labelling of the qubits. Taking into account the size of the microphotonic structures (including cavities and waveguides connecting local nodes), a working module of about 10 QDs could occupy an area of about $10\,\mu m \times 10\,\mu m$, so a quantum chip of size $10\,cm \times 10\,cm$ can in theory accommodate 10^8 qubits.

For the purpose of addressing and optical control of a single QD, several near-field optics technologies have been available, such as micro-optical masking and microfibre optics [273]. For a cluster of QDs to function under optical control, however, there are still non-trivial technical challenges, including at least fabrication of QD clusters with energy levels and inter-dot couplings falling in the desired parameter ranges, assembling of microlenses on the surface of QD clusters, and designing, shaping and controlling complex laser pulses. The microlens technology has been widely used in the digital imaging industry (microlenses of similar sizes are routinely used to focus light into individual pixels in commercial digital cameras).

3.2. *Distributed structure*

The electron spin qubits are distinguished by the different optical transition frequencies of the host QDs. Thus, the dot density shall be rather dilute so that each laser spot contains only a small number of QDs ($\sim$O(10), considering the typical inhomogeneous broadening of the excitonic linewidth of $\sim$10–100 meV, and the requirement of $\sim$0.1–1 meV frequency separation for optically addressing individual QDs. Therefore, the optical approach predetermines that a local node can only have

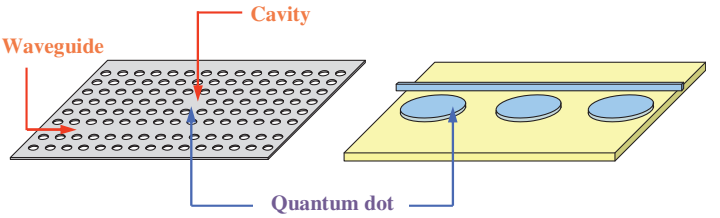

Figure 18. Left: Coupled cavity and waveguide structure formed by point and line defects in 2D photonic bandgap crystals; Right: waveguide coupled microdisc cavity etched on chip. Layers of QDs can be embedded in the matrix slab where the cavities are formed.

a limited number of qubits. In order to scale up, a distributed architecture could be a solution [2,274]. In such structures, clusters of QD electron spin qubits form quantum nodes where logical operations can be performed locally, and connections between clusters are through quantum channels in which the flying qubits take information from one place to another.

The single photon wavepacket is an ideal candidate as the carrier of flying qubits, being widely used in quantum cryptography [275] and linear optics quantum computation [276]. The qubit can be encoded in the photon-number subspace [277] or polarization subspace [276]. While single photon propagation in free space is un-channeled and inefficient, optical waveguides in semiconductors and optical fibres provide directional channels.

In the distributed architecture of optically controlled spin quantum computation, flying photons in waveguides/fibres are responsible for integrating the distributed stationary spin clusters into a globally functioning quantum computer. This requires quantum interfacing between single electron spins in QDs and single photons in waveguide. As mentioned in Section 2, QD electron spins interact with optical fields via the intermediate states of trions. Such interface at the single photon level requires strong light-matter interactions. As a QD has a fixed optical transition dipole moment which is limited by its size, one way to have such strong light-matter interaction is to confine photons in optical cavity structures with small volumes.

Microcavities can be realized in a number of ways in semiconductor structures. We list below the essential properties of a few representative ones:

(1) *Microdisk* – See Figures 18 and 19 for schematic illustrations of the geometry. Light is confined by total internal reflection in the inner wall and the confined modes are known as the whispering gallery modes. Quality factor $Q \sim \mathrm{O}(10^4)$ in III–V materials and $\sim\mathrm{O}(10^5)$ in polymer; mode volume $V \sim 6(\lambda_0/n)^3$ where n is the refractive index of the material and λ_0 the wavelength of cavity mode [278]. Strong coupling regime for GaAs fluctuation QD embedded in microdisc structure similar to the illustration in Figure 19 has been achieved [279]. Because of the large dipole moment of the fluctuation dot, the measured cavity-dot coupling constant $g_{\mathrm{cav}} \sim 0.2\,\mathrm{meV}$ signifies strong coupling.

(2) *Defect cavity in 2D Photonic Crystal* – Two-dimensional photonic bandgap crystals are an ideal structure to form a cavity resonator [280,281].

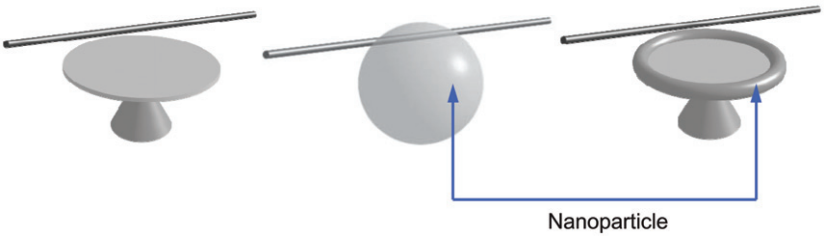

Figure 19. Left: fibre coupled microdisc cavity; Middle: fibre coupled microsphere cavity; Right: fibre coupled microtoroid cavity. Semiconductor nanoparticles, e.g. diamond with NV centres, can be adsorbed onto the latter two types of cavities.

Propagation of light in the plane has a forbidden bandgap for carefully designed periodical arrays of air holes drilled on the 2D slab. As shown in Figure 18, by forming a point defect in the 2D array of air holes, light can be almost perfectly confined in the plane of the slab if its frequency lies in the forbidden bandgap. The vertical confinement, achieved by total internal reflection at the semiconductor–air interfaces, is imperfect, in that light with small in-plane wavevectors can leak out of the top and bottom. Vertical leakage can be greatly suppressed by proper engineering of the defect [282,283]. $Q \sim 6 \times 10^5$ and $V \sim 1.2(\lambda_0/n)^3 \sim 0.072\,\mu m^3$ have been achieved [282,283]. Theoretically analysis shows that Q-factors greater than 2×10^7 are realizable by optimizing the structure [283]. The matrix of a 2D photonic crystal can be either silicon or III–V compounds [284]. Strong coupling with single self-assembled InAs QDs has been demonstrated [284,285], where $g_{cav} \sim 0.1$ meV.

(3) *Micropillar* – Light is vertically confined by distributed Bragg reflector mirrors and horizontally by total internal reflection. $Q \sim 10^4$ and $V \sim \mu m^3$ have been achieved [286,287]. Strong coupling with single self-assembled InAs QDs has been demonstrated [286,288], where $g_{cav} \sim 0.1$ meV.

(4) *Epitaxial cavity* – Vertical confinement is by distributed Bragg reflector mirrors and horizontal confinement by thickness variations, similar to the confinement principle of the fluctuation QD [289]. $Q = 3 \times 10^4$ and $V \sim \mu m^3$ have been achieved [289].

(5) *Silicon microsphere* – WGMs are confined by total internal reflection. Q exceeding 10^8 and $V \sim 10^3\,\mu m^3$ have been achieved [290,291]. Nanocrystals (such as CdSe nanocrystals [292] and diamond nano-crystals with NV centres [260]) deposited on the surface are usually used for coupling with the cavity photons.

(6) *Microtoroid* – See Figure 19 for an illustration of the geometry. WGMs are confined by total internal reflection. $Q \sim 10^8$ is achieved with principal diameter $D \sim 100\,\mu m$ and the minor diameter $d \sim \mu m$ [293]. Theoretical analysis shows the possibility of realizing microtoroid with Q exceeding 10^8 and $V \sim O(10)\,\mu m^3$ [294].

The high quality factor allows photons to be confined for a sufficiently long time inside a cavity and the small mode volume makes possible a large intra-cavity

electromagnetic field from a single photon. Both features are critical for the strong dot–cavity coupling, defined by the criteria that a single cavity photon can induce $\gtrsim 2\pi$ Rabi oscillation of an excitonic transition in a single dot within the lifetimes of the cavity photon and the exciton. Strong coupling has already been realized in several cavity–dot systems [260,279,284–286,288,292]. With microcavity being a playground for strong coupling of a single photon with a single dot, the interface between a flying photon qubit in a waveguide and a stationary spin qubit in a QD can be achieved by evanescent coupling between an optical waveguide/fibre and a microcavity containing the QD (see Figure 18 and 19). A single photon wavepacket propagating in the waveguide can excite a cavity photon which then significantly influences the QD spin dynamics, e.g. through the optical Raman process via the trion states (see Section 2.2) [119]. In addition to the exciting advances in improving the Q-factor and reducing the mode volume of semiconductor microcavities for strong coupling, many other key ingredients towards the construction and control of such a dot–cavity–waveguide coupled structure have been progressively achieved in laboratories. These include the high-efficiency coupling between microcavities and optical waveguides/fibres [295–301], precise control of intra-cavity location of QDs [285,302,303], fine-tuning of cavity modes into resonance with a given QD transition [285,302,304–306], electrically controllable charging of intra-cavity QDs [307] and coherent resonant driving of QD excitonic transitions inside a cavity by an external laser [230,308].

With the possibility of spin-photon interfacing in dot–cavity–waveguide structures, we are able to outline the construction of a distributed architecture for scalable quantum information processing in an integrated semiconductor platform composed of QDs, optical microcavities and optical waveguides/fibres (Figure 20) [309]. In this

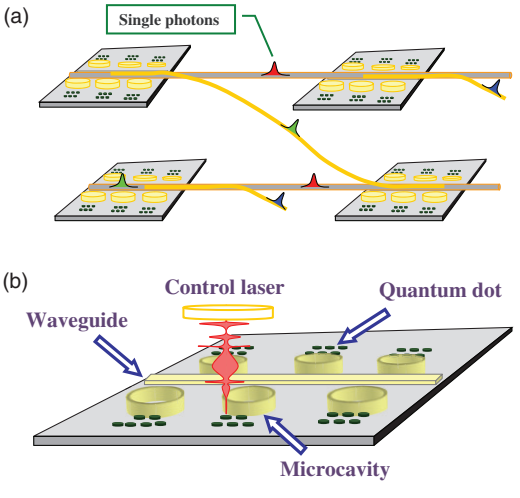

Figure 20. Distributed quantum information processing in integrated semiconductor structures. (a) Schematics of a distributed quantum computer where communications between computation modules are mediated by single photons in optical waveguides/fibres. (b) The spin-based computation modules on a chip, controlled by ultrafast optics.

network structure, a local node contains a limited number of charged QDs, distinguishable by their optical frequencies. The stationary spin qubits form a basis for the quantum memory and quantum logic modules. Optical waveguides/fibres connect distributed nodes with single photon wavepackets as the flying qubits. Microcavities offer the playground for the strong interaction between the two types of qubits. Control of a local node will be the focus of Section 4. Control of the interfacing between single spins and single photons will be the focus of Section 7. With the recent progresses in coupling NV centres in diamond with photons in cavities and waveguides [260–263], similar distributed quantum computing with NV centres is also foreseeable.

4. One- and two-qubit operations

It has been established that universal quantum computation can be accomplished by a set of single-qubit gates and one kind of entanglement gates, such as CNOT, $\sqrt{\text{SWAP}}$ or controlled phase-shift gate [172,183,184]. While there are many alternatives, we follow a more traditional and scalable approach of designing a system which has negligible interaction between qubits when the system is idling, and creating transient interaction between two qubits during the operation.

General speaking, there are two strategies for controlling electron spins in QDs, namely, the direct and the indirect controls. As the terminology suggests, the direct control manipulates the electron spins directly which may be realized by rotation of a single spin with an AC magnetic field from, e.g., a microwave or a pulse DC magnetic field [66,88,90,97,98,161], and by coupling two spins via exchange interaction mediated by virtual tunnelling between QDs switched by, e.g., gate voltages [63,65,82]. The direct control schemes are more applicable to electrically defined QD systems made possible by the feasibility of *in situ* electrical gates. There is no fundamental obstacle to integrate electrical gates to self-assembled or fluctuation QD systems and to apply the direct control of electron spins. But the much smaller size of these QDs as compared with the splitting-gate defined ones and the much stronger confinement (or much less tunnelling probability) cause non-trivial technical problems. The indirect control schemes are based on indirect coupling between electron spin states mediated by virtual excitation of auxiliary energy levels which are modified by (or conditioned on) the states of the spins [64,68–79,181,182]. Usually, such intermediate states are excitons which may be excited by optical pulses. The optical control of electron spins is limited to direct-gap semiconductors but otherwise have a great deal of merits particularly due to the energy scale cascade. As bandgaps in semiconductors are usually larger by orders of magnitude than the electron spin Zeeman energy, the control of the electron spins could be made much faster by using excitation cross the large bandgap. For comparison, electrical control of spins on the nanosecond scale is already the state-of-the-art technique [108,161], while optical manipulation of electron spins can be completed on the picosecond timescale [78,79,181,182].

In essence, all schemes of optical control of the electron spin states [64,68–76,173] are realized by the Raman processes where the virtual excitation of excitons plays the central role. In one-qubit operations, the intermediate states are excitons with one

excess electron, i.e., the trion states [68,72,76]. In two-qubit operations [64,68–71,73–76,173], the intermediate states are excitons with two excess electrons. The effective exchange interaction between two spins may be induced by the virtual excitation of one exciton tunnelling back and forth between two dots, which is similar to the RKKY process and is dubbed optical RKKY interaction to indicate the role of the optical excitation [73–75]. Alternatively, even if there is no tunnelling between QDs, the interplay between Coulomb interaction and the spin blocking effect would induce effective interaction between two separated spins when two excitons are (virtually) excited in two dots [68–71,173]. The spin interaction may also be mediated by virtual photon exchange during the virtual excitation of excitons [64,76].

More details about the optical control of one-spin and two-spin gates follow. Since the essential physics of various optical control schemes is similar, we will focus on two specific examples, namely, Raman control of single spins, and optical RKKY control of two spins, as an illustration of the physics and the operation conditions.

4.1. *Single-spin rotation by Raman process*

Arbitrary single-spin rotation can be realized via adiabatic Raman processes mediated by trion states [72,169]. We will illustrate the basic idea of such a scheme and discuss the non-adiabatic generalization and certain limits of the method. It is worth pointing out that the stimulated Raman adiabatic passage (STIRAP) [310] involving only dark states could not realize an arbitrary rotation but only a spin flip from a known initial state. The adiabatic Raman processes in arbitrary spin rotation involves both dark states and bright states [72].

The control of an electron spin relies critically on the spin states of the excited excitons which are determined by the optical selection rules in the semiconductor QDs. In the III–V semiconductors of zinc-blende crystal structure, the selection rules of optical excitations at the band edge are well-defined by the angular momentum conservation in terms of the electron spin in the conduction band and the hole spin in the valence band, which have angular momentum $s = 1/2$ and $J = 3/2$, respectively. In QDs of large lateral sizes and strong confinement in the growth direction (defined as the z-axis), the hole states will be split into two sets of degenerate states, with spin states $J_z = \pm 3/2$ and $\pm 1/2$, respectively, designated as HH and LH, respectively, according to their effective mass along the z-axis. When the lateral sizes of the QD are much larger than the confinement size in the growth direction, the mixing of different angular momentum states by the lateral confinement is small [81]. Thus the optical excitation is restricted by the angular momentum conservation along the z-axis. Now if the controlling optical pulses are applied normal to the sample surface, the conservation of the angular momentum about the growth direction makes it impossible to flip the electron spin along the z-axis and thus impossible to complete an arbitrary quantum operation, unless the light beam is incident with an angle [311] or the symmetry is broken by a magnetic field with a non-zero in-plane component. Since in the near-field optics, the incident light is usually normal to the surface, we need a static in-plane magnetic field applied (whose direction is defined as the x-axis). Under the strong magnetic field, the electron spin states are split into

two Zeeman levels $|+x\rangle$ and $|-x\rangle$ with energy $\pm\omega_c/2$, respectively. We use these two states as the basis $|0\rangle$ and $|1\rangle$ of a qubit. The Zeeman splitting ω_c is in the order of 0.1–1 meV under a magnetic field of a few Tesla. In GaAs fluctuation QDs, the hole states are still near-degenerate, since the large HH–LH splitting ($\Delta_{\rm hl}$ is tens of millielectron volts) makes the hole spin splitting $\sim \omega_c^3/\Delta_{\rm hl}^2$ negligible even under a field as strong as a few Tesla, so the hole states can still be defined by the magnetic quantum number J_z as $|\pm 3/2\rangle$, which will also be denoted by hollow arrows as $|\Downarrow\rangle$ and $|\Uparrow\rangle$, respectively. In this case, the optical transitions can be separated by the selection rules even when the energy difference due to the electron spin splitting is relatively small. Note that the near-degeneracy of the two trion states is not a necessary condition in the schemes of single spin rotation to be discussed below. Actually, in self-assembled dots where hole states can be split by an in-plane magnetic field due to the large HH–LH mixing, the splitting between the trion states can be exploited to separate desired transitions from unwanted ones by energy difference.

To illustrate the essential physics underlying the control process, we ignore the high-lying excited states and model the system by four states consisting of the two split electron spin states and two trion states $|t_\pm\rangle$ which are formed by two electrons in the singlet state $|\uparrow\downarrow\rangle$ and one hole in the spin state $|\Uparrow\rangle$ or $|\Downarrow\rangle$, respectively. According to the angular momentum conservation about the z-axis, the selection rules of the optical excitation, as depicted in Figure 21(a), is such that a light with circular polarization $\sigma^\pm$ will induce the transition from the electron states $|+1/2\rangle$ or $|-1/2\rangle$ to the trion states $|t_\pm\rangle$, respectively.

So, under the excitation of an optical pulse with σ^+ polarization, the dynamics is reduced to a Raman rotation in the Λ-type three-level system (as shown in Figure 21(b)), which is governed by the Hamiltonian

$$H = \omega_c s_x - \Omega^*(t)|+1/2\rangle\langle t_+| - \Omega(t)|t_+\rangle\langle +1/2| - \Delta|t_+\rangle\langle t_+|, \tag{8}$$

where $s_{x/y/z}$ is the electron spin operator along the x-, y- or z-direction, respectively, $\Omega(t)$ is Rabi frequency of the laser pulse in the rotating frame, and Δ is the detuning of the laser relative to the trion state $|t_+\rangle$. To eliminate the dynamic

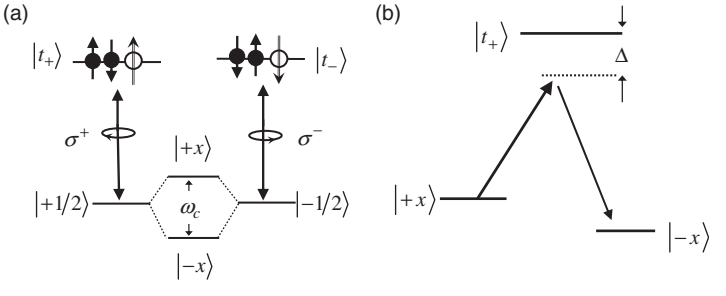

Figure 21. (a) Optical selection rules for the electron-trion transitions. (b) The Raman process in the Λ-type three-level system formed by the electron spin states and the trion states connected by a σ^+-polarized laser pulse.

phase associated with Zeeman splitting, the quantum operation should be done in the frame rotating together with the free spins under the magnetic field. By the transformation $S \equiv \exp(i\omega_c t s_x)$, the Hamiltonian in the precessing frame is written in the matrix form

$$\tilde{H} = \begin{bmatrix} 0 & 0 & -\Omega^*(t)e^{+i\omega_c t/2}/\sqrt{2} \\ 0 & 0 & -\Omega^*(t)e^{-i\omega_c t/2}/\sqrt{2} \\ -\Omega(t)e^{-i\omega_c t/2}/\sqrt{2} & -\Omega(t)e^{+i\omega_c t/2}/\sqrt{2} & -\Delta \end{bmatrix}, \tag{9}$$

in the basis of $e^{+i\omega_c t/2}|-x\rangle$, $e^{-i\omega_c t}|+x\rangle$, and $|t_+\rangle$.

For large detuning ($|\Delta|$ much greater than the bandwidth of the optical pulse and the Rabi frequency), the so-called adiabatic approximation is justified and thus under a standard canonical transformation, the off-diagonal terms in the Hamiltonian between the electron spin states and the trion state are eliminated up to the second order of the Rabi frequency. So the transformed effective Hamiltonian is approximated as

$$\tilde{H}_{\text{eff}} \approx \begin{bmatrix} |\Omega(t)|^2/(2\Delta) & -|\Omega(t)|^2 e^{+i\omega_c t}/(2\Delta) & 0 \\ -|\Omega(t)|^2 e^{-i\omega_c t}/(2\Delta) & |\Omega(t)|^2/(2\Delta) & 0 \\ 0 & 0 & -\Delta - |\Omega(t)|^2/\Delta \end{bmatrix}. \tag{10}$$

This is equivalent to a magnetic field with strength $|\Omega(t)|^2/(2g\mu_B\Delta)$ precessing in the x–y plane with the angular frequency ω_c (the time-dependent optical Stark shift [311] of the electron energy $|\Omega(t)|^2/(2\Delta)$ contributes only a trivial global phase-shift and can be ignored). In cases that the optical pulse is much shorter than the spin precession period, the effective magnetic field becomes an instantaneous pulse which can be controlled in the femtosecond timescales (cf. the GHz limit on the control of external magnetic field). For $t \approx n\pi/(\omega_c)$ (n is an integer), the magnetic field pulse is effectively along the z-axis, and for time around $(n+1/2)\pi/\omega_c$, the instantaneous rotation of the spin is effectively along the y-axis. Thus we have two SU(2) generators which can be combined to complete an arbitrary rotation of the electron spin. To be specific, a spin rotation with angle γ along an axis defined by the Euler angles (α, β), denoted as $R(\alpha, \beta, \gamma)$, can be realized by at most three elementary rotations along different axes in the x–y plane, for

$$R(\alpha,\beta,\gamma) = R\Big(\frac{\pi}{2}, \frac{\pi}{2}+\beta, \frac{\pi}{2}-\alpha\Big) R\Big(\frac{\pi}{2}, \beta, \gamma\Big) R\Big(\frac{\pi}{2}, -\frac{\pi}{2}+\beta, \frac{\pi}{2}-\alpha\Big), \tag{11}$$

where the three elementary rotations on the right-hand side of the equation can be performed in turn at $t = -\pi/(2\omega_c) + \beta/\omega_c$, β/ω_c, and $+\pi/\omega_c + \beta/\omega_c$, which can be completed within half the precession period of the electron spin. For an electron with Zeeman splitting of 1 meV, the duration of an arbitrary operation of a single spin is less than 2 ps.

To complete a finite rotation of the spin at a time much shorter than the precession period, the Rabi frequency should be large, which, however, could demolish the condition for the adiabatic approximation. For instance, if the Zeeman

splitting is 0.1 meV and the detuning is 1 meV, to complete a π rotation within a duration one tenth of the precession period, the Rabi frequency is required to be about 3 meV, greater than the detuning, which makes the adiabatic approximation unjustified. In fact, to validate the adiabatic condition for instantaneous operations, it is required that $\omega_c \ll \Delta$, which means slow operations for reasonably large detuning ($\Delta < 10$ meV). Alternatively, by shaping the control laser pulse, the rotation can also be operated in the non-adiabatic regime or in a non-instantaneous manner. No matter how intense and how fast the optical pulse could be, the spin rotation in general cases, however, is still limited by the precession period, as can be seen from the equation for the spin polarization as

$$\partial_t \langle s_z \rangle = \omega_c \langle s_y \rangle - \partial_t \rho_t, \tag{12}$$

where ρ_t is the population of the trion state. For a complete operation, the residue population of the trion should be zero, so the change of the spin momentum along the z-direction is $|\delta\langle s_z\rangle| = \left|\omega_c \int_0^t \langle s_y\rangle \mathrm{d}t\right| \leq \omega_c t$, which cannot be faster than the precession under the static external magnetic field.

In summary, under a moderate external magnetic field ($\lesssim$10 T and $\omega_c \sim 1$ meV), an arbitrary spin rotation can be accomplished well within 10 ps by up to three ultrashort optical pulses (with simple shape and large detuning) or by one pulse (with engineered shape). Remarkably, control of single electron spins [79,236,312] and hole spins [78] in QDs in picosecond timescales have been recently realized in experiments. Using the optical control, Yamamoto's group has demonstrated spin echo for an ensemble of impurities in GaAs [181] and for a single QD spin [313]. Greilich *et al*. [182]. have realized optical rotation of an ensemble of QD spins along arbitrary axes.

4.2. *Two-qubit gates by optical RKKY interaction*

To implement two-qubit quantum gates, optically induced RKKY (ORKKY) interaction between electrons doped in QDs has been proposed to couple two spins, laterally via continuum excitons [73,74] or vertically via discrete states [75]. The ORKKY interaction mediated by continuum excitons [73,74], due to the extension nature of the continuum states, is less controllable in selectively coupling certain spins. The ORKKY interaction between QDs vertically stacked [75], on the other hand, is not applicable to a scalable system with a planar layout. For the sake of scalability, we consider to employ the discrete excited states in laterally coupled QDs to induce the ORKKY interaction, which, as described below, can be controlled to selectively couple spins in designated adjacent QDs. The ORKKY interaction is by nature a Raman process with the ground states formed by the two-electron spin states and the intermediate states by excitons charged with two excess electrons.

The physical process of the ORKKY interaction via discrete intermediate states is depicted by the Feynmann diagram in Figure 22(a). The qubits under controls are the spins of two electrons in the ground states of two neighboring QDs, denoted as $\mathbf{s}_1$ and $\mathbf{s}_2$. When the electrons are in the ground states, the inter-dot tunnelling is negligible and therefore the two spins have no direct exchange interaction. The basic

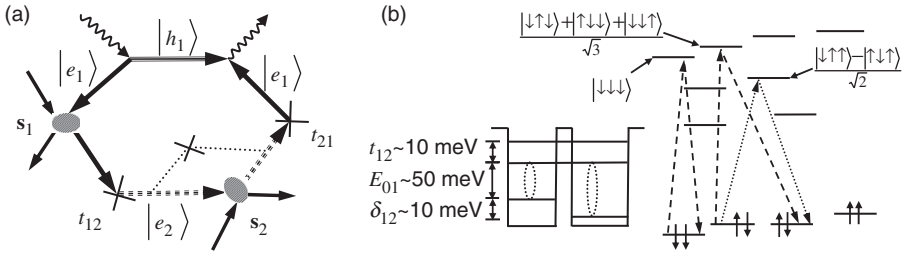

Figure 22. (a) Feynman diagram for optical RKKY interaction. The straight arrows are electron or holes lines, the wavy arrows are photon lines, the tunnelling is the cross vertices, the Coulomb exchange is the scattering vertices, and the AC Stark field is the dotted lines with cross. (b) Energy level schematics for two-qubit gates. The two-spin states are split by the magnetic field, and the exciton charged with two electrons (the hole is understood) is split both by the Coulomb exchange energy and by the magnetic field. The dotted arrows are optical excitation for a SWAP gate, which together with the excitation represented by dashed arrows can also accomplish the phase gate.

elements of the ORKKY process for mediated interaction between the two qubits can be described as:

(1) an incident optical pulse excites a direct electron-hole pair into the excited electron and hole levels in, say, QD 1, denoted as $|e_1\rangle \otimes |h_1\rangle$;
(2) the optically excited electron will interact with the electron spin $\mathbf{s}_1$ with the strong exchange interaction ($\lambda_i \sim 5$ meV in a typical InAs QD), while the electron-hole exchange interaction is negligible in comparison;
(3) with a strong quasi-cw optical field applied, the excited electron levels in the two QDs can be tuned into resonance by the optical Stark effect, and thus the electron in the excited state $|e_1\rangle$ can resonantly tunnel into the second QD with the tunnelling rate in the order of 10 meV for two QDs separated by 15 nm, while the hole tunnelling can be neglected due to the stronger confinement and off-resonance condition;
(4) having tunnelled into the excited level of the second QD, the optically excited electron can exchange spins with the excess electron in the second QD via the strong exchange interaction;
(5) after the exchange interaction with the second qubit electron, the electron in the excited state can tunnel back into the first QD and
(6) the electron back to the first QD can be recombined with the hole by emitting a photon back into the optical pulse, leaving the two excess electrons an effect of indirect spin exchange. Since the laser frequencies can be adjusted to selectively excite the exciton in one QD and to selectively shift the level in another QD by the AC Stark effect, a pair of adjacent QDs can be coupled on demand.

Since the Coulomb and the exchange interactions could be strong for electrons in the discrete states, as compared with the optical Rabi frequency, it is better to

treat the interactions non-perturbatively by first exactly diagonalizing the states of charged excitons, and use the eigenstates as the basis for calculating the optically induced indirect exchange interaction. In fact, when the intermediate states are discrete eigenstates of the Coulomb interaction, the ORKKY process becomes equivalent to the Raman process in the multi-level systems with the two-spin states as the ground states and the charged exciton states as the intermediate states. Then the optical excitation can be treated as a perturbation, similar to the case of the single-spin rotation, and the adiabatic approximation may also be adopted when the detuning is large.

As shown in Figure 22(b), we assume the following characteristic energies for two neighboring QDs of different sizes, which can be realized by properly adjusting the QD sizes, the separation and the composite x in $In_{1-x}Ga_xAs$ in typical cases under consideration: the difference in transition energy between the neighboring dots is $\delta_{12} \sim 10\,\text{meV}$, the distance between the ground and excited electron states $E_{01} \sim 50\,\text{meV}$, the tunnelling strength between neighboring excited states $t_{12} \sim 10\,\text{meV}$, and the Coulomb exchange energy between electrons $\lambda_{1/2} \sim 5\,\text{meV}$. When the electron-hole pair is excited into the excited single-particle levels in the smaller QD, the difference between the binding energy of the direct exciton (when both the electron and the hole are in the smaller dot) and that of the indirect exciton (when the electron has tunnelled into the large dot), which is $\sim$10 meV, can already compensate most of the energy difference (δ_{12}) between the excited single-particle levels in the two dots. And if desired, a further optical pumping can be used to fine-tune the energy levels in the dots so that near-resonance tunnelling can occur between the excited levels for electrons in the two dots. The ground single-particle states for electrons and the hole states can be virtually taken as localized due to the relatively high barrier.

To illustrate the basic idea of using the discrete exciton states in laterally coupled QDs for ORKKY interaction between the two qubit spins, we assume that the hole is (virtually) created by the optical pulse only at the first excited level in the smaller QD and the dynamics is essentially determined by the interaction between the two qubit spins and the optically excited electron. The role of the hole is then just to impose the renormalization of the electron energies. As mentioned above, both the tunnelling and Coulomb exchange are in the strong coupling regime, they should be considered non-perturbatively. So we can first diagonalize the Hamiltonian with the exchange energy and electron tunnelling fully included. As the tunnelling is spin-independent, we consider only the bond state of the QD molecule and treat the anti-bond state as in far off-resonance (since it is about 10 meV above). Thus the relevant spins are qubit 1 ($\mathbf{s}_1$), qubit 2 ($\mathbf{s}_2$) and the spin of the bond molecular state 3 ($\mathbf{s}_3$). The Hamiltonian of these three spins is

$$H = 2\lambda_1 \mathbf{s}_1 \cdot \mathbf{s}_3 + 2\lambda_2 \mathbf{s}_2 \cdot \mathbf{s}_3 + 2\omega_c(s_1^z + s_2^z + s_3^z), \tag{13}$$

where λ_1 and λ_2 are the exchange energy in each dot. For simplicity, we assume $\lambda_1 = \lambda_2 = \lambda$. The eigenstates and the corresponding eigen energies can be

worked out as

$$
\begin{aligned}
&\left|S,\tfrac{1}{2},-\tfrac{1}{2}\right\rangle=\tfrac{1}{\sqrt{2}}\left(|\downarrow\uparrow\downarrow\rangle-|\uparrow\downarrow\downarrow\rangle\right), && \varepsilon=-\omega_c,\\
&\left|S,\tfrac{1}{2},+\tfrac{1}{2}\right\rangle=\tfrac{1}{\sqrt{2}}\left(|\uparrow\downarrow\uparrow\rangle-|\downarrow\uparrow\uparrow\rangle\right), && \varepsilon=+\omega_c,\\
&\left|P,\tfrac{3}{2},-\tfrac{3}{2}\right\rangle=|\downarrow\downarrow\downarrow\rangle, && \varepsilon=\lambda-3\omega_c,\\
&\left|P,\tfrac{3}{2},-\tfrac{1}{2}\right\rangle=\tfrac{1}{\sqrt{3}}\left(|\uparrow\downarrow\downarrow\rangle+|\downarrow\uparrow\downarrow\rangle+|\downarrow\downarrow\uparrow\rangle\right), && \varepsilon=\lambda-\omega_c,\\
&\left|P,\tfrac{3}{2},+\tfrac{1}{2}\right\rangle=\tfrac{1}{\sqrt{3}}\left(|\downarrow\uparrow\uparrow\rangle+|\uparrow\downarrow\uparrow\rangle+|\uparrow\uparrow\downarrow\rangle\right), && \varepsilon=\lambda+\omega_c,\\
&\left|P,\tfrac{3}{2},+\tfrac{3}{2}\right\rangle=|\uparrow\uparrow\uparrow\rangle, && \varepsilon=\lambda+3\omega_c,\\
&\left|P,\tfrac{1}{2},-\tfrac{1}{2}\right\rangle=\tfrac{1}{\sqrt{6}}\left(|\uparrow\downarrow\downarrow\rangle+|\downarrow\uparrow\downarrow\rangle-2|\downarrow\downarrow\uparrow\rangle\right), && \varepsilon=-2\lambda-\omega_c,\\
&\left|P,\tfrac{1}{2},+\tfrac{1}{2}\right\rangle=\tfrac{1}{\sqrt{6}}\left(|\downarrow\uparrow\uparrow\rangle+|\uparrow\downarrow\uparrow\rangle-2|\uparrow\uparrow\downarrow\rangle\right), && \varepsilon=-2\lambda+\omega_c,
\end{aligned}
\tag{14}
$$

as schematically shown in Figure 22(b), where the up/down arrows indicate in turn the spin states of qubit 1, qubit 2 and the electron created by optical excitation, quantized along the external magnetic field direction. Notice $\lambda\sim 5\,\text{meV}\gg 2\omega_c\sim 1\,\text{meV}$. The two-qubit gates can just be realized by the Raman passages between the two-spin ground states mediated by the charged excitons formed by one hole plus three electrons in the spin states shown above. To be specific, we discuss two frequently used two-qubit gates as below.

4.2.1. *SWAP and $\sqrt{SWAP}$ gates*

A SWAP gate interchanges the states of two qubits. Its matrix form is shown in Figure D1. In the Raman process, it just flips the two states: $|\uparrow\downarrow\rangle$ and $|\downarrow\uparrow\rangle$. The intermediate state connecting these two states by Raman process is $|S,\tfrac{1}{2},\tfrac{1}{2}\rangle\equiv\tfrac{1}{\sqrt{2}}\left(|\uparrow\downarrow\uparrow\rangle-|\downarrow\uparrow\uparrow\rangle\right)$ (henceforth the hole state in the exciton has been omitted for the sake of simplicity), which is optically coupled only to the two-spin singlet state $\tfrac{1}{\sqrt{2}}\left(|\uparrow\downarrow\rangle-|\downarrow\uparrow\rangle\right)$. By performing a $2n\pi$ Rabi rotation between the intermediated exciton state and the singlet ground state, a pure phase-shift will be induced to the singlet state, whose value is determined by the detuning. When such a phase-shift is controlled to be π (which can be obtained by, e.g., setting the rotation angle to be 2π and the detuning is zero), the two states $|\uparrow\downarrow\rangle$ and $|\downarrow\uparrow\rangle$ are just flipped and the SWAP gate is realized. In practice, the optical pulse can be tuned off-resonance from the transition to suppress the spontaneous decay. With proper polarization, the optical pulse does not excite the nearby state $|S,\tfrac{1}{2},-\tfrac{1}{2}\rangle$ and all other transitions are at separated by an energy of λ. So this operation can be accomplished in a period of time $\sim 10\times(2\pi\lambda^{-1})\sim 10\,\text{ps}$. Considering the optical Stark pulse used for tuning the resonant tunnelling, a two-qubit SWAP gate in such a scheme would require two optical pulses of duration of about 10 ps.

By choosing a proper detuning, the phase-shift can also be controlled to be $\pi/2$, and then the SWAP gate is performed halfway, or the $\sqrt{\text{SWAP}}$ gate is realized,

which has the matrix form

$$U_{\mathrm{SS}} = \begin{pmatrix} 1 & 0 & 0 & 0 \\ 0 & \frac{1+i}{2} & \frac{1-i}{2} & 0 \\ 0 & \frac{1-i}{2} & \frac{1+i}{2} & 0 \\ 0 & 0 & 0 & 1 \end{pmatrix}. \tag{15}$$

The $\sqrt{\mathrm{SWAP}}$ gate can generate entanglement between the two spins and can be used to realize the controlled phase gate and the CNOT gate.

4.2.2. *Controlled phase gate*

Another two-qubit gate which can be used in lieu of the CNOT gate for universal quantum computation is the controlled phase gate which induces a phase-shift of the target qubit depending on the state of the controlling qubit. The general matrix form of the controlled phase gate is

$$\begin{pmatrix} e^{i\phi_{\downarrow\downarrow}} & 0 & 0 & 0 \\ 0 & e^{i\phi_{\downarrow\uparrow}} & 0 & 0 \\ 0 & 0 & e^{i\phi_{\uparrow\downarrow}} & 0 \\ 0 & 0 & 0 & e^{i\phi_{\uparrow\uparrow}} \end{pmatrix} = e^{i\frac{\phi_{\downarrow\uparrow}+\phi_{\uparrow\downarrow}}{2}} \left[R_x(\phi_{\uparrow\downarrow} - \phi_{\downarrow\downarrow}) \otimes R_x(\phi_{\downarrow\uparrow} - \phi_{\downarrow\downarrow}) \right] \begin{pmatrix} 1 & 0 & 0 & 0 \\ 0 & 1 & 0 & 0 \\ 0 & 0 & 1 & 0 \\ 0 & 0 & 0 & e^{i\phi} \end{pmatrix}, \tag{16}$$

where the subscript of the phase-shift indicates the corresponding qubit states, $R_x(\theta)$ is the single qubit phase-shift of θ, and $\phi \equiv \phi_{\downarrow\downarrow} + \phi_{\uparrow\uparrow} - \phi_{\downarrow\uparrow} - \phi_{\uparrow\downarrow}$. When $\phi = \pi$, the phase gate can be transformed into the CNOT gate by applying certain single-spin gates, which are usually assumed much easier than the two-qubit gates.

As shown in Figure 22(b), to obtain the phase-shift, an optical pulse is applied to couple the state $|\downarrow\downarrow\rangle$ to the exciton state $|P, \frac{3}{2}, -\frac{3}{2}\rangle \equiv |\downarrow\downarrow\downarrow\rangle$. The pulse shifts the states by optical Stark effect and induces the phase shift $\phi_{\downarrow\downarrow}$. This pulse will also couple the electron state $(|\downarrow\uparrow\rangle + |\uparrow\downarrow\rangle)/\sqrt{2}$ to the exciton state $|P, \frac{3}{2}, -\frac{1}{2}\rangle \equiv (|\downarrow\uparrow\downarrow\rangle + |\uparrow\downarrow\downarrow\rangle + |\downarrow\downarrow\uparrow\rangle)/\sqrt{3}$, inducing a phase shift to $(|\downarrow\uparrow\rangle + |\uparrow\downarrow\rangle)/\sqrt{2}$ and thus the rotation between $|\downarrow\uparrow\rangle$ and $|\uparrow\downarrow\rangle$. To obtain a pure phase gate, another pulse (with the same energy and polarization as in the SWAP gate) coupling the states $(|\downarrow\uparrow\rangle - |\uparrow\downarrow\rangle)/\sqrt{2}$ and $|S, \frac{1}{2}, \frac{1}{2}\rangle \equiv (|\downarrow\uparrow\uparrow\rangle - |\uparrow\downarrow\uparrow\rangle)/\sqrt{2}$ can be used to compensate the rotation. Finally, the conditional phase-shift is $\phi \equiv \phi_{\downarrow\downarrow} - \phi_{\downarrow\uparrow} - \phi_{\uparrow\downarrow} = -\frac{1}{3}\phi_{\downarrow\downarrow}$. Similar to the case of the SWAP gate, a phase-shift gate can be realized with three pulses (including the optical Stark pulse) of duration of about 10 ps.

4.3. *Issues to be considered*

In realistic cases, there are several issues which could degrade the fidelity of the quantum gates.

The first one is the relaxation of the intermediate state by spontaneous emission. In the STIRAP [310], the spin states can be flipped without populating the exciton

state, which, however, cannot perform a general quantum gate since such a passage depends on the initial state of the spin. To have a general quantum gate which transforms a spin independent of the initial state, both the dark and bright states should be employed. To suppress the spontaneous emission and other scattering processes, it is preferable to have large detuning so as to minimize the population of the intermediate state [68,72,169,173].

Another important effect affecting the fidelity is the imperfection of the selection rules and the hole-mixing [71]. In realistic cases, the QDs would never have perfectly symmetric shape and thus the lateral confinement could cause mixing between states of different angular momentum (such as the HH–LH mixing), which is worse for the excited states involved in the two-qubit gates. Such effects, however, only induce systematic errors or unwanted dynamics to the quantum gates designed for ideal condition. In principle, the shapes, polarizations and timings of the controlling laser pulses can always be readjusted once the realistic system parameters have been measured. It could also be possible to design pulses of certain robustness against small deviations in the system parameters [120,314], and a scheme of using chirped pulse to implement quantum gates robust against the mixing effect has been proposed [71].

For QDs with reflection symmetry with respect to the growth plane, the imperfect selection rules may be tolerated by re-designing the polarization of the control light. In general cases, especially for small QDs which have irregular shapes, the hole mixing may be used as a resource for quantum control. In previous discussions in Section 4.1, a static magnetic field applied along a direction other than the growth direction has been required to break the rotation symmetry so that an arbitrary rotation of a single spin is possible. When the conservation of angular moment with respect to the growth direction is not perfect and thus the 'forbidden' transitions would be made partially 'allowed' due to the hole mixing, an effective magnetic field along an arbitrary direction for the spin could be induced by a properly polarized light beam through the AC Stark effect and an arbitrary rotation of a single spin could be realized even without a external magnetic field applied. More discussions about the hole mixing and its effects on the optical control are given in Appendix A.

The third problem with the scalability of the quantum computation is the complexity in the energy level structure of multi-dot systems. The analysis and characterization of the many levels with a number of excess electrons require much effort and furthermore [315–319], the optical pulses applied to a desired transition would inevitably affect the other transitions in QDs nearby, making the pulse design very demanding when the system becomes large. In femtosecond chemistry, learning algorithms haven been developed to design sophisticated pulses for controlling the complex atomic and molecular dynamics [320–322]. We expect the quantum learning algorithm be a powerful tool to deal with the design complexity in multi-dot systems.

With recent experimental progresses demonstrating the feasibility of optical control of single spins, the optical control of two spins for implementing two-qubit quantum gates is an immediate milestone for future experiments. Indeed, the recent systematic investigation of the optical transitions in coupled QD structures [268,315,317–319] has laid a cornerstone for this target.

5. Qubit initialization

A rapid and continuous supply of refreshed qubits is one criteria for scalable quantum computation [2]. Such a requirement is not only a prerequisite for the initialization of a quantum computer, but also a key element for quantum error correction where errors are continuously generated during the operation in noisy environments and by imperfect control. The initial preparation of a quantum computer could be done slowly, e.g., by simply cooling the system to very low temperature. For quantum error correction, however, rapid reset of qubits is crucial to recycle the spoiled qubits, otherwise a (infinitely) large number of fresh qubits should be prepared and preserved before a quantum computation commences so that the erroneous qubits could be replaced. The dynamical recycling strategy is more economical than a static supply of many qubits which deteriorate. It is desirable that the machine be as small as possible, with operation cost as trade-off.

The essence of qubit initialization is preparing a pure quantum state out of a mixed one. It amounts to cooling a qubit (ideally) to absolutely zero temperature. Thus the key physical process is dumping entropy to the environment. The aim is to build a quantum refrigerator in analogy to a reverse Carnot cycle. In general, the cycle consists of the following steps [120,256,257,323–326]: (1) pumping of the system to an excited state; and (2) relaxation of the excited system with entropy dumped into the environment. To initialize the spin qubit in an ultrafast timescale, a quantum channel capable of dumping entropy rapidly is required.

In a QD, the only available thermal baths for dumping the entropy of an electron spin are the nuclear spins, the host lattice (the phonon bath) and the electromagnetic environment (the photon bath). The coupling between the electron spin and the nuclear spins is very weak (with the rate in the order of $10^{-6}\,s^{-1}$), so only the phonon or photon bath could be used as entropy drain. The direct coupling of an electron spin with either the lattice vibration or the electromagnetic modes is known to be very weak. The solution is to transfer the spin state into orbital states which couple to the phonon or photon bath strongly. The entropy dissipation by rapid photon channel can be realized by optically pumping the spin states to a trion state and coupling the trion to a photon in a strongly coupled QD-microcavity-waveguide structure [120]. Or alternatively, excited trion states may provide an efficient entropy channel realized by the rapid phonon emission in QDs. Below we discuss these two possibilities.

5.1. *Initialization by entropy dumping to photon baths*

5.1.1. *Optical pumping*

The idea of initializing a spin by optical pumping is illustrated in Figure 23: an optical light brings one of the two spin states into a trion state, and then the trion state relaxes to either spin state by spontaneous emission. After sufficient cycling of the pumping process, the electron spin will be in the state that is not coupled to the trion state by the pump light, which has been demonstrated recently in experiments for single electron spins in QDs [256,257]. The scheme has also been applied to initialize single HH spins in QDs [255]. With essentially the same physics, optical pumping has also been used to initialize spins of NV centres in diamond [90,95].

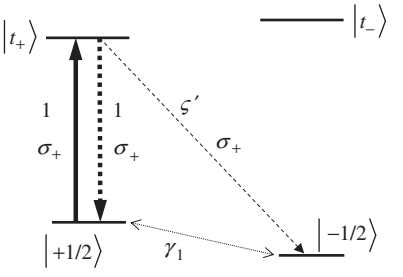

Figure 23. Optical pumping of a spin in the Faraday configuration. The solid line indicates the optical excitation, and the dotted lines indicate the spontaneous emission. The polarization and the relative dipole matrix element for each transition are indicated. The two spins states are connected by a spin-flip process with rate γ_1.

To selectively excite only one electron spin state, one can choose the light polarization so that one transition is 'forbidden' due to the selection rules. The selection rules are based on some symmetry, such as the (approximate) rotational symmetry about the growth direction. To exploit the selection rules resulting from the rotational symmetry, one can use a circularly polarized light. A σ_+ polarized light, e.g., couples the spin state $|+1/2\rangle$ to the trion state $|t+\rangle$ (Figure 23). Then the trion state will relax to both spin states by spontaneous emission. Now we have a dilemma: the selection rule prevents the spin state $|-1/2\rangle$ to be reached. But remember the selection rules we have are approximate and the 'forbidden' transitions are actually slightly allowed. According to the discussions in Appendix A, the trion state $|t+\rangle$ has a small probability ($\sim \zeta'^2$) to relax to the 'forbidden' state $|-1/2\rangle$. Also, due to the approximate selection rules, the state $|t-\rangle$ may be slightly excited, and the spin state $|-1/2\rangle$ can be excited by the σ_+-polarized light to the two trion states, which degrades the initialization efficiency. Furthermore, a magnetic field can be applied along the growth direction (i.e. in the Faraday configuration), so that all the transitions except the desired ones as depicted in Figure 23 are off-resonance from the pump light. Thus the pump process is characterized by several rates: the excitation rate G, the spontaneous emission rates Γ and $\tilde{\Gamma} \equiv \Gamma\zeta'^2$ (to the spin up and spin down states, respectively), and the longitudinal spin relaxation rate $\gamma_1 \equiv T_1^{-1}$. The rate equations for the trion population p_t and the electron populations in the two spin states $p_\pm$ are established as

$$\dot{p}_t = -\left(\Gamma + \tilde{\Gamma}\right) p_t + G p_+, \tag{17a}$$

$$\dot{p}_+ = -\gamma_1 p_+ + \gamma_1 p_- + \Gamma p_t - G p_+, \tag{17b}$$

$$\dot{p}_- = -\gamma_1 p_- + \gamma_1 p_+ + \tilde{\Gamma} p_t. \tag{17c}$$

The quality of the initialization may be quantified by two factors: the saturation time T_s and the saturation spin polarization P_s. In a typical GaAs or InAs QD at low temperature and under a moderately strong magnetic field, $\Gamma \sim 10^9\,\mathrm{s}^{-1}$, $\gamma_1 \sim 10^3\,\mathrm{s}^{-1}$ (see Section 2.3 for details), and $\zeta' \sim 1\%$ (for a unstrained dot [81], the value may be increased by strain [80]). Assuming the pumping rate $G \gg \Gamma$, we obtain by the rate

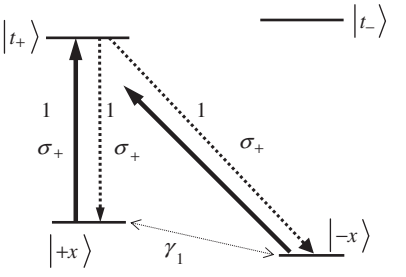

Figure 24. The same as Figure 23 except that the setup is in the Voigt configuration.

equations (note the trion population will eventually become spin up population when the light is switched off)

$$T_s \sim 10/\tilde{\Gamma} \sim 0.1\,\text{ms}, \tag{18a}$$

$$P_s \cong p_- - p_+ - p_t \approx 1 - 2\gamma_1/\tilde{\Gamma} \sim 98\%. \tag{18b}$$

Such a high degree of electron spin polarization by optical pumping has been experimentally demonstrated [256]. The initialization by optical pumping in the Faraday configuration, however, is rather slow and the saturation polarization is limited by the spin flip rate relative to the 'forbidden' spontaneous emission rate. Furthermore, the energy cost of the pump light is considerable. To see the energy cost of the optical pumping in the Faraday configuration, we notice that for just one useful photon emitted (which results in the target spin state), the number of photon wasted (by spontaneous emission resulting in the original state) is $\zeta'^{-2} \sim 400$ – only 0.25% energy of the pump light has been effective. The limiting factor is the small dipole moment for the 'forbidden' transition.

The solution is straightforward. One can work in the Voigt configuration in which a magnetic field is applied in plane to quantized the electron spins to be $|\pm x\rangle$ [118,257,325]. As shown in Figure 24, now both spin eigenstates are connected to a trion state by a σ_+-polarized excitation with the same dipole matrix element. The efficiency of optical pumping in the Voigt configuration can be discussed similarly to that in the Faraday configuration. But now there is another limiting factor of the saturation polarization: the backward optical excitation process from the target spin state to the trion state which, though off-resonance, is not negligible because of the large dipole matrix element. The generation rate of the trion by the off-resonance excitation is $\tilde{G} \equiv G\Gamma^2/\left(\Gamma^2 + \omega_c^2\right)$ where ω_c is the angular Lamor frequency of the electron spin in the magnetic field. The rate equations for the trion population P_t and the electron populations in the two spin states $P_\pm$ are established as

$$\dot{p}_t = -2\Gamma p_t + G p_+ + \tilde{G} p_-, \tag{19a}$$

$$\dot{p}_+ = -\gamma_1 p_+ + \gamma_1 p_- - G p_+ + \Gamma p_t, \tag{19b}$$

$$\dot{p}_- = -\gamma_1 p_- + \gamma_1 p_+ - \tilde{G} p_- + \Gamma p_t. \tag{19c}$$

Under the condition that $G \gg \Gamma \gg \tilde{G} \gg \gamma_1$ (e.g. $G = 10\Gamma$ and $\omega_c = 10^2\Gamma \sim 10^{11}\,\mathrm{s}^{-1}$), the efficiency of the initialization by optical pumping in the Faraday configuration is characterized by

$$T_s \sim 10/\Gamma \sim 10\ \mathrm{ns}, \tag{20a}$$

$$P_s \cong p_- - p_+ \approx 1 - \tilde{G}/\Gamma \sim 99.9\%. \tag{20b}$$

Owing to using the allowed transition in the Voigt configuration instead of the forbidden transition in the Faraday configuration, the spin initialization is faster by orders of magnitude. Also, the saturating polarization is much closer to unity since now the limiting factor is the off-resonance transition probability relative to the resonant one, instead of the spin-flip rate relative to the trion recombination rate due to the forbidden transition in the Faraday configuration. The off-resonance transition could be suppressed simply by enlarging the electron Zeeman splitting. There are calculations [325] and experiments [257] demonstrating efficient optical pumping of single electron spins in the Voigt configuration.

5.1.2. *Single-shot initialization with cavity enhancement*

In the previous discussion on spin initialization by optical pumping, we have seen that it is crucial to have a rapid entropy dumping channel to have efficient qubit cooling. The cooling duration of 10 ns is acceptable in many cases, but it is still highly desirable to have even faster spin initialization so that the qubit refreshing rate could catch up with the quantum gate and the error generation rate. Suppose the error rate per qubit per operation is about the quantum error correction threshold 10^{-3} and about 10 physical qubits are used to code one logical qubit to incorporate the error correction within the quantum logic. As we have discussed, the optical control for a simple quantum gate should take about 10 ps. That means we should have a qubit reset rate well above 1 qubit per nanosecond to avoid quantum computation being held up due to the lack of refreshed qubits. To have such ultrafast spin initialization, the entropy dumping channel should be specially engineered. One possible approach is to enhance the coupling to the photon bath by increasing the local density of states of photon modes. This enhancement is possible by putting a QD in the proximity of a microcavity [120]. As has been discussed earlier, a microphotonic structure is in any case needed to form a scalable large structure of QDs for distributed quantum computation. Here we discuss how the *in situ* cavity QED may be used to selectively enhance the photon emission for entropy dumping and hence for ultrafast spin initialization, following the procedure of Ref. [120].

The basic structure is depicted in Figure 25. To be specific, we consider a microring coupled to a QD. Such a structure may be constructed by etching a semiconductor surface where QDs are located. Structures in photonic crystals should be ideal alternatives (see Section 3.2). The specific structure, however, is not crucial to the physics to be discussed below. The attached microcavity would strongly modify the electromagnetic vacuum in the vicinity of the QD. The coupling to the cavity mode (which is taken as a whispering gallery mode) is realized due to the overlap between the QD and the evanescent wave of the cavity mode. A waveguide coupled to the cavity serves as a quantum channel for a cavity photon

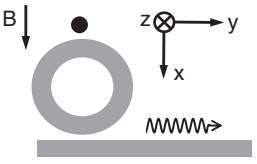

Figure 25. Schematics of the dot–cavity–waveguide coupling structure.

to escape rapidly to the environment. For the purpose of spin cooling, such a directional waveguide is not necessary, and actually one could as well use a cavity with large leakage (bad cavity situation). Since the emitted photon carries certain information about the qubit, a guided channel with cavity also enables such information to be retrieved, either for quantum measurement (as will discussed later) and for quantum error diagnosis. The incorporation of a waveguide along a cavity then involves extra designing and fabricating cost.

We consider the Voigt configuration. The energy diagram and optical transitions are shown in Figure 26. The spin eigenstates under a static magnetic field in the x-direction are denoted $|\pm\rangle$. The spin states may be flipped to the two degenerate trion (exciton plus an electron) states $|T\mp\rangle$ or $|T\pm\rangle$ by an X- or Y-polarized tipping pulse, respectively. The trion states are, by design, off-resonance from the cavity modes. We assume such off-resonance condition for several considerations: (1) It avoids the cavity-induced optical decoherence during quantum operations of the spin. (2) A local node usually consists of a number of QDs to a cavity, so it is unlikely to have all the QDs are in resonance with a cavity mode. (3) The resonance coupling may be realized by transient control via optical Stark effect which provides flexibility for selectively initialize a spin in a QD in the cluster. The relevant cavity mode is denoted by $|C\rangle$. The evanescent wave of the cavity mode is designed to be X-polarized in the vicinity of the nanodot, so that when brought within resonance, the trion states $|T\pm\rangle$ and the cavity states $|\mp, C\rangle$ are coupled into two split trion-polariton states, respectively. This provides a fast decay of the trion to a spin state by emitting a photon into the quantum channel. The pump light is Y-polarized so that a Raman pathway is formed from the spin state $|+\rangle$ to the trion state $|T+\rangle$ (by the optical pumping), to the cavity state $|-, C\rangle$ (by dot-cavity coupling) and to the spin state $|-\rangle$ (by spontaneous photon emission into the waveguide).

The optical cycle (similar to a reverse Carnot cycle) for cooling a spin qubit is illustrated in Figure 27 [120]. Without loss of generality, we assume that the electron before optical pumping is in an unpolarized state, i.e., $\hat{\rho}(-\infty) = 0.5|-\rangle\langle -| + 0.5|+\rangle\langle +|$. A cooling cycle consists of four basic steps:

(1) an X-polarized AC Stark pulse is adiabatically switched on, bringing the states $|T+\rangle$ and $|-, C\rangle$ into resonance by AC Stark effect.
(2) a Y-polarized pump pulse flips the spin up state $|+\rangle$ to the polariton states formed by $|T+\rangle$ and $|-, C\rangle$.
(3) the polariton states relax to the spin down state $|-\rangle$ rapidly by emitting a photon into the waveguide, dumping the spin entropy to the environment.
(4) the AC Stark pulse is adiabatically switched off. No photon-generation or spin-flip would take place if the initial spin state is $|-\rangle$.

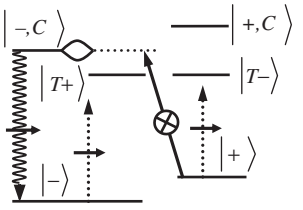

Figure 26. Basic optical processes for initializing a spin by controlled cavity QED. The dotted, solid and wavy arrows represent the AC Stark pulse (X-polarized), the tipping pulse (Y-polarized) and the spontaneous emission, respectively.

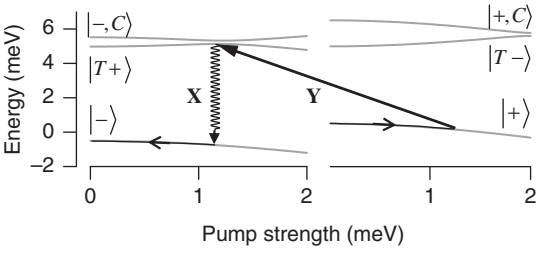

Figure 27. A quantum version of the reverse Carnot cycle for spin qubit initialization in a QD. The grey curves are the energies of different states versus the Rabi frequency of the AC Stark pulse, in the rotating frame (Adapted from R.B. Liu *et al*. Physical Review B, 72 (2005), p. 081306(R) [120]. Copyright © 2005 by the American Physical Society.).

Ideally, after one cooling cycle, the spin is fully polarized with the entropy mapped into the quantum channel, and the final density matrix becomes $|-\rangle\langle -| \otimes (0.5|0\rangle\langle 0| + 0.5|1\rangle\langle 1|)$, where $|n\rangle$ is the n-photon waveguide state. This is an idealization of the single-shot initialization of a spin qubit in a QD. In reality, the single-shot initialization is subject to errors due to the spontaneous emission of photons into free space, by which the trion state may relax to either spin state depending on the polarization of the emitted free-space photon, while the cavity photon couples only the transition to the target spin state.

The whole system under the optical control is described by the Hamiltonian

$$\begin{aligned}\hat{H} \equiv{}& \Omega_C \hat{a}^\dagger \hat{a} \pm \frac{\omega_c}{2}|\pm\rangle\langle\pm| + \Omega_T|T\pm\rangle\langle T\pm| + (g_{\text{cav}}|T\pm\rangle\langle\mp|\hat{a} + \text{H.c}) \\ &+ \left[\chi_t(t)\mathbf{e}_t + \chi_p(t)\mathbf{e}_p\right]\cdot\mathbf{e}_X(|T\pm\rangle\langle\mp| + r_C\hat{a}^\dagger) + \text{H.c} \\ &+ \left[\chi_t(t)\mathbf{e}_t + \chi_p(t)\mathbf{e}_p\right]\cdot\mathbf{e}_Y|T\pm\rangle\langle\pm| + \text{H.c},\end{aligned} \tag{21}$$

where $\hat{a}$ is the cavity mode annihilation operator, Ω_C the cavity mode frequency, Ω_T the bare trion state frequency, ω_c the electron Zeeman splitting, g_{cav} the coupling between the cavity and the QD, χ_p the Rabi frequency of AC Stark pulses with polarizations $\mathbf{e}_p$, χ_t the Rabi frequency of the pump pulse with polarization $\mathbf{e}_t$ and r_C the strength of the direct coupling between the light pulse and the cavity mode (relative to the coupling to the trion state).

The dynamics in the cavity-dot system is rather complicated and some attention should be paid to the designing of the controlling pulses. To bring the trion state into

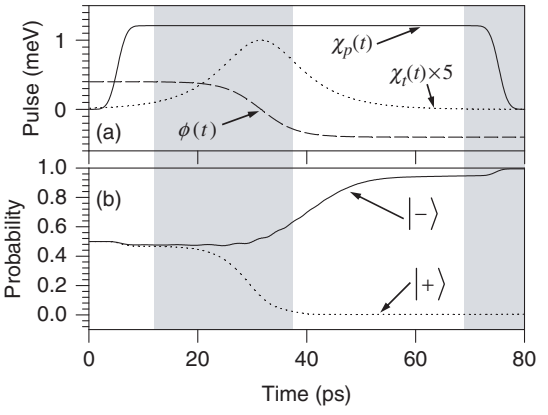

Figure 28. (a) The Rabi frequencies of the AC Stark pulse and the tipping pulse (amplified by a factor 5), and the sweeping frequency of the tipping pulse. (b) Probabilities of spin down and up. Different steps of the cooling cycle, indicated by ①–④, are distinguished by shadowed areas. (Adapted from R.B. Liu *et al.* Physical Review B, 72 (2005), p. 081306(R) [120]. Copyright © 2005 by the American Physical Society.).

the resonance with the cavity mode and to maintain the resonance, the AC Stark pulse is designed to have an almost square profile. Also, the switch-on and off of the pulse should be made smooth enough to avoid non-adiabatic excitation of the trion states from the target spin state. We choose the pulse to be of the profile

$$\chi_p(t) = \chi_p e^{-i\Omega_p t}[\mathrm{erf}(\sigma_p(t-t_1)) - \mathrm{erf}(\sigma_p(t-t_2))], \tag{22}$$

(Figure 28a). As the AC Stark pulse maintains the resonant cavity-dot coupling which facilitates the photon escape to the quantum channel, the trion state relaxes very fast (on the timescale of g_{cav}^{-1} and γ^{-1}, ~10 ps). The flipping pulse should be a π-pulse for Rabi rotation between $|+\rangle$ and $|T+\rangle$. Due to the dynamical nature of the states (dressed by the AC Stark pulse) and the rather small polariton splitting (~0.1 meV), a perfect π-rotation requires an extremely long pulse. In principle, a full excitation of the spin up state to the polariton states could be made much faster by pulse shaping. One of such pulse shaping is to use geometrical control of the transition which is robust against uncertainty of the polariton frequencies. The geometrical control is realized by using a chirped pulse as $\chi_t(t) = \chi_t e^{-i\phi(t)-i\Omega_t t}$ sech $(\sigma_t(t-t_t))$ with the phase sweeping rate $\dot{\phi}(t) = -\sigma_c \tanh(\sigma_t(t-t_t))$ [314]. The frequency of the pulse now will sweep from σ_c above Ω_t to σ_c below and the sweeping range $[\Omega_t - \sigma_c,\ \Omega_t + \sigma_c]$ covers both of the trion–polariton states. The initial spin state $|+\rangle$ will be brought adiabatically into a superposition of the two polariton states, which relaxes rapidly to the target spin state $|-\rangle$. Such a geometrical flip can also tolerate to some degree laser fluctuations and uncertainty in the dipole moment, transition energy and selection rules.

The cooling process is simulated by numerically solving the master equation of the dot-cavity system

$$\partial_t \hat{\rho} = -i[\hat{H}, \hat{\rho}] - \frac{\gamma + \gamma'}{2}\mathcal{L}_{\hat{a}}\hat{\rho} - \frac{\Gamma}{2}\sum_{s,s'=\pm}\mathcal{L}_{|s\rangle\langle Ts'|}\hat{\rho}, \tag{23}$$

where $\mathcal{L}_{\hat{o}}\hat{\rho} \equiv 2\hat{o}\hat{\rho}\hat{o}^{\dagger} - \hat{o}^{\dagger}\hat{o}\hat{\rho} - \hat{\rho}\hat{o}^{\dagger}\hat{o}$ denotes a Lindblad superoperator, γ the cavity-waveguide escape rate, γ' the cavity-free-space loss rate and Γ the trion decay rate due to spontaneous emission into free-space. The multi-photon cavity states were included in the numerical calculation, as they renormalize the AC Stark shift (the real excitation of multi-photon states is negligible due to the off-resonance condition). Inclusion of up to 3-photon states was found sufficient to obtain converged results.

We test the cooling efficiency with a set of realistic parameters [120]. The Zeeman splitting $\omega_c = 1\,\text{meV}$, $\gamma = 0.2\,\text{meV}$, $\gamma' = 0.045\,\mu\text{eV}$ (corresponding to an intrinsic Q-factor $\sim 3 \times 10^7$), the dot-cavity coupling $g_{\text{cav}} = 0.1\,\text{meV}$, the cavity–trion detuning $\Omega_C - \Omega_T - \omega_L/2 = 0.5\,\text{meV}$, $\Gamma = 1\,\mu\text{eV}$ and $r_C = 0.3$. For the parameters given above, the trion state $|T+\rangle$ and the cavity state $|-, C\rangle$ are brought into resonance when the AC Stark pulse strength ($2\chi_p$) is maintained at 1.21 meV. Maintaining the resonance for $t_2 - t_1 = 70\,\text{ps}$ is found sufficient for the total dissipation of the photon. The spectral width of the AC Stark shift pulse ($\sigma_p = 0.354\,\text{meV}$) is set much smaller than the detuning ($\Omega_T + \omega_L/2 - \Omega_p = 5.5\,\text{meV}$), so that the excitation due to non-adiabatic switch-on and off is negligible. The flipping pump pulse has a frequency sweep range of $\sigma_c = 0.4\,\text{meV}$, strength $\chi_t = 0.2\,\text{meV}$, and duration $1/\sigma_t = 6.58\,\text{ps}$. The spin state $|+\rangle$ is flipped to the polariton states with negligible error.

Figure 28(b) shows that a single-cooling cycle completed within 80 ps produces an almost 100% polarized spin from a maximally mixed state. The density matrix at the end of the cycle is $\hat{\rho} = 0.9945|-\rangle\langle -| + 0.0040|+\rangle\langle +| + \hat{\rho}_{\text{err}}$, where $\hat{\rho}_{\text{err}}$ is the probability ($\approx$0.15%) of the system remaining in the trion states which results mainly from the non-adiabatic switching of the AC Stark pulse. The extra error ($\approx$0.4%) comes mainly from the decay of the trion with photon emission into free space.

5.2. *Initialization by entropy dump to phonon baths*

The phonon bath in a QD is often taken as a source of the qubit decoherence, but it can also be used as as a resource for ultrafast cooling. The electronic energy levels in QDs are discrete, it has been argued that the phonon emission would be much suppressed due to the lack of available final states fulfilling the energy conservation [327]. This so-called phonon bottleneck effect, because of its importance in QD lasers and detectors, has been extensively studied both in experiments and in theories. Nonetheless, experiments have established various mechanisms for rapid relaxation of electrons from exited states to the ground states, such as the Auger-process and the multi-phonon process [328]. The observed relaxation time varies from tens of picoseconds to a few picoseconds [329,330]. The spin relaxation, especially for holes due to the large spin-orbit coupling, always accompanies with the energy relaxation, for the mixing in the excited states is much stronger than in the ground states. Thus we can use the phonon emission as fast entropy dumping channel for an electron spin in a QD.

A cycle of the spin initialization is illustrated in the inset of Figure 29:

(1) a circularly polarized laser pulse resonantly pumps the electron states to an excited trion state.

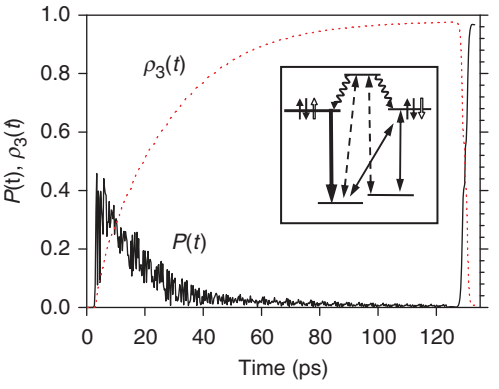

Figure 29. The numerical simulation of a typical initialization cycle using phonon emission from excited trion states. Inset: Schematics for the spin initialization process.

(2) the excited trion state relaxes rapidly to the ground trion states $|\uparrow\downarrow\Uparrow\rangle$ and $|\uparrow\downarrow\Downarrow\rangle$. During the relaxation, the hole spin is not conserved due to the strong HH–LH mixing in the excited state, and without loss of generality we assume the rate is the same for the relaxation to the two ground trion states.
(3) to deplete the population of one of the ground trion states, a circularly polarized laser pulse is applied to resonantly couple, e.g. the trion state $|\uparrow\downarrow\Downarrow\rangle$ to the electron spin state $|\uparrow\rangle$.
(4) after a period of pumping and relaxation, the population will be accumulated to the trion state $|\uparrow\downarrow\Uparrow\rangle$, and, thus, an ultrafast π-pulse can be applied to flip the trion state into a pure electron spin state.

The most time-consuming step of this laser cooling process is the pump and relaxation processes which is limited by the carrier relaxation rate and the pump strength. Care should be taken to avoid the population being trapped in some dark state which could be possible in the strongly driven multi-level system (similar to the electromagnetically induced transparency effect). Figure 29 shows a typical spin initialization cycle in which the spin is pumped from a fully mixed state to a nearly fully polarized state in 120 ps (the polarization at the end of the cycle is about 97%), where $\rho_3(t)$ is the population stored in the ground trion state $|\uparrow\downarrow\Uparrow\rangle$, and $P(t)$ is the polarization of the electron spin. The pump strength for the excited and ground trion states has been set to be 2 meV and 0.5 meV, respectively, the carrier relaxation time is 2 ps, and the spontaneous emission time is 1 ns. The π-pulse flipping the trion state into the spin state is chirped for optimized performance.

The phonon baths offer an alternative solution of ultrafast spin initialization with comparable speed to a photon bath enhanced by cavity QED. The real excitation of the excited electron and hole states, however, could cause some complications. One such issue is the trapping of electrons and holes in the dark states, which cause the loss of a spin qubit. And in fluctuation QDs, it is not likely the excited state energy is high enough for LO phonon emission.

6. Quantum non-demolition measurement of spin qubits

The result of a quantum algorithm is obtained by quantum measurement of specific qubits. To diagnose the errors generated in quantum error correction, quantum measurement is also needed.

In current single-spin experiments in QDs [79,256,273,326,331–333] and in diamond color centres [88], the measurement is usually achieved by cycling read of the spins, which amounts to time-ensemble measurement. Remarkably, efficiency enhancement in measurement of NV centre spins in diamond has been made using ancillary nuclear spin qubits [265,266], but the single-shot measurement still remains illusive.

Eventually, single-shot measurement of quantum registers is demanded for scalable quantum computation for large-scale problems. In Appendix C, we show that quantum non-demolition (QND) measurement, even with certain errors, may be converted to a single-shot measurement and thus is scalable. To realize single-shot measurement, the crucial issue is how to enhance the coupling between the probe (e.g. photons) and the spin qubits. Below we provide a possible solution of using cavity QED, which may be implemented *in situ* in a quantum network (discussed in Section 7). The discussion is based on QD cavity-QED systems, but may be readily extended to NV centres where cavity-QED have been also demonstrated [260].

6.1. *Scalability of quantum measurement in quantum computation*

In quantum computation (such as in Shor's algorithm [1,172]), the quantum register could be in a superposition state right before the measurement $|\Psi\rangle = \sum_x C_x|x\rangle$, where $|x\rangle \equiv |x_1,\ x_2, \ldots, x_N\rangle$ is a computational basis state for the N-qubit register. The measurement should be in the computational basis which returns any $|x\rangle$ contained in the superposition and the computation result is derived from the measured x. If an algorithm requires the measurement of the wavefunction C_x, i.e., the tomography of the quantum state, it would be an analogue computation instead of a digital one, and much worse, it would not be scalable as the number of measurements would increase exponentially with the number of qubits in the register to be measured [334]. Such measurements are ensemble measurements.

A point we would like to put forward here about the scalability of quantum measurement in quantum computation is that an ensemble measurement is not scalable in the sense that the size of the ensemble would increase exponentially with the problem size (defined as the number of qubits registering the computation result involving a quantum measurement) [120]. It has been well-known that an ensemble quantum computation is not scalable if the qubits cannot be initialized to a pure state [335]. The issue of scalability associated with the ensemble measurement [120], however, has received less attention in spite of its importance in quantum computation. This problem is briefly explained below, and more detailed discussion is given in Appendix C.

First we notice that the uncorrelated ensemble measurement cannot be used to read out the quantum register in general algorithms (especially for those terminating in superposition states, such as Shor's algorithm). In an uncorrelated measurement, the spins are measured independently. Thus, in general which basis states are in the

superposition cannot be deduced from the measured result. For example, the superposition state $|000\rangle + |111\rangle$ will give the same uncorrelated measurement result as the state $|000\rangle + |011\rangle + |101\rangle + |110\rangle$. In some algorithms, such as Shor's algorithm for factorization, the number of basis states in the superposition may increase exponentially with the number of qubits, thus the number of possible superposition states yielding the same uncorrelated measurement result would increase exponentially with the number of qubits measured. So the quantum measurement has to be a correlated one (e.g., the photon counting should be in coincidence) to be scalable. If a coincidence measurement is a destructive one, the procedure has to be run from the very beginning in each repetition, and the superposition state can collapse into any possible $|x\rangle$, which is in general different from one cycle to another. To have a certain x to be measured at least twice for the sake of confidence, the number of repetitions to be performed should be in the order of the number of basis states in the superposition, which again could be an exponential function of the problem size. In conclusion, the enhancement of signal-background contrast by ensemble quantum computation is not a scalable solution.

In realistic cases, the signal of a single-shot measurement of a single quantum object is usually too weak to be distinguished from noise. Thus the signals are to be amplified either by simultaneously measuring a large number of identical 'quantum computers' running the same quantum program or by repeating the quantum program under identical conditions for a large number of times. This renders the quantum computation to be an ensemble one and hence not scalable.

Using ensemble measurement as a solution to the detection efficiency problem has been applied in various systems, including nuclear spins in liquid-phase NMR [335] or solid-state NMR [62]. Here we consider quantum computing with optically controlled spins. The spin-dependent absorption (or other optical methods such as spin-dependent scattering and Faraday rotation) may be used to measure a single spin in a QD, in which a probe pulse resonant with the spin-trion transition in a QD measures the spin in the computational basis by detecting whether or not a single photon of the probe pulse has been absorbed. To measure a register with many qubits, the probe should be composed of many pulses in which each pulse addresses a QD individually by spatial and spectral resolution. In practice, the interaction between the probe pulse and a single spin is very weak, and also photon collection and detection efficiency is less than one, so the information obtained about a spin is on the average much less than one bit. The probe measurement has to be repeated for many times to accumulate statistical confidence in the measured result (or signal-to-noise ratio). Considering the fact that the probe process is destructive to the spin state (since a trion state excited by the probe pulse may return to either spin state regardless of the original spin state), the repetition has to be run from the very beginning of the quantum computation which prepares the quantum computer to the same superposition state. This makes the quantum computation an ensemble one, which in general is not scalable.

Nonetheless, the ensemble measurement could still be useful in demonstrating quantum algorithms for small-size problems. For instance, as will be shown later, to demonstrate Shor's algorithm for factorizing 15 by optical control of electron spins in QDs, the program would be completed in less than a few nanoseconds, and the number of computational basis states in the superposition is less than 10.

A commercial Ti-sapphire pulse laser with repetition rate of about 100 MHz could be used to carry out an ensemble of repeated running and measurement in a reasonably short time in a pump–probe configuration, where the initialization and gate control are viewed as a single complex pump pulse and the probe pulse is composed of many frequency components (and detected in multi-channels).

6.2. *QND measurement via cavity QED*

In essence, the realization of an efficient single-shot quantum measurement involves two key elements: rapid quantum state entanglement of the target qubit (here a spin in a QD) with a detectable information carrier (such as a photon), and efficient and faithful collection of the information carrier (such as by a photon detector with a high efficiency and a low dark count rate). Errors in the measurement, due to the efficiency or dark count problems, e.g., cannot be fully eliminated. Thus cycling of single-shot measurement is required to accumulate statistical confidence. As discussed in Appendix C, the cycling of single-shot measurement is scalable when the measurement is a QND one, i.e. the qubit state after the measurement is (ideally) an eigenstate in the measurement basis corresponding to the measurement output.

The QND measurement being rapid is an essential element in the following sense: the cycling of measurement has to be completed in a time much shorter than the qubit is significantly disturbed by the environment. So we should look for a rapid quantum information transfer between the spin qubit and a medium to be detected. An ideal medium is photons. The cavity-enhanced entropy dumping in the ultrafast initialization is indeed a rapid information transfer (but there the information has been viewed as noise). Thus the ultrafast spin initialization and rapid QND may be integrated in the same microphotonic structure [120].

To ensure efficient detection of the transferred quantum information, the photons escaped from the cavity should be directed into a quantum channel, unlike in the initialization process where it does not matter which direction the dumped entropy flows. To realize such a directional information flow, a waveguide could be fabricated in the proximity of the cavity, and the waveguide may be coupled to a fibre which conducts the photon to a detector [295–301].

The optical control of the cavity-QED for a rapid measurement is similar to that for the ultrafast initialization [120]. But to enable measurement cycling, the measurement should be non-destructive, i.e. the spin basis state should return back to its initial state after a cycle of measurement, with close to unity probability. Thus we need to switch the polarizations of the tipping and the AC Stark pulses from (Y, X) to (X, Y), respectively. The energy diagram with optical transitions indicated is shown in Figure 30. A measurement cycle may be processed in four basic steps (Figure 31):

(1) an X-polarized tipping pulse flips the spin state $|+\rangle$ to the trion state $|T-\rangle$.
(2) a Y-polarized AC Stark pulse adiabatically switched on drives the trion state into resonance with the cavity state $|+, C\rangle$.

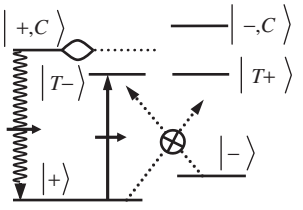

Figure 30. Basic optical processes for QND measurement of a spin by controlled cavity QED. The dotted, solid and wavy arrows represent the AC Stark pulse (*Y*-polarized), the tipping pulse (*X*-polarized) and the spontaneous emission, respectively.

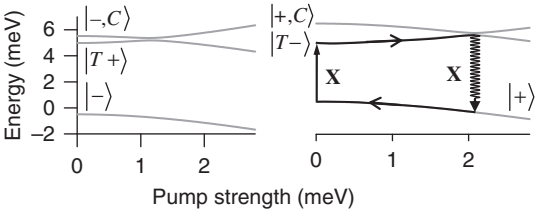

Figure 31. Detailed optical process for the measurement cycle. The grey curves are the energies of different states versus the Rabi frequency of the AC Stark pulse, in the rotating frame. (Adapted from R.B. Liu *et al.* Physical Review B, 72 (2005), p. 081306(R) [120]. Copyright © 2005 by the American Physical Society.).

(3) the trion state resonantly tunnels into the cavity state and relaxes rapidly back to the spin state $|+\rangle$, leaving a photon emitted into the quantum channel.
(4) the AC Stark pulse is adiabatically switched off.

Suppose that the spin state to be measured is $\alpha|+\rangle + \beta|-\rangle$ and the channel is initially in the vacuum state $|0\rangle$. An ideal measurement process will transform the system into the entangled state $\alpha|+\rangle|1\rangle + \beta|-\rangle|0\rangle$, so that the detection of the photon projects the electron into a spin basis state, providing a QND measurement of the spin. Note that the pulse timing for measurement is different from that for cooling (cf. Figures 28a and 32a). In the measurement cycle, the flipping pulse need not be chirped, since here the Rabi flop occurs between stationary energy levels and the transition between the spin state and the trion is well-separated in frequency from the cavity mode. Instead, a simple Gaussian π pulse $\chi_t(t) = \chi_t e^{-\sigma_t^2(t-t_t)^2/2-i\Omega_t t}$ may be used. The AC Stark pulse chosen is *Y*-polarized to avoid direct excitation of the cavity mode.

Numerically simulation is done to check the efficiency of the measurement cycle [120]. Since the initialization and the QND measurement are supposed to be operated via the same photonic structure, the simulation is done with the same physical structure as that in Figure 28. The number of photons emitted into the waveguide is calculated with $\partial_t n = \gamma\langle\hat{a}^\dagger\hat{a}\rangle$. The tipping and the AC Stark pulses are set such that $1/\sigma_t = 2.19\,\text{ps}$, $\chi_t = 0.192\,\text{meV}$, $\Omega_t = \Omega_T - \omega_L/2$, $\sigma_p = 0.707\,\text{meV}$, $2\chi_p = 2.08\,\text{meV}$, $\Omega_T + \omega_L/2 - \Omega_p = 5.5\,\text{meV}$ and the duration of the pump pulse

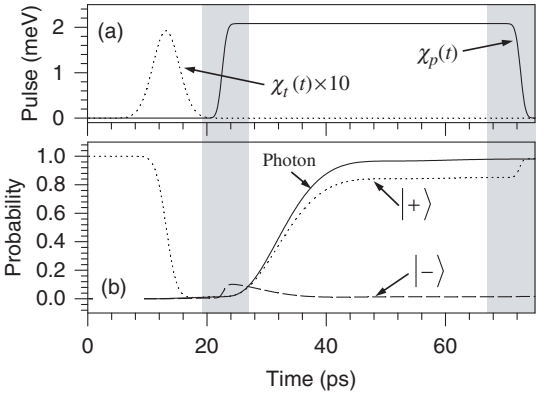

Figure 32. (a) The Rabi frequencies of the AC Stark pulse and the tipping pulse (amplified by a factor 10). (b) Probabilities of spin down and up, and the number of waveguide photons, for a spin initially polarized up. Different steps of the cooling cycle, indicated by ①−④, are distinguished by shadowed areas. (Adapted from R.B. Liu *et al.* Physical Review B, 72 (2005), p. 081306(R) [120]. Copyright © 2005 by the American Physical Society.).

$t_2 - t_1 = 50$ ps. After a single cycle of measurement, an initial state $\hat{\rho}_0 = |+\rangle\langle+|$ results in the final state $\hat{\rho}_1 = 0.0161|-\rangle\langle-| + 0.9824|+\rangle\langle+| + \hat{\rho}_{\text{err}}$ with the number of photon emitted into the waveguide $n = 0.9806$ (Figure 32b), while an initial state $\hat{\rho}_0 = |-\rangle\langle-|$ results in the final state $\hat{\rho}_1 = 0.9955|-\rangle\langle-| + 0.0040|+\rangle\langle+| + \hat{\rho}_{\text{err}}$ with $n = 0.0015$ (not shown). The photon emitted into the waveguide can be detected with high efficiency. If the detector has a zero dark-count rate and an efficiency of 50% [336], the positive operator-valued measures (POVM; [172], see Appendix C for more discussions) for the measurement process can be defined as

$$\hat{P}_- = 0.9992|-\rangle\langle-| + 0.5097|+\rangle\langle+|, \tag{24a}$$

$$\hat{P}_+ = 0.0008|-\rangle\langle-| + 0.4903|+\rangle\langle+|, \tag{24b}$$

for a non-click or click event, respectively. Within 5 measurement cycles, e.g, the spin state is measured with accuracy higher than 97%, and the back-action noise to the spin is less than 10%, while the time duration is less than 0.4 ns, much shorter than the spin decoherence time.

The QND measurement of single spins can thus be completed within 100 ps, and the high efficiency of collecting and detecting photons propagating in waveguides enables a near unity accuracy by repeating the single-shot measurement for only a few times. The measurement is still subject to the problem of less than unity efficiency as well as back-action noise. As discussed in Appendix C, quantum gates and error tolerating coding can be combined to achieve a sufficiently faithful measurement of a qubit without rewinding a quantum computing program.

7. Networking local nodes

In Section 3.2, we have introduced the dot–cavity–waveguide coupled structure for distributed quantum information processing. Quantum nodes are formed by clusters

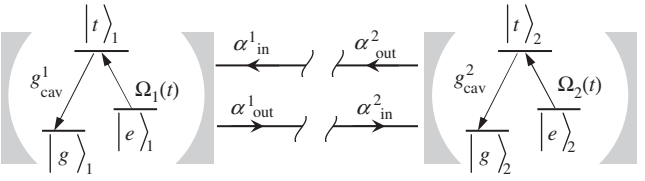

Figure 33. Illustration of state transfer in a quantum network. The node is composed of a cavity coupled to a three-level Λ system. The two ground states $|g\rangle$ and $|e\rangle$ of the three level systems form the Hilbert space for the stationary qubits. State $|g\rangle$ is coupled to the intermediate $|t\rangle$ by the cavity mode with strength g_{cav} and $|e\rangle$ to $|t\rangle$ by a classical light with Rabi frequency $\Omega(t)$. Direct excitation of cavities by the classical light is assumed absent. The cavities themselves are coupled to the outside continuum which forms a photonic channel. Two nodes are connected by the photonic channel in the following way: the output of node 1 is directed to node 2 as its input and vice versa. (Adapted from W. Yao *et al.*, Journal of Optics B: Quantum and Semiclassical Optics, 7 (2005), p. S318 [347]. Copyright © 2005 by the Institute of Physics.)

of singly charged QDs with electron spins as carriers of stationery qubits. Single photons in optical waveguides or fibres can transport quantum information between distant nodes. Interfacing between single spins in QDs and single photons is made possible by the strong photon confinement in solid state microcavities.

The separation between quantum nodes on a single chip which can range from $\sim$ micrometre to $\sim$ centimetre allows parallel optical control, and intra-chip communication is realized by optical waveguides. Inter-chip communication is possible by wiring chips together with optical fibres [337–339]. For intra-chip communication and short distance inter-chip communication, the decoherence of the photon qubit is negligible [340–342]. Thus, it is possible and also highly desirable to perform inter-node operations in a deterministic way (to be contrasted with most quantum cryptography and linear optics quantum computation schemes based on projective measurement which renders the logical controls probabilistic). The key component is a quantum interface that allows the deterministic state transfer between spin and photon qubit.

The prototype quantum interface for this purpose was proposed by Cirac *et al.* [277]. It is composed of a cavity coupled to a three-level Λ system, illustrated in Figure 33. The two ground states, $|g\rangle$ and $|e\rangle$, of the three level system form the stationary qubit. State $|g\rangle$ is coupled to the intermediate state $|t\rangle$ by the cavity mode and $|e\rangle$ to $|t\rangle$ by the external laser field. Direct excitation of cavity by the external laser is assumed absent. Through the imperfect mirror, the cavity is coupled to the electromagnetic continuum which forms a photonic channel. A Raman path from $|e\rangle$ to $|g\rangle$ through the intermediate state $|t\rangle$ is thus formed. If the three level system is initially in state $|e\rangle$, an external laser pulse can bring it to state $|t\rangle$ by a π rotation which relaxes to state $|g\rangle$ by spontaneous emission of a cavity photon. The cavity photon then goes into the photonic channel forming a single photon wavepacket. If the three level system is initially in state $|g\rangle$, it will remain in this state provided the cavity is in its vacuum. The quantum state carried by the three-level system is thus mapped into the photon number subspace of the outgoing photon,

$$\big(C_g|\,g\rangle + C_e|e\rangle\big) \otimes |\text{vac}\rangle \rightarrow |\,g\rangle \otimes \big[C_g|\text{vac}\rangle + C_e|\alpha_{\text{out}}\rangle\big], \tag{25}$$

where $|\alpha\rangle$ denotes a single photon wavepacket in the photonic channel and $|\text{vac}\rangle$ the channel vacuum. This process forms the basis for the sending function (i.e. the mapping from a stationery qubit to a flying qubit) of a quantum node. The receiving function is the mapping from a flying qubit to a stationary qubit and can be realized as the time reversal of a sending process,

$$|g\rangle \otimes (C_g|\text{vac}\rangle + C_e|\alpha_{\text{in}}\rangle) \rightarrow (C_g|g\rangle + C_e|e\rangle) \otimes |\text{vac}\rangle. \tag{26}$$

With the output of the sending node directed as the input of the receiving node (Figure 33), transfer of qubits between two distant nodes can be performed.

This quantum network by cavity QED was originally proposed for quantum computation with atomic systems [277]. Critical experimental steps towards realizing such a quantum interface in atom-cavity QED systems have been progressively demonstrated [153,154,343], including the initial demonstration of reversible state transfer between photons and atoms [344]. Via similar cavity-assisted Raman processes, schemes for mapping between motional states of single trapped atoms [345] or collective excitation of atomic ensembles [346] and the quantum states of single photons are also proposed.

For quantum computation with QD spins [63], deterministic quantum network control is indeed possible in the distributed structure discussed previously in Section 3.2. In Section 7.1, we will first show how to realize such a prototype quantum interface between a QD electron spin and a photon mode in a waveguide/fibre. In Section 7.2, we will describe the exact solution to the interface dynamics between a spin qubit and a photon qubit in the prototype quantum node in the most general scenario. Control schemes based on the exact solution form the basis of a variety of inter-node operations in quantum networks as discussed in Section 7.3. The issue of unavoidable inhomogeneity of solid-state quantum nodes is properly resolved with the exact interface solution. In Section 7.4, we study the effects of various sources of errors on the interface operations. A summary and outlook are given in Section 7.5.

7.1. *Dot-cavity-waveguide structure as spin-photon interface*

Here we show how to implement a dot-cavity-waveguide coupled structure as a deterministic quantum interface for single spins in QDs and single photons in waveguides.

The coupled structure can be realized with any of the microcavity systems discussed in Section 3.2. In Figure 34(a), a QD sitting in the evanescence field of whispering gallery mode of a ring cavity is illustrated as an example. There are two essential requirements for such a coupled structure to be an efficient interface. First, the dot-cavity coupling must have a large Purcell factor, so that the QD optical transitions are dominantly coupled to the cavity field. Second, the leakage of the cavity photon into free space should be small as compared with the tunnelling into the attached waveguide. If both conditions are fulfilled, the evolution through the desired quantum pathway, i.e. QD trion $\leftrightarrow$ cavity photon $\leftrightarrow$ waveguide photon, occurs on a much faster timescale than the leakage out of it [119,120]. Lowering of the cavity Q-factor due to the coupling to the waveguide is part of the process and has no deleterious effects on the quantum operation. The cavity with the reduced

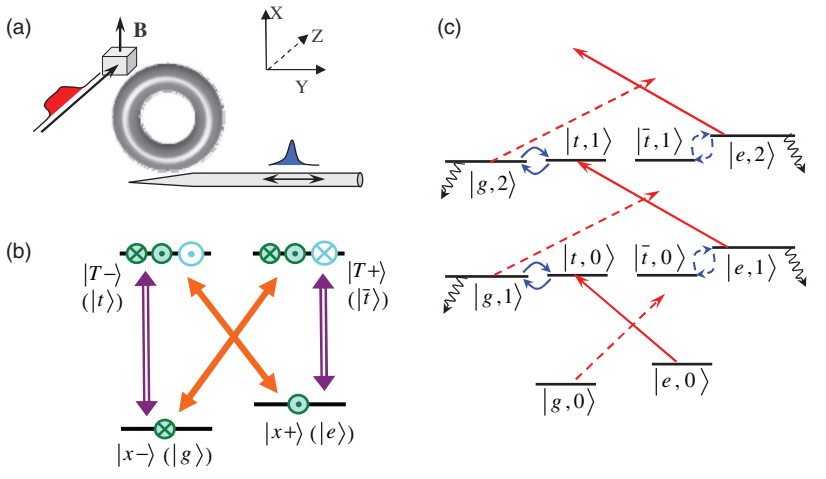

Figure 34. (a) A high-Q microring coupling a 'tapered' waveguide and a singly charged QD. (Adapted from W. Yao *et al.*, Physical Review Letters, 95 (2005) p. 030504 [119]. Copyright © 2005 by the American Physical Society.) (b) Optical selection rules in the basis where spins are quantized along the field (x) direction. The hollow two-headed arrow denotes X-polarized light and the solid arrow denotes Y-polarized light. (c) The level diagram and optical process. In $|s,n\rangle$, $s=g$, e, t or $\bar{t}$ denotes an electronic state in the dot and n denotes the number of photons in the single cavity mode. (Adapted from W. Yao *et al.*, Physical Review Letters, 95 (2005) p. 030504 [119]. Copyright © 2005 by the American Physical Society.) Straight, curved and wavy arrows represent the laser excitation, dot–cavity coupling and cavity-fibre tunnelling, respectively. The resonant and off-resonance processes are represented by solid and dashed lines, respectively.

Q-factor is *not* required to be in the strong coupling regime [119,347,348]. This will become clear when we discuss the control of this interface in the following sections.

The qubit is represented by the two spin states $|x-\rangle$ and $|x+\rangle$ and spin manipulations are mediated by the two trion ground states $|T-\rangle$ and $|T+\rangle$ (see Section 2.2). In the convention of the prototype quantum interface, the two spin states are also denoted here as $|g\rangle$ and $|e\rangle$ respectively, and the two trion states $|T+\rangle$ and $|T-\rangle$ as $|t\rangle$ and $|\bar{t}\rangle$, respectively. While $|g\rangle$ and $|e\rangle$ have energies ω_g and ω_e in a static magnetic field normal to the optical axis of the dot (Figure 34a), $|t\rangle$ and $|\bar{t}\rangle$ typically have a much smaller energy splitting ($\omega_t \simeq \omega_{\bar{t}}$) in GaAs fluctuation dot because of its negligible in-plane g-factor of the HH [200,351], but a splitting comparable to the electron's in self-assembled InAs dot [257].

By design, the selected cavity mode of frequency ω_c is X-polarized in the vicinity of the QD and a Y-polarized control laser of central frequency ω_L and complex Rabi frequency $\Omega(t)$ directly couples to the QD transitions [230,308]. Therefore, by the selection rules shown in Figure 34, the cavity field couples only to the straight transitions $|g\rangle \rightarrow |t\rangle$ and $|e\rangle \rightarrow |\bar{t}\rangle$, and the controlling laser couples only to the cross transitions $|g\rangle \rightarrow |\bar{t}\rangle$ and $|e\rangle \rightarrow |t\rangle$. The laser light and cavity mode satisfy the two-photon resonance condition: $\omega_L + \omega_e = \omega_c + \omega_g$. The Raman detuning $\Delta \equiv \omega_t - \omega_L - \omega_e$ is also much smaller than the electron Zeeman splitting $\omega_e - \omega_g$. Thus, by the Zeeman splitting and the selection rules, the trion state $|\bar{t}\rangle$ is off-resonance to the laser light and the cavity mode (shown by dashed lines in the Figure 34(c)).

At a sending node, the Raman process consists in first the laser field exciting the spin state $|e,0\rangle$ to the trion state $|t,0\rangle$, then the trion state resonantly coupled to the cavity state $|g,1\rangle$ which finally is rotated to the spin state $|g,0\rangle$ forming a photon wave packet in the waveguide (here 0 and 1 denote the number of photons in the single cavity mode). The receiving mode is just the time-reversed process. Undesirable dynamics involving the state $|\bar{t}\rangle$ is eliminated by making the Zeeman splitting sufficiently larger than the cavity-dot coupling and the Rabi frequency. The resultant optical process is the cavity-assisted Raman process in a Λ-type three-level system as required by the prototype quantum interface (see Figure 33). Numerical calculations including the non-resonance transitions and realistic decoherence have been performed and high fidelity of desired operations at the quantum interface is demonstrated (see Section 7.4 for details).

7.2. *Control of spin-photon interface*

In the previous section, we have shown that the dot–cavity–waveguide coupled structure could be an efficient solid state realization of the prototype quantum interface. In order for such quantum interface to be suitable for a quantum network, proper control schemes are required.

The difficulty in realizing the network lies in the receiving end. Instead of being trapped at the quantum node, the single photon pulse can be reflected by the cavity unless the pulse shape of the classic control laser matches the single photon wavepacket exactly, known as quantum impedance matching [346,350]. One way to deal with this requirement was provided in [277]. The central idea is that if a laser pulse can be found for generation of an outgoing photon wavepacket with time reversal symmetry, by using this laser control at the sending node and its time reversal at the receiving node, the time reversal symmetry will guarantee the photon wavepacket to be completely trapped at the receiving node. A solution for such a laser control pulse was given in [277].

The time reversal symmetric control scheme requires the sending and receiving quantum nodes to be identical in terms of optical transition frequencies and strength of coupling between the components. Unfortunately, such requirement is practically impossible to fulfill in solid state systems since the fabricated QDs and microcavities naturally have shape variations and size fluctuations, leading to inhomogeneity in optical frequencies. The cavity field has a highly non-uniform profile and thus cavity-dot coupling differ from dot to dot. For realization of a quantum network with solid state structures, control schemes beyond the time symmetric one is required. In the sending function, it is straightforward to solve for the outgoing single photon wavepacket $\alpha(t)$ if we know the form of the laser control pulse $\Omega(t)$. The key problem is the inverse functional relation $\Omega(t)=\mathcal{F}^{-1}[\alpha(t)]$, i.e., given an arbitrary single photon wavepacket $\alpha(t)$, the exact laser pulse that can generate this single photon wavepacket at a sending node, or completely trap it at a receiving node. Knowing this relation allows the sending and receiving operations to be separately addressed and hence the construction of a quantum network with heterogeneous quantum nodes.

Solutions to $\Omega(t)=\mathcal{F}^{-1}[\alpha(t)]$ were first given in the adiabatic approximations [346,350]. Exact solutions in the non-adiabatic form were later found by Yao *et al.* [119,347], as briefly described below.

The Hamiltonian including the interaction between the single-mode cavity and the three-level system and the channel continuum is

$$H=\omega_c a^{\dagger}a+\omega_t|t\rangle\langle t|+\omega_e|e\rangle\langle e|+\int_0^{\infty}\mathrm{d}\omega\,\omega b_{\omega}^{\dagger}b_{\omega}+g_{\mathrm{cav}}\big(i|t\rangle\langle g|a+\mathrm{H.c.}\big)$$
$$+\frac{1}{2}\big[i\Omega(t)e^{-i\omega_L t}|t\rangle\langle e|+H.c.\big]+\int_0^{\infty}\mathrm{d}\omega\Big(i\sqrt{\gamma/2\pi}b_{\omega}^{\dagger}a+\mathrm{H.c.}\Big), \tag{27}$$

where b_ω is the annihilation operator for the mode of frequency ω in the channel continuum and a the annihilation operator for the cavity mode. The energy of state $|g\rangle$ is set as zero. The $|g\rangle\rightarrow|t\rangle$ transition is coupled to the cavity mode with strength g_{cav}. The $|e\rangle\rightarrow|t\rangle$ transition is coupled to the external control laser of time-dependent Rabi frequency $\Omega(t)$ and central frequency ω_L. The coupling of the cavity mode to the channel continuum is assumed constant:$\sqrt{\gamma/2\pi}$. An ideal situation is assumed neglecting photon leakage into free space through intermediate state $|t\rangle$ or the cavity sidewall.

We note that the system described by this Hamiltonian, under the laser excitation and the cavity-dot and cavity-channel interaction, has two invariant Hilbert subspaces, with the basis $\{|g,0\rangle\ |\mathrm{vac}\rangle\}$ and $\{|e,0\rangle\ |\mathrm{vac}\rangle,\ |t,0\rangle\ |\mathrm{vac}\rangle,\ |g,1\rangle\ |\mathrm{vac}\rangle,\ |g,0\rangle\ |\omega\rangle\}$ (where in $|s,n\rangle$, $s=g$, e or t denotes the state of the three-level system, n denotes the number of photons in the cavity mode, and $|\omega\rangle$ denotes the one-photon Fock state of the channel mode of frequency ω). So the evolution of the system can be generally described by the state $C_g|g,\ 0\rangle\ |\mathrm{vac}\rangle+C_e|\ \Psi^e(t)\rangle$ in the interaction picture, where

$$\big|\Psi^e(t)\big\rangle=\beta_e(t)|e,0\rangle|\mathrm{vac}\rangle+\beta_t(t)|t,0\rangle|\mathrm{vac}\rangle$$
$$+\beta_c(t)\big|\,g,1\big\rangle|\mathrm{vac}\rangle+\int_0^{\infty}\mathrm{d}\omega_{\omega}\alpha_{\omega}(t)\big|\,g,0\big\rangle|\omega\rangle. \tag{28}$$

The time evolution of the amplitudes in the interaction picture is described by the following Schrödinger equations,

$$\dot{\beta}_e=-\frac{\Omega^*}{2}e^{-i(\omega_t-\omega_L-\omega_e)t}\beta_t, \tag{29a}$$

$$\dot{\beta}_t=g_{\mathrm{cav}}e^{i(\omega_t-\omega_c)t}\beta_c+\frac{\Omega}{2}e^{i(\omega_t-\omega_L-\omega_e)t}\beta_e, \tag{29b}$$

$$\dot{\beta}_c=-g_{\mathrm{cav}}e^{-i(\omega_t-\omega_c)t}\beta_t-\sqrt{\gamma}\alpha_{\mathrm{in}}(t)-\frac{\gamma}{2}\beta_c \tag{29c}$$

$$=-g_{\mathrm{cav}}e^{-i(\omega_t-\omega_c)t}\beta_t-\sqrt{\gamma}\alpha_{\mathrm{out}}(t)+\frac{\gamma}{2}\beta_c, \tag{29d}$$

where $\alpha_{\mathrm{in}}(t)\equiv\int\mathrm{d}\omega\,\alpha_{\omega}(t_0)e^{-i(\omega-\omega_c)t}/\sqrt{2\pi}$ with $t_0\rightarrow-\infty$ and $\alpha_{\mathrm{out}}(t)\equiv\int\mathrm{d}\omega\,\alpha_{\omega}(t_1)e^{-i(\omega-\omega_c)t}/\sqrt{2\pi}$ with $t_1\rightarrow+\infty$ can be regarded as the incoming and outgoing wavepacket of the photon in the quantum channel, respectively. From Equations (29c) and (29d), we note that evolution of $\beta_c(t)$ is simply an

instantaneous map of the difference between the input and output field in the photonic channel

$$\sqrt{\gamma}\beta_c(t) = \alpha_{\text{out}}(t) - \alpha_{\text{in}}(t). \tag{30}$$

$\beta_t(t)$ is also readily expressed in terms of $\alpha_{\text{in}}(t)$ and $\alpha_{\text{out}}(t)$ as,

$$\begin{aligned}\beta_t &= \frac{-\dot{\beta}_c - \sqrt{\gamma}\alpha_{\text{in}}(t) - \frac{\gamma}{2}\beta_c}{g_{\text{cav}}} e^{i(\omega_t-\omega_c)t} \\ &= \frac{-(\dot{\alpha}_{\text{out}} - \dot{\alpha}_{\text{in}})/\sqrt{\gamma} - (\alpha_{\text{in}}(t) + \alpha_{\text{out}}(t))\sqrt{\gamma}/2}{g_{\text{cav}}} e^{i(\omega_t-\omega_c)t}.\end{aligned} \tag{31}$$

So as the amplitude of $\beta_e(t)$,

$$\frac{\mathrm{d}}{\mathrm{d}t}|\beta_e|^2 = -\frac{\mathrm{d}}{\mathrm{d}t}|\beta_t|^2 + g_{\text{cav}}\left[\beta_c^*\beta_t e^{-i(\omega_t-\omega_c)t} + \beta_c\beta_t^* e^{i(\omega_t-\omega_c)t}\right], \tag{32}$$

and the phase,

$$\begin{aligned}\frac{\mathrm{d}}{\mathrm{d}t}\arg(\beta_e) = &\frac{1}{2i}|\beta_e|^{-2}\left(\dot{\beta}_t\beta_t^* - \beta_t\dot{\beta}_t^*\right) \\ &+ \frac{g_{\text{cav}}}{2i}|\beta_e|^{-2}\left[\beta_t\beta_c^* e^{-i(\omega_t-\omega_c)t} - \beta_c\beta_t^* e^{i(\omega_t-\omega_c)t}\right].\end{aligned} \tag{33}$$

Finally, from Equation (29b), the complex Rabi frequency of the laser pulse $\Omega(t)$ can be expressed in terms of the amplitudes that have been solved above,

$$\Omega(t) = 2\frac{\dot{\beta}^t - g_{\text{cav}}\beta^c}{\beta^e}. \tag{34}$$

Thus the desired operation, with $\alpha_{\text{in}}(t)$ and $\alpha_{\text{out}}(t)$ arbitrarily specified, can be generated on demand as long as the normalization condition of the wavefunction is not violated

$$\frac{\mathrm{d}}{\mathrm{d}t}\left(|\beta_e|^2 + |\beta_t|^2 + |\beta_c|^2\right) = |\alpha_{\text{in}}(t)|^2 - |\alpha_{\text{out}}(t)|^2. \tag{35}$$

The functions of this quantum interface can be classified into three types:

(I) if there is no incoming photon, the quantum interface generates an outgoing photon wavepacket of a specified shape.

(II) if there is an incoming photon wavepacket of a specified shape, it is completely trapped by the quantum interface so that there is non outgoing field.

(III) if there is an incoming photon wavepacket of a specified shape, the quantum interface generates an outgoing photon wavepacket of another specified shape – a controlled scattering process.

The first two types of control form the basis for the quantum network operation. With control of the type III, the quantum interface can act as a controllable scatter or pulse shaper for single photon wavepackets. This control can also be considered as the combination of consecutive controls of types II and I. In the following section, we will discuss in more detail how to implement the first two types of controls for a quantum network.

7.3. *Inter-node operations in a quantum network*

The sending node of a quantum network is operated with control of type I. The initial conditions are: $\alpha_{\text{in}}(t)=0$, $\beta_c(t_0)=0$, $\beta_e(t_0)=1$ and $\beta_t(t_0)=0$. The integral form of Equation (35) becomes

$$|\beta_e|^2 = 1-\sin^2\theta\int_{t_0}^{t}|\tilde{\alpha}_{\text{out}}(\tau)|^2\mathrm{d}\tau-|\beta_c|^2-|g_{\text{cav}}|^{-2}|\dot{\beta}_c+\gamma\beta_c/2|^2, \tag{36}$$

where $\tilde{\alpha}_{\text{out}}$ is the normalized wavepacket of the emitted photon, and $\sin^2\theta$ is the average photon number. For a photon number and a pulse shape arbitrarily specified, the amplitude of the cavity mode is determined by Equation (30) as $\beta_c(t)=\sqrt{\gamma}\tilde{\alpha}_{\text{out}}(t)\sin\theta$. If we pose the problem of finding the laser control pulse to produce a specified shape of the outgoing photon wavepacket, the fact that the right-hand side of Equation (36) is positive requires the specified output pulse be sufficiently smooth, i.e. the pulse generation process be slower than the cavity-channel tunnelling and the dot–cavity coupling rate (with timescales γ^{-1} and g_{cav}^{-1}, respectively). At the remote future time, $t_1\to+\infty$, the photon emission process is completed, i.e. $\beta_c(t_1)=\dot{\beta}_c(t_1)=0$, so $\beta_e(t_1)=e^{i\phi}\cos\theta$ with the controllable phase ϕ given by Equation (33). The general form of the photon generation process can be expressed as

$$\begin{aligned}&\big(C_g|\,g\rangle+C_e|e\rangle\big)\otimes|\text{vac}\rangle\\ &\xrightarrow{\Omega(t)}C_g|\,g\rangle\otimes|\text{vac}\rangle+C_e\big[e^{i\phi}\cos\theta|e\rangle\otimes|\text{vac}\rangle+\sin\theta|\,g\rangle\otimes|\tilde{\alpha}_{\text{out}}\rangle\big].\end{aligned} \tag{37}$$

A full Raman process corresponds to $\theta=\pi/2$ and $\beta_e(t_1)=0$, where Equation (37) is reduced to,

$$\big(C_g|\,g\rangle+C_e|e\rangle\big)\otimes|\text{vac}\rangle\xrightarrow{\Omega(t)}|\,g\rangle\otimes\big(C_g|\text{vac}\rangle+C_e|\tilde{\alpha}_{\text{out}}\rangle\big), \tag{38}$$

which results in the mapping of the stationary qubit onto the flying qubit. If initially the three level system is entirely in state $|e\rangle$, this mapping operation can function as a deterministic generation of a single-photon wavepacket with any desired shape $\tilde{\alpha}_{\text{out}}(t)$. If the Raman cycle is controlled to be partially completed ($\theta<\pi/2$), the state initially in $|e\rangle\otimes|\text{vac}\rangle$ is transformed into an entangled state of the stationary spin and the flying photon

$$|e\rangle\otimes|\text{vac}\rangle\xrightarrow{\Omega(t)}e^{i\phi}\cos\theta|e\rangle\otimes|\text{vac}\rangle+\sin\theta|\,g\rangle\otimes|\tilde{\alpha}_{\text{out}}\rangle. \tag{39}$$

The entanglement entropy $E=-\cos^2\theta\log_2\cos^2\theta-\sin^2\theta\log_2\sin^2\theta$ can be set at any value between 0 and 1 depending on the rotating angle θ.

The receiving node is operated with control of type II, typically as a full Raman cycle, in the quantum network scheme. With the three level system initially on state $|g\rangle$ and the incoming photon $C_g|\text{vac}\rangle+C_e|\alpha_{\text{in}}(t)\rangle$, the mapping transformation is,

$$|\,g\rangle\otimes(C_g|\text{vac}\rangle+C_e|\alpha_{\text{in}}\rangle)\xrightarrow{\Omega(t)}(C_g|\,g\rangle+C_e|e\rangle)\otimes|\text{vac}\rangle. \tag{40}$$

As in the sending process, the incoming photon pulse $\alpha_{\text{in}}(t)$ can be arbitrarily specified, provided that it is smooth enough.

By combining the sending and receiving processes, the transfer of a qubit from one node to another can be easily implemented, with the outgoing photon from the sending node directed as the incoming photon for the receiving node. As the photonic channel is linear, two state-transfer operations with opposite directions can be performed in parallel, and qubits at the two nodes will be swapped. Swap operations can only be performed between nodes separated with sufficiently large distance so that photon travelling time in the channel is longer than the interface operation time.

If the operation at the sending node has been designed to produce an entangled state of the stationary and the flying qubit, the mapping process at the receiving node will just produce an entangled state of the two nodes by the transformation,

$$\begin{aligned} |e\rangle_1|g\rangle_2 \otimes |\text{vac}\rangle &\xrightarrow{\Omega_1(t)} e^{i\phi}\cos\theta|e\rangle_1|g\rangle_2 \otimes |\text{vac}\rangle + \sin\theta|g\rangle_1|g\rangle_2 \otimes |\tilde{\alpha}_{\text{out}}\rangle \\ &\xrightarrow{\Omega_2(t)} \left[e^{i\phi}\cos\theta|e\rangle_1|g\rangle_2 + \sin\theta|g\rangle_1|e\rangle_2\right] \otimes |\text{vac}\rangle. \end{aligned} \tag{41}$$

Non-local entanglement can thus be generated deterministically in the quantum network.

With the exact solutions for the interface dynamics, the sending and receiving functions can be separately addressed. This enables the construction of a quantum network with heterogeneous quantum nodes, which is essential for solid state realization. To illustrate this, we give below an exemplary control strategy. The control laser pulse at a sending node can have a general shape $\Omega_1(t)e^{-i\omega_L^1 t}$ with the pulse area satisfying the specified rotation angle θ. The outgoing single photon wavepacket has a definite shape $\alpha_{\text{out}}^1(t)$ (in the rotating frame defined by frequency ω_c^1), determined by the laser control $\Omega_1(t)$ and the parameters of the sending node g_{cav}^1, γ_1 and Raman detuning $\Delta_1 \equiv \omega_t^1 - \omega_L^1 - \omega_e^1 = \omega_t^1 - \omega_c^1$. Then we pose the problem of finding the optical control $\Omega_2(t)e^{-i\omega_L^2 t}$ to trap the single photon wavepacket $\alpha_{\text{in}}^2(t) \equiv \alpha_{\text{out}}^1(t)e^{i(\omega_c^2-\omega_c^1)t}$ at the receiving node which may have a different set of parameters g_{cav}^2, γ_2, ω_t^2, ω_e^2 and ω_c^2. From Equation (36) and the discussion follows, it implies that the tolerance of the node inhomogeneity is determined by the node bandwidth, i.e. the dot–cavity coupling g_{cav} and dot-waveguide tunnelling γ. Thus, a large dot–cavity coupling g_{cav} is essential. This tolerance was discussed more explicitly by Fattal *et al.* in Ref. [348].

7.4. *Operations with imperfections*

In this section, we discuss the effects of various imperfections that may occur in a realistic quantum network and the corresponding mitigation.

7.4.1. *Intrinsic photon leakage into free space*

The desired quantum evolution is through the pathway of trion–cavity photon–waveguide photon. The main causes of photon leakage out of this quantum pathway is through the trion decay by spontaneous emission and the cavity mode leakage other than the tunnelling into the waveguide. The waveguide and fibre loss is

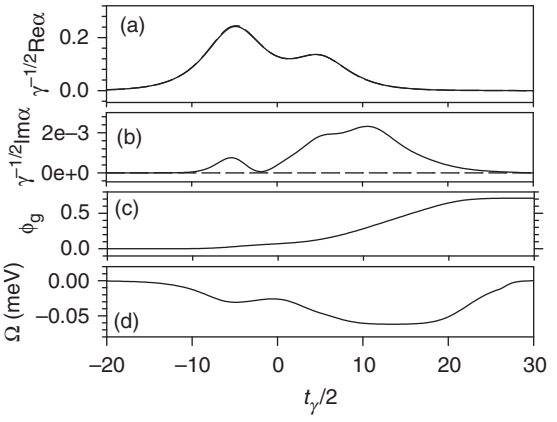

Figure 35. Generation of a single photon wavepacket with an asymmetric double sech shape (see text). (a) Real part of the dimensionless amplitude of the simulated single photon wavepacket (——) as a function of the dimensionless time $\gamma t/2$. The deviation from the target shape (– – –) is not visible. (b) Imaginary part of the simulated single photon wavepacket (——) and that of the target one (– – –). (c) Phase drift of the component $|g, 0\rangle$. (d) Rabi frequency of the control laser pulse. (Adapted from W. Yao *et al.*, Physical Review Letters, 95 (2005) p. 030504 [119]. Copyright © 2005 by the American Physical Society.).

negligible on the distance-scale of relevance for intra-chip communication and for inter-chip communications if the chips are distributed in a spatial range of $\lesssim$10 cm. As long as the photon leakage rate is much smaller than the bandwidth of the desired quantum pathway (determined by the dot–cavity coupling $g_{\rm cav}$ and the cavity-waveguide tunnelling γ), high fidelity operations can be expected. Typical trion decay rates in self-assembled QDs are $\Gamma \sim \mu$eV [229,230], and the intrinsic loss rate of a high-Q cavity (i.e. excluding coupling to the dot and the waveguide) can be potentially achieved at $\gamma_0 \gtrsim 0.1\,\mu$eV (corresponding to a Q-factor $\sim 10^7$) [282,283]. The state-of-the-art dot–cavity coupling constant achieved is $g_{\rm cav} = 0.1$ meV [279,284,286], while the cavity-waveguide tunnelling rate is controlled in design by the gap distance. Thus the bandwidth can be two orders larger than the leakage rate.

The simulation result of mapping a spin state to a flying photon wavepacket with the shape targeted as an asymmetric superposition of two sech-functions as $\alpha_{\rm out}^{\rm ideal}(t) = {\rm sech}(\gamma t/6 + 5) + 0.5\,{\rm sech}(\gamma t/6 - 5)$ is shown in Figure 35. The trion decay rate, based on experiment [229], is set at $\Gamma = 3\,\mu$eV, and the intrinsic cavity loss rate is assumed to be $\gamma_0 = 0.1\,\mu$eV [283]. The cavity-fibre tunnelling rate is chosen to be $\gamma = 0.2$ meV and the dot–cavity coupling constant $g_{\rm cav} = 0.1$ meV [284]. The fidelity of the single photon generation $|\langle\alpha_{\rm out}^{\rm ideal}|\alpha_{\rm out}\rangle| \approx 0.9912$. Because of the non-adiabatic optical pumping and dot–cavity coupling, the whole mapping process can be completed within 300 ps. The simulation of the photon absorption process shows an overall fidelity greater than 0.99 as well. With the above chosen parameters, the cavity mode broadening due to the coupling to waveguide is actually larger than the dot–cavity coupling. The system is therefore *not* in the strong coupling regime by the usual definition [279,284,286]. High fidelity is nonetheless guaranteed by the large Purcell factor.

Table 1. Effect of errors in coupling parameters on the fidelity of entanglement and of state transfer.

	No error	10% g Error	10% γ Error	10% $\Omega(t)$ Error
Entanglement	0.9912	0.9872	0.9894	0.9862
Transfer	0.9901	0.9870	0.9891	0.9879

7.4.2. *Unwanted coupling to energy levels beyond the 3-level Λ system*

In the energy level structure of the dot–cavity coupled system, non-resonance coupling to other energy levels could lead to excitation out of the 3-level Λ subspace and AC Stark shift of the qubit states of interest (Figure 34c). These effects have been included in the numerical simulation given in Figure 35. As shown in Figure 35(c), AC Stark shift induces a deterministic phase drift between $|g\rangle$ and $|e\rangle$. As the two excitation pathways starting respectively from $|g\rangle$ and $|e\rangle$ are independent of each other (Figure 34c), this phase drift is independent of the coefficients C_g and C_e. Therefore, it can be compensated by a single-qubit operation irrespective of the quantum state being mapped. Leakage out of the qubit subspace by the non-resonance excitation to multi-photon states can be greatly suppressed if the Zeeman splitting is much larger than the Rabi frequency and the cavity-dot coupling. For InAs self-assembled QDs, Zeeman splitting ~meV can be achieved in a moderately strong magnetic field (~10 T) due to the large g-factor of InAs materials.

7.4.3. *Unknown parameter offsets*

Solutions to the laser pulses for desired controls of the quantum interface are based on the knowledge of the coupling strength g_{cav}, γ and $\Omega(t)$. But in practice, there could be various unknown errors on parameters due to imperfect characterization of the system. The robustness of the control schemes in the presence of unknown system parameter errors is thus a critical feature. In Table 1, we list the effects of unknown offsets from the assumed values of various parameters on the fidelity of two typical quantum network operations: (i) entangling two quantum nodes into state $e^{i\phi}|g\rangle_1|e\rangle_2 + |e\rangle_1|g\rangle_2$; (ii) transfer of the state $|g\rangle + |e\rangle$ between two nodes. In both cases, the target shape of the involved single photon wavepacket is $\text{sech}(\frac{\gamma t}{6})$ and the design of the control laser pulses uses the assumed parameter values. The system shows a surprising robustness: 10% unknown errors on g_{cav}, γ or $|\Omega(t)|$ only reduce the fidelity by less than 1%. This intrinsic robustness against unknown parameter errors paves the way for learning studies of the system parameters by trial and error [320,322,351], and classical feedback controls in the quantum network [352,353].

7.4.4. *Laser intensity fluctuations*

The $|\Omega(t)|$ error studied in Table 1 is a global one on the amplitude, e.g. induced by the QD being slightly out of focus from the laser control field or an unknown offset from the assumed value of the dot dipole moment. The actual control laser pulse may have shape deviations from the desired ones, e.g. due to temporal fluctuations

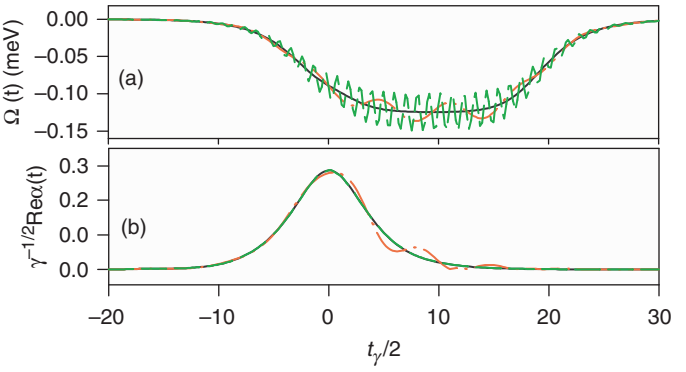

Figure 36. Transfer of state $|g\rangle + |e\rangle$ between two nodes in presence of amplitude fluctuations of the control lasers. (a) The desired control laser pulse by design at the sending node (——) and the actually applied control pulse with slow fluctuations (– · – · –) and fast fluctuations (——). The control laser pulse at the receiving node has a similar error applied. (b) The generated intermediate single photon wavepacket. The solid curve shows the target shape of the single photon if the ideal control laser pulse is used (solid curve in (a)). Deviation of the generated single photon wavepacket is invisible in the case of fast laser fluctuations. The fidelity of the transfer is 0.9912 with slow fluctuations and 0.9922 with fast fluctuations. The parameters used are: $\gamma = 0.2\,\text{meV}$, $g_{\text{cav}} = \gamma/2$, $\gamma_t = 3\,\mu\text{eV}$ and intrinsic cavity leakage 0.05 μeV. (Adapted from W. Yao *et al.*, Physical Review Letters, 95 (2005) p. 030504 [119]. Copyright © 2005 by the American Physical Society.).

in laser amplitude. The effects of this error source have been studied in [347], where the control scheme is found to be immune against fast fluctuations (Figure 36). This robustness is due to the finite bandwidth of the quantum interface determined by the cavity-dot coupling strength and the cavity-waveguide tunnelling rate. Any temporal fluctuations in the control field with the frequency higher than the interface bandwidth are effectively averaged out. The time independent amplitude error listed in Table 1 may also be considered as a special shape error which is actually the worst scenario for the fidelity.

7.4.5. *Laser phase fluctuations*

The complex Rabi frequency $\Omega(t)$ can also have phase uncertainties due to laser phase drift which is typically slower than the timescale of interface operation. Assume that the laser control field at the moment of sending operation has an unknown phase of φ_1 and, hence, the Rabi frequency is $\Omega_1(t)\, e^{i\varphi_1}$. From the form of the coupling term that involves the laser field in the Hamiltonian Equation (27), the unknown phase factor can be absorbed by redefining the state $|\tilde{e}\rangle_1 \equiv e^{-i\varphi_1}|e\rangle_1$, so that,

$$\frac{1}{2}\left[i\Omega_1(t)e^{i\varphi_1}e^{-i\omega_L t}|t\rangle_{11}\langle e| + H.c.\right] \equiv \frac{1}{2}\left[i\Omega_1(t)e^{-i\omega_L t}|t\rangle_{11}\langle\tilde{e}| + H.c.\right] \tag{42}$$

and we can make the same transform at the receiving node where the control laser has the unknown phase φ_2 at the moment the single photon arrives. Starting from a general state $\left(C_g|g\rangle_1 + C_e|e\rangle_1\right)|g\rangle_2 \otimes |\text{vac}\rangle \equiv C_g|g\rangle_1|g\rangle_2 \otimes |\text{vac}\rangle + C_e e^{i\varphi_1}|\tilde{e}\rangle_1$

$|g\rangle_2 \otimes |\text{vac}\rangle$, two-node operations in the presence of laser phase uncertainties can be generally expressed as

$$\begin{aligned} & C_g|g\rangle_1|g\rangle_2 \otimes |\text{vac}\rangle + C_e e^{i\varphi_1}|\tilde{e}\rangle_1|g\rangle_2 \otimes |\text{vac}\rangle \\ \xrightarrow{\Omega_1(t)} & C_g|g\rangle_1|g\rangle_2 \otimes |\text{vac}\rangle \\ & \quad + C_e e^{i\varphi_1}\left[e^{i\phi}\cos\theta|\tilde{e}\rangle_1|g\rangle_2 \otimes |\text{vac}\rangle + \sin\theta|g\rangle_1|g\rangle_2 \otimes |\tilde{\alpha}_{\text{out}}\rangle\right] \\ \xrightarrow{\Omega_2(t-\tau)} & \left[C_g|g\rangle_1|g\rangle_2 + C_e e^{i\varphi_1}\left(e^{i\phi}\cos\theta|\tilde{e}\rangle_1|g\rangle_2 + \sin\theta|g\rangle_1|\tilde{e}\rangle_2\right)\right] \otimes |\text{vac}\rangle. \end{aligned} \tag{43}$$

The final state is equivalent to $[C_g|g\rangle_1|g\rangle_2 + C_e(e^{i\phi}\cos\theta|e\rangle_1|g\rangle_2 + e^{i\varphi_1}e^{-i\varphi_2}\sin\theta|g\rangle_1|e\rangle_2)] \otimes |\text{vac}\rangle$. If the control laser fields at the two nodes is phase locked so that there is a certain relative phase between $\Omega_1(t)$ and $\Omega_2(t-\tau)$, the two-node operation is well-protected from laser phase fluctuations.

7.4.6. *Deterministic phase and shape variations in photon propagation*

Unknown offsets from the assumed waveguide/fibre dispersion relation or nonlinearity of the dispersion relation can cause phase and shape variations of the single photon wavepacket during the propagation. At low temperature where thermal fluctuations are suppressed, such variations are deterministic and can thus be incorporated in the design of the receiving node control. Closed-loop adaptive feedback control [352,353] or quantum learning algorithms [320,322,351] can be implemented to pre-characterize such variations.

7.4.7. *Loss and indeterministic fluctuation in photon propagation*

For inter-node operations between well-separated nodes (distance $\gtrsim$ m), photon losses and indeterministic fluctuations during the propagation in the fibre could be non-negligible. Error correction schemes dealing with such propagation loss has been proposed using auxiliary stationary qubits in the quantum node [354]. The idea of quantum repeaters with nested purification schemes [355] might also be incorporated into the quantum network design for protection against the photon propagation loss and indeterministic fluctuations.

7.5. *Summary: coherent quantum manipulation by remote control*

In this section, we discuss how to unite clusters of QD spins into a network for distributed quantum information processing. The advances in the fabrication of coupled structures of QDs, semiconductor microcavities and optical waveguides make possible a high efficiency quantum interface between stationary spin qubits and flying photon qubits, where the latter can be used for communication between seperated clusters. As indicated in the DiVincenzo criteria [2], such capability greatly enhances the chance towards the construction of fault-tolerant scalable quantum computers in these systems.

Counterintuitively, real excitations of the continuum modes in the quantum channel act as a conduit for mediating coherent operations rather than the cause of dissipation. A more abstract picture for the network structure here is the 3-level Λ

system coupled to a one-dimensional continuum modes, formed by the cavity-waveguide coupled structure, considered as a whole electromagnetic continuum. The important function of the cavity is in providing a local resonance in spectrum with large spectral weight near the frequency of the QD optical transition, which results in a large Purcell factor (i.e. the ratio between the spectral weight of the cavity-waveguide modes and the free-space modes). The unitary evolution dominates over the irreversible processes within the coupled system of the QD and the cavity-waveguide continuum. Temporal shaping of the laser control pulse provides sufficient freedom to control such evolution. While the relevant part of the spectrum of the cavity-waveguide continuum is of a simple Lorentz shape with width $\gamma \ll \omega_c$, this Markovian condition is not a mandatory requirement. Provided that the 3-level Λ system is coupled to a continuum where a spectral weight peak (irrespective of shape) results in a high Purcell factor at the relevant optical frequency, control schemes for high efficiency network operation is possible [356]. This opens up possibilities for networking localized stationary qubit by continuum modes without cavity QED and in the non-Markovian regime.

8. Challenges

We have discussed all the necessary elements for implementing scalable quantum computation with electron spins in QDs under optical control. To reach the larger goals, there remain many obstacles. Here we present an overview of what technologies may be at the top of the required list to accomplish the goals. To have a concrete idea of the challenges for short- to mid-term pursuit, we will also give an estimate of the resources for a benchmark task: factorization of 15 with Shor's algorithm.

8.1. *Resource estimate for Shor's algorithm for factorizing 15*

Undoubtedly, Shor's algorithm for factorizing integers is the most important example demonstrating the superpower of quantum computation [1,172]. It gives a solution with time consumption only polynomially increasing with the problem size (the bit length of the number to be factorized) and thus offers an exponential speedup over all known classical counterparts. Historically, Shor's algorithm has stimulated the exploding enthusiasm in quantum computation by showing its computation power. An efficient factorization scheme can be used to break the public-key encryptions, such as the RSA protocol which is widely used in internet communication. The factorization of the first 'non-trivial' number – 15 by Shor's algorithm has been realized with the liquid NMR spectroscopy [3], which serves as a benchmark for quantum computation in other systems. Here we give an estimate of the resources required to accomplish such a milestone in the optically controlled spin-based QD system.

The key step of Shor's algorithm for factorizing a number N is to find the smallest nonzero r satisfying $a^r = 1 \bmod(N)$ (i.e. the order of a with respect to N), where the seed a is co-prime to N (i.e. the maximum common factor of a and N, denoted as (a, N) is 1) and can be randomly selected. By the fact that the order r is

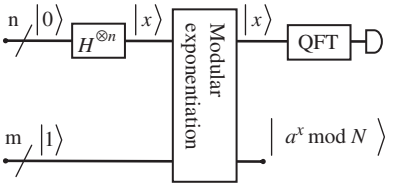

Figure 37. Logic flow-chart of Shor's algorithm for order searching.

the period of the modular exponentiation function $f(x) = a^x \bmod(N)$, it suffices to search for the period or to measure the frequency of the function $f(x)$, which can be accomplished by the quantum Fourier transformation (QFT). The process of finding the period can be expressed as [1,172]

$$|0^n\rangle \otimes |0^m\rangle \xrightarrow{\text{QFT}^{-1}} \sum_{x=0}^{2^n-1} |x\rangle \otimes |0^m\rangle \xrightarrow{f(x)} \sum_{x=0}^{2^n-1} |x\rangle \otimes |a^x \bmod(N)\rangle$$
$$\xrightarrow{\text{QFT}} \sum_{y=0}^{2^n-1} \sum_{x=0}^{2^n-1} e^{i2\pi xy/2^n} |y\rangle \otimes |a^x \bmod(N)\rangle, \tag{44}$$

where $|0^{n(m)}\rangle$ denotes a $n(m)$-qubit register set at the zero state, $m = [\log_2 N] + 1$ the bit length of N, x a binary number and the normalization constants for the states have been omitted. Both the QFT and the modular exponentiation can be carried out with the number of elementary quantum gates polynomially increasing with the problem size (m). A more detailed review of the order-finding algorithm is given in Appendix C.1.

As $f(x)$ is a periodic function with period r, the population of the basis state of the first register at the end of the program will be non-zero only for $y \approx 2^n\, c/r$ ($c = 0$, $1, \ldots, r-1$), for the QFT will transform a period function into sharp peaks at the multiples of the frequency $2^n/r$. Thus, a quantum measurement of the first register in the computational basis will result one of states in the superposition, thus yielding the number $2^n\, c/r$ from which the order r can be derived and the number N factorized. The order r generally is of the order of magnitude of $N \sim 2^m$, so the number of basis states in the superposition is $\sim 2^m$, an exponential function of the problem size, which explains why a QND measurement is required to make Shor's algorithm scalable for factorizing large numbers, as discussed in Section 6.

The flow-chart of Shor's algorithm for order finding is shown in Figure 37. The first QFT subroutine can be simplified to a series of single-qubit Hadamard gates (see Appendix C.1 for the definition of the elementary quantum gates) since the initial state is set to be $|0^n\rangle$. The second register is initialized to be $|1\rangle$ to facilitate the modular exponentiation. In principle, the length of the first register n should be large enough to reproduce the real number $1/r$ with sufficient effective bits. To factorize 15, it turns out that the orders of all co-primes of 15 are either 2 (for $a = 4, 11, 14$) or 4 (for $a = 2, 7, 8, 13$), both of which are a factor of 2^3, so three-qubit register should be enough to resolve $2^n/r$. Including the second register, seven qubits are sufficient to demonstrate the algorithm for the first 'non-trivial' target: 15.

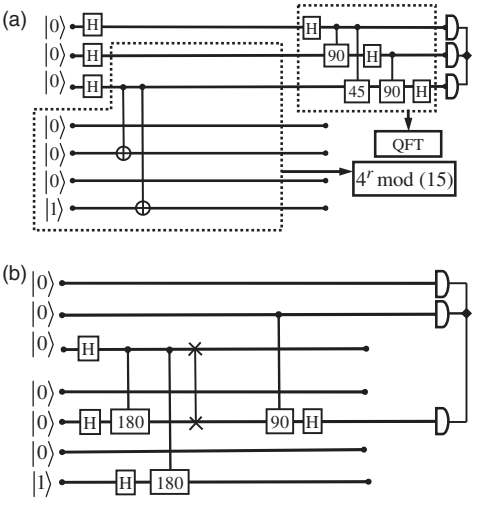

Figure 38. (a) Quantum circuit for searching r for $4^r = 1$ mod(15), where the subprograms for the modular exponentiation and the QFT are blocked together as indicated. (b) The simplified circuit with only local two-qubit gates.

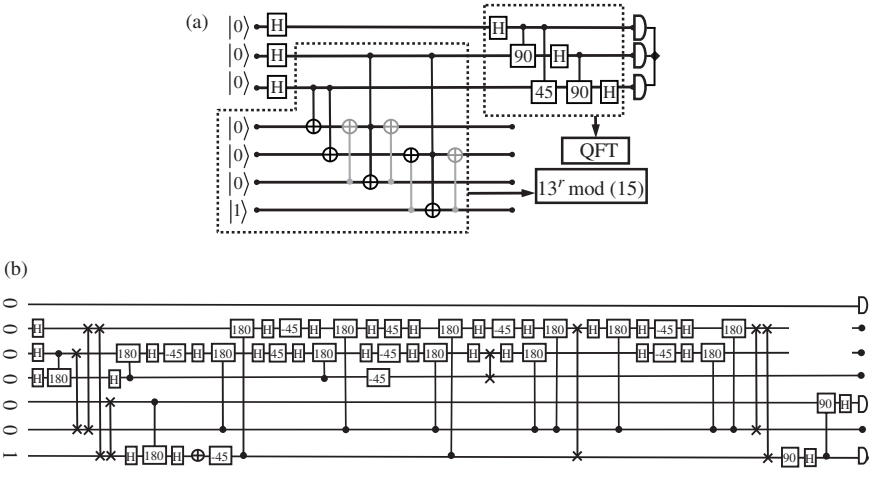

Figure 39. (a) Quantum circuit for searching r for $13^r = 1$ mod(15). The faded components can be removed without changing the computing result. (b) The simplified circuit with all gates experimentally realizable.

Figures 38 and 39 give the specific quantum circuits constructed with the elementary quantum gates (as defined in Appendix D) to implement Shor's algorithm for factorizing 15 with the seed number selected as $a = 4$ (an easy example) and $a = 13$ (a difficult example). Compilation and optimization have been performed to reduce the number of physical operations:

(1) to minimize the number of SWAP gates for coupling remote qubits in the linear configuration, the labelling of the qubits in the register has been

optimized, and at the end of the program the qubits are not swapped back to their original positions but re-labelled instead, as indicated in Figure 16(a).
(2) the quantum gates are omitted if they act on the second register after the last gate controlled by the first register, since such gates have no effect on the QFT of the first register.
(3) whenever possible, the sequential single-bit operations on the same qubit are combined into one single-qubit gate (in experiment, all one-bit gates between two controlled gates can be realized by a single-spin rotation).

The numbers of gates and pulses and the running time needed in different cases are estimated with the following considerations:

(1) all sequential single-qubit gates on the same qubit are combined as one single-spin rotation which can be completed with three pulses within 10 ps.
(2) each SWAP gate can be completed by two pulses within 10 ps.
(3) each controlled phase gate can be completed by three pulses in 10 ps.
(4) each qubit can be initialized by three pulses within 120 ps.
(5) to reduce the complexity of pulse designing, all operations within the local module should be performed serially (to factorize larger numbers, a large-scale quantum network of distributed modules will be needed and in that case operations could be performed in parallel in separated modules).
(6) the time consumption for quantum measurement is not counted.

The timescales of the single- and two-qubit gates are chosen in accordance with the discussions in Section 4. While there are so far no experimental demonstrations of optically controlled two-qubit gates, the estimated timescales of the single-qubit gates are similar to the experimentally realized gates [78,79,181,182]. The estimated resource requirements are summarized in Table 2. Alternatively, the controlled phase gates can be replaced by the $\sqrt{\text{SWAP}}$ gates, and the resource requirement is expected to be similar.

8.2. *Technologies most needed*

8.2.1. *Complex multi-pulse optics*

As listed in Table 2, to factorize the small number 15, the number of optical pulses needed is in the order of 100. It is would be extremely difficult to synchronize so many laser pulses and to stabilize the relative phases, but all the pulses may be viewed as a single one with complex frequency and phase design. The complex pulse may be formed from a single laser source by pulse shaping techniques, such as

Table 2. The numbers of gates and pulses and the time required to factorize 15 by Shor's quantum algorithm with two typical examples of seed numbers a for $a^r = 1 \bmod(15)$.

a	# 1-Bit gates	# SWAP	# Phase gate	# Pulses	Time-cost
$a=4$	4	1	3	44	0.9 ns
$a=13$	20	8	15	142	1.3 ns

acousto-optical modulation [357,358]. Design of such a complex pulse is also very challenging. Learning or genetic algorithms may be developed to deal with the problem, with lessons learned from controlling complex chemical processes by ultrafast optical pulses [320–322]. The measurement involves many probe pulses interacting with many QDs. The signals are to be analyzed through frequency multiplexer as well as phase modulation with heterodyne detection [331]. Thus multi-dimensional spectroscopies [359–362] are desirable for characterizing the systems and for implementing a small-scale benchmark demonstration. Eventually, the measurement would have to be done with an efficient quantum channel like a cavity-waveguide structure.

8.2.2. *System fabrication and characterization*

The design of the quantum computer and its operation follow the sequence: the physical system is constructed first, with certain uncontrollability, then it is characterized. The optical control will be designed according to the system parameters. In such a procedure, we do not require an ultimate control of the system fabrication (hardware) but defer the difficult work to the control design (software) stage. For example, we do not require, and actually do not desire that all the QDs are almost identical. But of course, the system should be fabricated fulfilling certain conditions. Basically, we need a system made of QD clusters, which should meet the following requirements:

(1) QDs are only locally coupled. For a system with coupling between remotely separated dots, the design of the controlling pulses would require overhead increasing exponentially with the number of qubits, since essentially the control design amounts to solving the Schödinger equation of the whole system.
(2) the coupling between different QDs in a local node should be weak. Otherwise, tunnelling between different dots would make the local node rather a large QD molecule instead of a cluster of individual dots, making even a single-qubit gate as complex as a control of all the qubits in the local node.
(3) even though we do not require all the QDs to be nearly identical, the size of different QDs in a cluster should be in a relatively small range. Otherwise, the optical control, especially the energy shift by the AC Stark effect, would be extremely difficult.
(4) the number of active electrons in each QD should be controlled to be one, either by doping or by gate voltage control.

Once a QD system has been constructed, the characterization is not any less demanding. The parameters to be determined include electron doping level, electron spin g-factors, frequencies of the ground and excited state transitions, selection rules or relative dipole matrix elements for different transitions, tunnelling rates and exchange interaction of electrons in different levels and different dots, etc. Identification of the exciton, bi-exciton or trion transitions in two-dot systems have already been demonstrated in two vertically coupled dots with the help of varying the gate voltage [195]. A pair of laterally coupled dots remains a challenge.

The characterization of a cluster of, for example, seven QDs, is a tremendously difficult target for the current experiment capability. In the long run, we would expect no full characterization of the system be required. The solution may lie in, again, the learning algorithm, by which, the controlling optical pulses are to be designed, self-adaptive to the fidelity of a certain set of quantum gates.

8.2.3. *Nano-photonics*

The requirement of nano-optics is two-folded: First, the control of a local node requires near-field optical addressing. Second, the ultrafast fast initialization and QND measurement of a qubit, and coupling between different nodes need cavities and waveguides fabricated *in situ* with the QDs.

To address individually each cluster of QDs, a microlens and microfibre may be used. Each QD within a cluster is distinguished by its fingerprint transition frequencies. The spatial resolution required is given by the distances between clusters instead of the size of the clusters. Using high-index material for the microlens, spatial resolution $\sim 0.1\,\mu m$ may be achievable. In cases where the spatial resolution is not enough to single out dot clusters, an alternative solution would be further pulse shaping (probably with a learning algorithm as well) to eliminate the coupling between different clusters covered by one microlens.

To connect QDs with cavities and waveguides, two structures look promising. One is obtained by etching the surface where the QDs are grown [278]. Electron-beam lithography and chemical etching (sometimes plus some annealing) have already produced high-quality microcavities and waveguides on semiconductor surfaces. Even strong coupling between a QD and microcavity in such a system has been demonstrated [279]. Photonic crystals are another promising possibility. Point defects in photonic crystals can be made into nano-cavities with Q-factor $\gtrsim 10^6$ and effective volume less than a half-wavelength cubed [282,283]. Strong coupling between a QD and a photonic crystal nano-cavity has also been demonstrated [284,285]. QED of single QDs in nano-cavity in photonic crystals can be engineered [281,304,305]. Waveguides in photonic crystals can be made by line defects which may be coupled to remote nodes by optical fibres [301]. How to combine these photonic structures with the QD clusters, especially, how to assemble them in proper layouts and positions, would demand a great deal of progress in sample processing technologies.

We would like to point out that the photonic structure fabricated on the QD system may also be used to individually address each local node. Thus, we eventually may need no microlens or microfibres to attach each dot cluster.

A wilder conjecture is that the lasers be integrated in the photonic structure. Micro- or nano-lasers made of photonic crystal cavities have actually come into being. The remaining problem would be to make the laser emit into a waveguide, and to tailor it into wanted shapes and sequences. How is one to control the laser on-chip then? Electrical gates may be used. So we come around a full circle and find a point where different quantum computation strategies may be synthesized to achieve a common goal.

9. Conclusion

We have discussed various aspects of a scalable scheme of quantum computation based on optical control of electron spins in semiconductor QDs. To implement such a scheme, a number of outstanding challenges remain to be overcome.

We would like to add some remarks on two different philosophies in implementing digital computing or more generally automatic reasoning, which may give us some inspiration in the journey to realize quantum computation. One is related to the von Neumann structure of computers and the other is related to the Turing ACE structure, both of which are based on Turing's insightful view of programs and data as essentially the same for a universal computer. Turing's design is deeply rooted on his finding of universal computers and thus has a hardware of minimal instructions with complex functions to be implemented by software programming. The von Neumann structure, while keeping the important role of programming, tries to maximize the usage of hardware design to implement a large number of mathematical functions which would otherwise be solved simply by programming. We follow Turing's perception in describing the blueprint of a quantum computer based on semiconductor QDs and optical control of spins in them, simply for one reason: In implementing quantum computation, the hardware part is far more formidable than the design of optimal control. Thus we propose no need of perfectly controlled arrays of almost identical QDs but a control scheme programmed after a physical structure has been constructed and characterized. The randomness in the system synthesis is not to be eliminated but to be utilized. The requirement for a functional physical block is relatively simple: sufficient coupling for a universal set of quantum gates to be programmed. Finally, we note that Turing's philosophy is becoming more and more important nowadays in large-scale classical computers which tend towards the reduced instruction set computer (RISC) architecture.

When will a quantum computer come into being of practical usage? We do not know. But a hint may lie in the comparison between our present situation and the situation some 60 years ago when engineers were working hard to maintain thousands of vacuum tubes functioning together for a while before one or another went wrong. Scaling up of a quantum computer may not be as rapid as classical computers have done, but just be aware that adding one functioning qubit supposedly doubles the power of a quantum computer, which is worth 18 hard-working months in the sense defined by Moore's law.

Acknowledgements

This review is based on work done in long collaborations with many people, including D.G. Steel, D. Gammon, P. Chen, C. Peirmarocchi, S.E. Economou, S.K. Saikin, C. Emary, W. Yang and under financial support from US NSF (PHY 0804114), US ARO (W911NF-08-1-0487), and Hong Kong RGC (CUHK/402207 and HKU/706309P).

References

[1] P.W. Shor, *Algorithms for quantum computation: discrete logaorithms and factoring,* in *Proceedings of the 35th Annual Symposium on Foundations of Computer Sciences* E.S. Goldwasser ed., November, IEEE Press, Los Alamitos, CA, 1994, pp. 124.

[2] D. DiVincenzo, Fortschr. Phys. 48 (2000), p. 771.
[3] L.M.K. Vandersypen, M. Steffen, G. Breyta, C.S. Yannoni, M.H. Sherwood, and I.L. Chuang, Nature 414 (2001), p. 883.
[4] N.A. Gershenfeld and I.L. Chuang, Science 275 (1997), p. 350.
[5] I.L. Chuang, L.M.K. Vandersypen, X.L. Zhou, D.W. Leung, and S. Lloyd, Nature 393 (1998), p. 143.
[6] J.A. Jones and M. Mosca, J. Chem. Phys. 109 (1998), p. 1648.
[7] D.G. Cory, M.D. Price, and T.F. Havel, Physica D 120 (1998), p. 82.
[8] J.I. Cirac and P. Zoller, Phys. Rev. Lett. 74 (1995), p. 4091.
[9] C. Monroe, D.M. Meekhof, B.E. King, W.M. Itano, and D.J. Wineland, Phys. Rev. Lett. 75 (1995), p. 4714.
[10] A. Sorensen and K. Molmer, Phys. Rev. Lett. 82 (1999), p. 1971.
[11] J.L. Cirac and P. Zoller, Nature 404 (2000), p. 579.
[12] R. Folman, P. Kruger, D. Cassettari, B. Hessmo, T. Maier, and J. Schmiedmayer, Phys. Rev. Lett. 84 (2000), p. 4749.
[13] D. Kielpinski, C. Monroe, and D.J. Wineland, Nature 417 (2002), p. 709.
[14] S. Gulde, M. Riebe, G.P.T. Lancaster, C. Becher, J. Eschner, H. Haffner, F. Schmidt-Kaler, I.L. Chuang, and R. Blatt, Nature 421 (2003), p. 48.
[15] D. Leibfried, B. DeMarco, V. Meyer, D. Lucas, M. Barrett, J. Britton, W.M. Itano, B. Jelenkovic, C. Langer, T. Rosenband, and D.J. Wineland, Nature 422 (2003), p. 412.
[16] F. Schmidt-Kaler, H. Haffner, M. Riebe, S. Gulde, G.P.T. Lancaster, T. Deuschle, C. Becher, C.F. Roos, J. Eschner, and R. Blatt, Nature 422 (2003), p. 408.
[17] D. Leibfried, E. Knill, S. Seidelin, J. Britton, R.B. Blakestad, J. Chiaverini, D.B. Hume, W.M. Itano, J.D. Jost, C. Langer, R. Ozeri, R. Reichle, and D.J. Wineland, Nature 438 (2005), p. 639.
[18] J. Benhelm, G. Kirchmair, C.F. Roos, and R. Blatt, Nat. Phys. 4 (2008), p. 463.
[19] G.K. Brennen, C.M. Caves, P.S. Jessen, and I.H. Deutsch, Phys. Rev. Lett. 82 (1999), p. 1060.
[20] D. Jaksch, H.J. Briegel, J.I. Cirac, C.W. Gardiner, and P. Zoller, Phys. Rev. Lett. 82 (1999), p. 1975.
[21] D. Jaksch, J.I. Cirac, P. Zoller, S.L. Rolston, R. Cote, and M.D. Lukin, Phys. Rev. Lett. 85 (2000), p. 2208.
[22] O. Mandel, M. Greiner, A. Widera, T. Rom, T.W. Hansch, and I. Bloch, Nature 425 (2003), p. 937.
[23] M. Anderlini, P.J. Lee, B.L. Brown, J. Sebby-Strabley, W.D. Phillips, and J.V. Porto, Nature 448 (2007), p. 452.
[24] S. Trotzky, P. Cheinet, S. Foelling, M. Feld, U. Schnorrberger, A.M. Rey, A. Polkovnikov, E.A. Demler, M.D. Lukin, and I. Bloch, Science 319 (2008), p. 295.
[25] E. Knill, R. Laflamme, and G.J. Milburn, Nature 409 (2001), p. 46.
[26] J.L. O'Brien, G.J. Pryde, A.G. White, T.C. Ralph, and D. Branning, Nature 426 (2003), p. 264.
[27] R. Raussendorf, D.E. Browne, and H.J. Briegel, Phys. Rev. A 68 (2003), p. 022312.
[28] M.A. Nielsen, Phys. Rev. Lett. 93 (2004), p. 040503.
[29] P. Walther, K.J. Resch, T. Rudolph, E. Schenck, H. Weinfurter, V. Vedral, M. Aspelmeyer, and A. Zeilinger, Nature 434 (2005), p. 169.
[30] D.E. Browne and T. Rudolph, Phys. Rev. Lett. 95 (2005), p. 010501.
[31] Y. Lim, A. Beige, and L.C. Kwek, Phys. Rev. Lett. 95 (2005), p. 030505.
[32] R. Prevedel, P. Walther, F. Tiefenbacher, P. Bohl, R. Kaltenbaek, T. Jennewein, and A. Zeilinger, Nature 445 (2007), p. 65.
[33] C.Y. Lu, D.E. Browne, T. Yang, and J.W. Pan, Phys. Rev. Lett. 99 (2007), p. 250504.

[34] M. Varnava, D.E. Browne, and T. Rudolph, Phys. Rev. Lett. 1 (2008), p. 060502.
[35] A. Shnirman, G. Schon, and Z. Hermon, Phys. Rev. Lett. 79 (1997), p. 2371.
[36] D. Averin, Solid State Commun. 105 (1998), p. 659.
[37] Y. Makhlin, G. Schon, and A. Shnirman, Nature 398 (1999), p. 305.
[38] Y. Nakamura, Y.A. Pashkin, and J.S. Tsai, Nature 398 (1999), p. 786.
[39] Y. Makhlin, G. Schon, and A. Shnirman, Rev. Mod. Phys. 73 (2001), p. 357.
[40] Y. Yu, S.Y. Han, X. Chu, S.I. Chu, and Z. Wang, Science 296 (2002), p. 889.
[41] J.M. Martinis, S. Nam, J. Aumentado, and C. Urbina, Phys. Rev. Lett. 89 (2002), p. 117901.
[42] I. Chiorescu, Y. Nakamura, C.J.P.M. Harmans, and J.E. Mooij, Science 299 (2003), p. 1869.
[43] T. Yamamoto, Y.A. Pashkin, O. Astafiev, Y. Nakamura, and J.S. Tsai, Nature 425 (2003), p. 941.
[44] F.W. Strauch, P.R. Johnson, A.J. Dragt, C.J. Lobb, J.R. Anderson, and F.C. Wellstood, Phys. Rev. Lett. 91 (2003), p. 167005.
[45] A. Blais, A. Brinkvan den, and A. Zagoskin, Phys. Rev. Lett. 90 (2003), p. 127901.
[46] M. Grajcar, A. Izmalkov, S.H.W. van der Ploeg, S. Linzen, T. Plecenik, T. Wagner, U. Hubner, E. Il'ichev, H.G. Meyer, A.Y. Smirnov, P.J. Love, A. van den Brink, M.H.S. Amin, S. Uchaikin, and A.M. Zagoskin, Phys. Rev. Lett. 96 (2006), p. 047006.
[47] A. Wallraff, D. Schuster, A. Blais, L. Frunzio, R. Huang, J. Majer, S. Kumar, S. Girvin, and R. Schoelkopf, Nature 431 (2004), p. 162.
[48] A.O. Niskanen, K. Harrabi, F. Yoshihara, Y. Nakamura, S. Lloyd, and J.S. Tsai, Science 316 (2007), p. 723.
[49] J. Majer, J.M. Chow, J.M. Gambetta, J. Koch, B.R. Johnson, J.A. Schreier, L. Frunzio, D.I. Schuster, A.A. Houck, A. Wallraff, A. Blais, M.H. Devoret, S.M. Girvin, and R.J. Schoelkopf, Nature 449 (2007), p. 443.
[50] M. Neeley, M. Ansmann, R.C. Bialczak, M. Hofheinz, E. Lucero, A.D. O'Connell, D. Sank, H. Wang, J. Wenner, A.N. Cleland, M.R. Geller, and J.M. Martinis, Science 325 (2009), p. 722.
[51] M. Hofheinz, H. Wang, M. Ansmann, R.C. Bialczak, E. Lucero, M. Neeley, A.D. O'Connell, D. Sank, J. Wenner, J.M. Martinis, and A.N. Cleland, Nature 459 (2009), p. 546.
[52] L. DiCarlo, J.M. Chow, J.M. Gambetta, L.S. Bishop, B.R. Johnson, D.I. Schuster, J. Majer, A. Blais, L. Frunzio, S.M. Girvin, and R.J. Schoelkopf, Nature 460 (2009), p. 240.
[53] J.Q. You and F. Nori, Phys. Today 58 (2005), p. 42.
[54] J. Clarke and F.K. Wilhelm, Nature 453 (2008), p. 1031.
[55] J.M. Martinis, Quant. Info. Proc. 8 (2009), p. 81.
[56] P.M. Platzman and M.I. Dykman, Science 284 (1999), p. 1967.
[57] M.J. Lea, P.G. Frayne, and Y. Mukharsky, Fortschr. Phys. 48 (2000), p. 1109.
[58] A.J. Dahm, J.M. Goodkind, I. Karakurt, and S. Pilla, J. Low Temp. Phys. 126 (2002), p. 709.
[59] S.A. Lyon, Phys. Rev. A 74 (2006), p. 052338.
[60] M.N. Leuenberger and D. Loss, Nature 410 (2001), p. 789.
[61] B.E. Kane, Nature 393 (1998), p. 133.
[62] T.D. Ladd, J.R. Goldman, F. Yamaguchi, Y. Yamamoto, E. Abe, and K.M. Itoh, Phys. Rev. Lett. 89 (2002), p. 017901.
[63] D. Loss and D.P. DiVincenzo, Phys. Rev. A 57 (1998), p. 120.
[64] A. Imamoğlu, D.D. Awschalom, G. Burkard, D.P. DiVincenzo, D. Loss, M. Sherwin, and A. Small, Phys. Rev. Lett. 83 (1999), p. 4204.

[65] G. Burkard, D. Loss, and D.P. DiVincenzo, Phys. Rev. B 59 (1999), p. 2070.
[66] R. Vrijen, E. Yablonovitch, K. Wang, H.W. Jiang, A. Balandin, V. Roychowdhury, T. Mor, and D. DiVincenzo, Phys. Rev. A 62 (2000), p. 012306.
[67] V. Cerletti, W.A. Coish, O. Gywat, and D. Loss, Nanotechnology 16 (2005), p. R27.
[68] T. Calarco, A. Datta, P. Fedichev, E. Pazy, and P. Zoller, Phys. Rev. A 68 (2003), p. 012310.
[69] E. Pazy, E. Biolatti, T. Calarco, I. D'amico, P. Zanardi, F. Rossi, and P. Zoller, Europhys. Lett. 62 (2003), p. 175.
[70] A. Nazir, B.W. Lovett, S.D. Barrett, T.P. Spiller, and G.A.D. Briggs, Phys. Rev. Lett. 93 (2004), p. 150502.
[71] B.W. Lovett, E. Pazy, A. Nazir, S.D. Barrett, T.P. Spiller, and G.A.D. Briggs, Phys. Rev. B 72 (2005), p. 115324.
[72] P. Chen, C. Piermarocchi, L.J. Sham, D. Gammon, and D.G. Steel, Phys. Rev. B 69 (2004), p. 075320.
[73] C. Piermarocchi, P. Chen, L.J. Sham, and D.G. Steel, Phys. Rev. Lett. 89 (2002), p. 167402.
[74] G. Ramon, Y. Lyanda-Geller, T.L. Reinecke, and L.J. Sham, Phys. Rev. B 71 (2005), p. 121305.
[75] C. Emary and L.J. Sham, Phys. Rev. B 75 (2007), p. 125317.
[76] S.M. Clark, K.M.C. Fu, T.D. Ladd, and Y. Yamamoto, Phys. Rev. Lett. 99 (2007), p. 040501.
[77] S.E. Economou and T.L. Reinecke, Phys. Rev. Lett. 99 (2007), p. 217401.
[78] A.J. Ramsay, S.J. Boyle, R.S. Kolodka, J.B.B. Oliveira, J. Skiba-Szymanska, H.Y. Liu, M. Hopkinson, A.M. Fox, and M.S. Skolnick, Phys. Rev. Lett. 100 (2008), p. 197401.
[79] D. Press, T.D. Ladd, B. Zhang, and Y. Yamamoto, Nature 456 (2008), p. 218.
[80] B. Eble, C. Testelin, P. Desfonds, F. Bernardot, A. Balocchi, T. Amand, A. Miard, A. Lemaitre, X. Marie, and M. Chamarro, Phys. Rev. Lett. 102 (2009), p. 146601.
[81] J. Fischer, W.A. Coish, D.V. Bulaev, and D. Loss, Phys. Rev. B 78 (2008), p. 155329.
[82] R.G. Clark, R. Brenner, T.M. Buehler, V. Chan, N.J. Curson, A.S. Dzurak, E. Gauja, H.S. Goan, A.D. Greentree, T. Hallam, A.R. Hamilton, L.C.L. Hollenberg, D.N. Jamieson, J.C. Mccallum, G.J. Milburn, J.L. O'brien, L. Oberbeck, C.I. Pakes, S.D. Prawer, D.J. Reilly, F.J. Ruess, S.R. Schofield, M.Y. Simmons, F.E. Stanley, R.P. Starrett, C. Wellard, and C. Yang, Philos. Trans. Royal Soc. Lond. A 361 (2003), p. 1451.
[83] S.R. Schofield, N.J. Curson, M.Y. Simmons, F.J. Ruess, T. Hallam, L. Oberbeck, and R.G. Clark, Phys. Rev. Lett. 91 (2003), p. 136104.
[84] F.R. Bradbury, A.M. Tyryshkin, G. Sabouret, J. Bokor, T. Schenkel, and S. Lyon, Phys. Rev. Lett. 97 (2006), p. 176404.
[85] H. Huebl, A.R. Stegner, M. Stutzmann, M.S. Brandt, G. Vogg, F. Bensch, E. Rauls, and U. Gerstmann, Phys. Rev. Lett. 97 (2006), p. 166402.
[86] A.R. Stegner, C. Boehme, H. Huebl, M. Stutzmann, K. Lips, and M.S. Brandt, Nat. Phys. 2 (2006), p. 835.
[87] J. Wrachtrup, S.Y. Kilin, and A.P. Nizovtsev, Opt. Spectrosc. 91 (2001), p. 429.
[88] F. Jelezko, I. Popa, A. Gruber, C. Tietz, J. Wrachtrup, A. Nizovtsev, and S. Kilin, Appl. Phys. Lett. 81 (2002), p. 2160.
[89] T.A. Kennedy, J.S. Colton, J.E. Butler, R.C. Linares, and P.J. Doering, Appl. Phys. Lett. 83 (2003), p. 4190.
[90] F. Jelezko, T. Gaebel, I. Popa, A. Gruber, and J. Wrachtrup, Phys. Rev. Lett. 92 (2004), p. 076401.
[91] F. Jelezko, T. Gaebel, I. Popa, M. Domhan, A. Gruber, and J. Wrachtrup, Phys. Rev. Lett. 93 (2004), p. 130501.

[92] C. Santori, P. Tamarat, P. Neumann, J. Wrachtrup, D. Fattal, R.G. Beausoleil, J. Rabeau, P. Olivero, A.D. Greentree, S. Prawer, F. Jelezko, and P.R. Hemmer, Phys. Rev. Lett. 97 (2006), p. 247401.
[93] R.J. Epstein, F.M. Mendoza, Y.K. Kato, and D.D. Awschalom, Nat. Phys. 1 (2005), p. 94.
[94] T. Gaebel, M. Domhan, I. Popa, C. Wittmann, P. Neumann, F. Jelezko, J.R. Rabeau, N. Stavrias, A.D. Greentree, S. Prawer, J. Meijer, J. Twamley, P.R. Hemmer, and J. Wrachtrup, Nat. Phys. 2 (2006), p. 408.
[95] R. Hanson, F.M. Mendoza, R.J. Epstein, and D.D. Awschalom, Phys. Rev. Lett. 97 (2006), p. 087601.
[96] R. Hanson, O. Gywat, and D.D. Awschalom, Phys. Rev. B 74 (2006), p. 161203(R).
[97] L. Childress, M.V. Gurudev Dutt, J.M. Taylor, A.S. Zibrov, F. Jelezko, J. Wrachtrup, P.R. Hemmer, and M.D. Lukin, Science 314 (2006), p. 281.
[98] M.V. Gurudev Dutt, L. Childress, L. Jiang, E. Togan, J. Maze, F. Jelezko, A.S. Zibrov, P.R. Hemmer, and M.D. Lukin, Science 316 (2007), p. 1312.
[99] R. Hanson, V.V. Dobrovitski, A.E. Feiguin, O. Gywat, and D.D. Awschalom, Science 320 (2008), p. 352.
[100] J. Wrachtrup and F. Jelezko, J. Phys. – Condens. Matter. 18 (2006), p. S807.
[101] A.Y. Kitaev, Ann. Phys. 303 (2003), p. 2.
[102] M.H. Freedman, A. Kitaev, M.J. Larsen, and Z.H. Wang, Bull. Am. Math. Soc. 40 (2003), p. 31.
[103] S. Das Sarma, M. Freedman, and C. Nayak, Phys. Rev. Lett. 94 (2005), p. 166802.
[104] M. Dolev, M. Heiblum, V. Umansky, A. Stern, and D. Mahalu, Nature 452 (2008), p. 829.
[105] I.P. Radu, J.B. Miller, C.M. Marcus, M.A. Kastner, L.N. Pfeiffer, and K.W. West, Science 320 (2008), p. 899.
[106] J.M. Taylor, C.M. Marcus, and M.D. Lukin, Phys. Rev. Lett. 90 (2003), p. 206803.
[107] W.M. Witzel and S. Das Sarma, Phys. Rev. B 76 (2007), p. 045218.
[108] J.R. Petta, A.C. Johnson, J.M. Taylor, E.A. Laird, A. Yacoby, M.D. Lukin, C.M. Marcus, M.P. Hanson, and A.C. Gossard, Science 309 (2005), p. 2180.
[109] A. Greilich, D.R. Yakovlev, A. Shabaev, A.L. Efros, I.A. Yugova, R. Oulton, V. Stavarache, D. Reuter, A. Wieck, and M. Bayer, Science 313 (2006), p. 341.
[110] A.M. Tyryshkin, S.A. Lyon, A.V. Astashkin, and A.M. Raitsimring, Phys. Rev. B 68 (2003), p. 193207.
[111] E. Abe, J. Isoya, and K.M. Itoh, J. Supercond. 18 (2005), p. 157.
[112] A.S. Bracker, E.A. Stinaff, D. Gammon, M.E. Ware, J.G. Tischler, A. Shabaev, A.L. Efros, D. Park, D. Gershoni, V.L. Korenev, and I.A. Merkulov, Phys. Rev. Lett. 94 (2005), p. 047402.
[113] S. Takahashi, R. Hanson, J. Tolvan, M.S. Sherwin, and D.D. Awschalom, Phys. Rev. Lett. 101 (2008), p. 047601.
[114] G. Ramon and X. Hu, Phys. Rev. B 75 (2007), p. 161301.
[115] D.J. Reilly, J.M. Taylor, J.R. Petta, C.M. Marcus, M.P. Hanson, and A.C. Gossard, Science 321 (2008), p. 817.
[116] C.X. Deng and X.D. Hu, Phys. Rev. B 72 (2005), p. 165333.
[117] F. Jelezko, T. Gaebel, I. Popa, M. Domhan, A. Gruber, and J. Wrachtrup, Phys. Rev. Lett. 93 (2004), p. 130501.
[118] W. Yao, R.B. Liu, and L.J. Sham, Phys. Rev. Lett. 92 (2004), p. 217402.
[119] W. Yao, R.B. Liu, and L.J. Sham, Phys. Rev. Lett. 95 (2005), p. 030504.
[120] R.B. Liu, W. Yao, and L.J. Sham, Phys. Rev. B 72 (2005), p. 081306(R).
[121] A.V. Khaetskii, D. Loss, and L. Glazman, Phys. Rev. Lett. 88 (2002), p. 186802.
[122] J. Schliemann, A.V. Khaetskii, and D. Loss, Phys. Rev. B 66 (2002), p. 245303.

[123] R. Sousade and S. Das Sarma, Phys. Rev. B 68 (2003), p. 115322.
[124] W.A. Coish and D. Loss, Phys. Rev. B 70 (2004), p. 195340.
[125] N. Shenvi, R. Sousade, and K.B. Whaley, Phys. Rev. B 71 (2005), p. 224411.
[126] W.M. Witzel, R. Sousade, and S. Das Sarma, Phys. Rev. B 72 (2005), p. 161306(R).
[127] W. Yao, R.B. Liu, and L.J. Sham, Phys. Rev. B 74 (2006), p. 195301.
[128] C. Deng and X. Hu, Phys. Rev. B 73 (2006), p. 241303(R).
[129] S.K. Saikin, W. Yao, and L.J. Sham, Phys. Rev. B 75 (2007), p. 125314.
[130] R.B. Liu, W. Yao, and L.J. Sham, New J. Phys. 9 (2007), p. 226.
[131] W.A. Coish, J. Fischer, and D. Loss, Phys. Rev. B 77 (2008), p. 125329.
[132] L. Cywinski, W.M. Witzel, and S. Das Sarma, Phys. Rev. Lett. 102 (2009), p. 057601.
[133] K. Khodjasteh and D.A. Lidar, Phys. Rev. Lett. 95 (2005), p. 180501.
[134] W. Yao, R.B. Liu, and L.J. Sham, Phys. Rev. Lett. 98 (2007), p. 077602.
[135] W.M. Witzel and S. Das Sarma, Phys. Rev. Lett. 98 (2007), p. 077601.
[136] W.M. Witzel and S. Das Sarma, Phys. Rev. B 76 (2007), p. 241303(R).
[137] W.X. Zhang, V.V. Dobrovitski, L.F. Santos, L. Viola, and B.N. Harmon, Phys. Rev. B 75 (2007), p. 201302(R).
[138] W.X. Zhang, N.P. Konstantinidis, V.V. Dobrovitski, B.N. Harmon, L.F. Santos, and L. Viola, Phys. Rev. B 77 (2008), p. 125336.
[139] G.S. Uhrig, Phys. Rev. Lett. 98 (2007), p. 100504.
[140] B. Lee, W.M. Witzel, and S. Das Sarma, Phys. Rev. Lett. 100 (2008), p. 160505.
[141] W. Yang and R.B. Liu, Phys. Rev. Lett. 101 (2008), p. 180403.
[142] G.S. Uhrig, Phys. Rev. Lett. 102 (2009) p. 120502.
[143] M.S. Rudner and L.S. Levitov, Phys. Rev. Lett. 99 (2007), p. 036602.
[144] H. Ribeiro and G. Burkard, Phys. Rev. Lett. 102 (2009), p. 216802.
[145] W. Yao, arXiv:0905.2460 (2009).
[146] A. Greilich, A. Shabaev, D.R. Yakovlev, A.L. Efros, I.A. Yugova, D. Reuter, A. Wieck, and M. Bayer, Science 317 (2007), p. 1896.
[147] X. Xu, W. Yao, B. Sun, D.G. Steel, A.S. Bracker, D. Gammon, and L.J. Sham, Nature 459 (2009), p. 1105.
[148] I.T. Vink, K. Nowack, F. Koppens, J. Danon, Y. Nazarov, and L. Vandersypen, arXiv:0902.2659 (2009).
[149] G. Giedke, J.M. Taylor, D. D'Alessandro, M.D. Lukin, and A. Imamoglu, Phys. Rev. A 74 (2006), p. 032316.
[150] D. Stepanenko, G. Burkard, G. Giedke, and A. Imamoglu, Phys. Rev. Lett. 96 (2006), p. 136401.
[151] D. Klauser, W.A. Coish, and D. Loss, Phys. Rev. B 73 (2006), p. 205302.
[152] L.M. Duan, E. Demler, and M.D. Lukin, Phys. Rev. Lett. 91 (2003), p. 090402.
[153] M. Keller, B. Lange, K. Hayasaka, W. Lange, and H. Walther, Nature 431 (2004), p. 1075.
[154] J. McKeever, A. Boca, A. Boozer, R. Miller, J. Buck, A. Kuzmich, and H.J. Kimble, Nature 303 (2004), p. 1992.
[155] B. Darquie, M.P.A. Jones, J. Dingjan, J. Beugnon, S. Bergamini, Y. Sortais, G. Messin, A. Browaeys, and P. Grangier, Science 309 (2005), p. 454.
[156] P. Michler, A. Kiraz, C. Becher, W.V. Schoenfeld, P.M. Petroff, L. Zhang, E. Hu, and A. Imamoğlu, Science 290 (2000), p. 2282.
[157] M. Pelton, C. Santori, J. Vučković, B. Zhang, G.S. Solomon, J. Plant, and Y. Yamamoto, Phys. Rev. Lett. 89 (2002), p. 233602.
[158] J. Meijer, B. Burchard, M. Domhan, C. Wittmann, T. Gaebel, I. Popa, F. Jelezko, and J. Wrachtrup, Appl. Phys. Lett. 87 (2005), p. 261909.
[159] J. Meijer, T. Vogel, B. Burchard, I. Rangelow, L. Bischoff, J. Wrachtrup, M. Domhan, F. Jelezko, W. Schnitzler, S. Schulz, K. Singer, and F. Schmidt-Kaler, Appl. Phys. A – Mat. Sci. Proc. 83 (2006), p. 321.

[160] L.J. Sham and T.M. Rice, Phys. Rev. 144 (1966), p. 708.
[161] F.H.L. Koppens, C. Buizert, K.J. Tielrooij, I.T. Vink, K.C. Nowack, T. Meunier, L.P. Kouwenhoven, and L.M.K. Vandersypen, Nature 442 (2006), p. 766.
[162] A.V. Khaetskii and Y. Nazarov, Phys. Rev. B 61 (2000), p. 12639.
[163] A.V. Khaetskii and Y. Nazarov, Phys. Rev. B 64 (2001), p. 125316.
[164] L.M. Woods, T.L. Reinecke, and Y. Lyanda-Geller, Phys. Rev. B 66 (2002), p. 161318(R).
[165] J.L. Cheng, M.W. Wu, and C. Lu, Phys. Rev. B 69 (2004), p. 115318.
[166] V.N. Golovach, A. Khaetskii, and D. Loss, Phys. Rev. Lett. 93 (2004), p. 016601.
[167] Y.G. Semenov and K.W. Kim, Phys. Rev. Lett. 92 (2004), p. 026601.
[168] P. San-Jose, G. Zarand, A. Shnirman, and G. Schoen, Phys. Rev. Lett. 97 (2006), p. 076803.
[169] G.F. Quinteiro and C. Piermarocchi, Phys. Rev. Lett. 72 (2005), p. 045334.
[170] X.D. Hu and S. Das sarma, Phys. Rev. Lett. 96 (2006), p. 100501.
[171] W.A. Coish and D. Loss, Phys. Rev. B 72 (2005), p. 125337.
[172] M.A. Nielsen and I.L. Chuang, *Quantum Computation and Quantum Information*, Cambridge University Press, Cambridge, 2000.
[173] S.K. Saikin, C. Emary, D.G. Steel, and L.J. Sham, Phys. Rev. B 78 (2008), p. 235314.
[174] J.M. Elzerman, R. Hanson, L.H. BeverenWillems van, B. Witkamp, L.M.K. Vandersypen, and L.P. Kouwenhoven, Nature 430 (2004), p. 431.
[175] T. Fujisawa, D.G. Austing, Y. Tokura, Y. Hirayama, and S. Tarucha, Nature 419 (2002), p. 278.
[176] M. Kroutvar, Y. Ducommun, D. Heiss, M. Bichler, D. Schuh, D. Abstreiter, and J.J. Finley, Nature 432 (2004), p. 81.
[177] J. Cheng, Y. Wu, X. Xu, D. Sun, D.G. Steel, A.S. Bracker, D. Gammon, W. Yao, and L.J. Sham, Solid State Commun. 140 (2006), p. 381.
[178] J.S. Hodges, J.C. Yang, C. Ramanathan, and D.G. Cory, Phys. Rev. A 78 (2008), p. 010303.
[179] J. Du, X. Rong, N. Zhao, Y. Wang, J. Yang, and R.B. Liu, Nature 461 (2009), p. 1265.
[180] F.H.L. Koppens, K.C. Nowack, and L.M.K. Vandersypen, Phys. Rev. Lett. 100 (2008), p. 236802.
[181] S.M. Clark, K.M.C. Fu, Q. Zhang, T.D. Ladd, C. Stanley, and Y. Yamamoto, Phys. Rev. Lett. 102 (2009), p. 247601.
[182] A. Greilich, S.E. Economou, S. Spatzek, D.R. Yakovlev, D. Reuter, A.D. Wieck, T.L. Reinecke, and M. Bayer, Nat. Phys. 5 (2009), p. 262.
[183] D.P. DiVincenzo, Phys. Rev. A 51 (1995), p. 1015.
[184] S. Lloyd, Phys. Rev. Lett. 75 (1995), p. 346.
[185] K. Brunner, U. Bockelmann, G. Abstreiter, M. Walther, G. Böhm, G. Tränkle, and G. Weimann, Phys. Rev. Lett. 76 (1992), p. 3216.
[186] D. Gammon, B.V. Shanabrook, and D.S. Katzer, Phys. Rev. Lett. 67 (1991), p. 1547.
[187] T.H. Stievater, *Transient nonlinear spectroscopy of single quantum dots*, Ph.D. diss., University of Michigan, 2001.
[188] K. Brunner, G. Abstreiter, G. Böhm, G. Tränkle, and G. Weimann, Appl. Phys. Lett. 64 (1994), p. 3320.
[189] K. Brunner, G. Abstreiter, G. Böhm, G. Tränkle, and G. Weimann, Phys. Rev. Lett. 73 (1994), p. 1138.
[190] A. Zrenner, L.V. Butov, M. Hagn, G. Abstreiter, G. Böhm, and G. Weimann, Phys. Rev. Lett. 72 (1994), p. 3382.
[191] D. Gammon, E.S. Snow, and D.S. Katzer, Appl. Phys. Lett. 67 (1995), p. 2391.
[192] D. Gammon, E.S. Snow, B.V. Shanabrook, D.S. Katzer, and D. Park, Phys. Rev. Lett. 76 (1996), p. 3005.

[193] D. Gammon, E.S. Snow, B.V. Shanabrook, D.S. Katzer, and D. Park, Science 273 (1996), p. 87.
[194] M.E. Ware, E.A. Stinaff, D. Gammon, M.F. Doty, A.S. Bracker, D. Gershoni, V.L. Korenev, S.C. Bădescu, Y. Lyanda-Geller, and T.L. Reinecke, Phys. Rev. Lett. 95 (2005), p. 177403.
[195] E.A. Stinaff, M. Scheibner, A.S. Bracker, I.V. Ponomarev, V.L. Korenev, M.E. Ware, M.F. Doty, T.L. Reinecke, and D. Gammon, Science 311 (2006), p. 636.
[196] P.M. Petroff and S.P. DenBaars, Superlat. Microstruct. 15 (1994), p. 15.
[197] N. Richard, Semicond. Sci. Tech. 11 (1996), p. 1365.
[198] G. Chen, *Coherent optical spectroscopy and manipulation of GaAs quantum dots*, Ph.D. diss., University of Michigan, 2002.
[199] P.M. Petroff, A. Lorke, and A. Imamoglu, Phys. Today 54 (2001), p. 45.
[200] J.G. Tischler, A.S. Bracker, D. Gammon, and D. Park, Phys. Rev. B 66 (2002), p. 081310.
[201] W.G. Wielvan der, S. De Franceschi, J.M. Elzerman, T. Fujisawa, S. Tarucha, and K.L. P., Rev. Mod. Phys. 75 (2003), p. 1.
[202] A.C. Johnson, J.R. Petta, J.M. Taylor, A. Yacoby, M.D. Lukin, C.M. Marcus, M.P. Hanson, and A.C. Gossard, Nature 435 (2005), p. 925.
[203] F. Jelezko, T. Gaebel, I. Popa, A. Gruber, and J. Wrachtrup, Phys. Rev. Lett. 92 (2004), p. 076401.
[204] P. Tamarat, T. Gaebel, J. Rabeau, M. Khan, A.D. Greentree, H. Wilson, L.C.L. Hollenberg, S. Prawer, P.R. Hemmer, F. Jelezko, and J. Wrachtrup, Phys. Rev. Lett. 97 (2006), p. 083002.
[205] M.V.G. Dutt, J. Cheng, B. Li, X. Xu, X. Li, P.R. Berman, D.G. Steel, A.S. Bracker, D. Gammon, S.E. Economou, R.-B. Liu, and L.J. Sham, Phys. Rev. Lett. 94 (2005), p. 227403.
[206] A. Imamoglu, E. Knill, L. Tian, and P. Zoller, Phys. Rev. Lett. 91 (2003), p. 017402.
[207] W.H. Zurek, Rev. Mod. Phys. 75 (2003), p. 715.
[208] E. Joos, H.D. Zeh, C. Kiefer, D. Giulini, J. Kupsch, and I.O. Stamatescu, *Decoherence and the Appearance of a Classical World in Quantum Theory*, 2nd ed., Springer, New York, 2003.
[209] M. Schlosshauer, Rev. Mod. Phys. 76 (2004), p. 1267.
[210] S. Amasha, K. MacLean, I.P. Radu, D.M. Zumbuhl, M.A. Kastner, M.P. Hanson, and A.C. Gossard, Phys. Rev. Lett. 100 (2008), p. 046803.
[211] A. Greilich, R. Oulton, E.A. Zhukov, I.A. Yugova, M. Yakovlev, D.R. Bayer, A. Shabaev, and A.L. Efros, Phys. Rev. Lett. 96 (2006), p. 227401.
[212] F.H.L. Koppens, J.A. Folk, J.M. Elzerman, R. Hanson, L.H.W. Beverenvan, I.T. Vink, H.P. Tranitz, W. Wegscheider, L.P. Kouwenhoven, and L.M.K. Vandersypen, Science 309 (2005), p. 1346.
[213] J. Cheng, W. Yao, X. Xu, D.G. Steel, A.S. Bracker, D. Gammon, and L.J. Sham, Phys. Rev. B 77 (2008), p. 115315.
[214] L. Cywiński, W.M. Witzel, and S. Das Sarma, Phys. Rev. B 79 (2009), p. 245314.
[215] N. Bloembergen and T.J. Rowland, *Nuclear Spin Exchange in Solids: Tl^203 and Tl^205 Magnetic Resonance in Thallium and Thallic Oxide*, Phys. Rev. 97 (1955), p. 1679.
[216] P.W. Anderson, Phys. Rev. 99 (1955), p. 623.
[217] R.G. Shulman, J.M. Mays, and D.W. McCall, Phys. Rev. 100 (1955), p. 692.
[218] R.G. Shulman, B.J. Wyluda, and H.J. Hrostowski, Phys. Rev. 109 (1958), p. 808.
[219] R.K. Sundfors, Phys. Rev. 185 (1969), p. 458.
[220] W.M. Witzel and S. Das Sarma, Phys. Rev. B 74 (2006), p. 35322.
[221] W. Yang and R.B. Liu, Phys. Rev. B 78 (2008), p. 085315.
[222] W. Yang and R.B. Liu, Phys. Rev. B 79 (2009), p. 115320.

[223] A. Khaetskii, D. Loss, and L. Glazman, Phys. Rev. B 67 (2003), p. 195329.
[224] C.P. Slichter, *Principles of Magnetic Resonance*, 3rd ed., Springer-Verlag, New York, 1992.
[225] E.L. Hahn, Phys. Rev. 80 (1950), p. 580.
[226] P.P. Zanker, J. Schmidt, J. Schmiedeskamp, R.H. Acosta, and H.W. Spiess, Phys. Rev. Lett. 99 (2007), p. 263001.
[227] J.R. West, B.H. Fong, and D.A. Lidar, Phys. Rev. Lett. 104 (2010), p. 130501.
[228] A. Zrenner, J. Chem. Phys. 112 (2000), p. 7790.
[229] M. Bayer and A. Forchel, Phys. Rev. B 65 (2002), p. 041308.
[230] A. Muller, E.B. Flagg, P. Bianucci, X. Wang, D.G. Deppe, W. Ma, J. Zhang, M. Xiao, G.J. Salamo, and C.K. Shih, Phys. Rev. Lett. 99 (2007), p. 187402.
[231] T.H. Stievater, X.Q. Li, D.G. Steel, D. Gammon, D.S. Katzer, D. Park, C. Piermarocchi, and L.J. Sham, Phys. Rev. Lett. 87 (2001), p. 133603.
[232] H. Htoon, T. Takagahara, D. Kulik, O. Baklenov, A.L. Holmes Jr., and C.K. Shih, Phys. Rev. Lett. 88 (2002), p. 087401.
[233] H. Kamada, H. Gotoh, J. Temmyo, T. Takagahara, and H. Ando, Phys. Rev. Lett. 87 (2001), p. 246401.
[234] A. Zrenner, E. Beham, S. Stufler, F. Findeis, M. Bichler, and G. Abstreiter, Nature 418 (2002), p. 612.
[235] G. Chen, T.H. Stievater, E.T. Batteh, X.Q. Li, D.G. Steel, D. Gammon, D.S. Katzer, D. Park, and L.J. Sham, Phys. Rev. Lett. 88 (2002), p. 117901.
[236] J. Berezovsky, M.H. Mikkelsen, N.G. Stoltz, L.A. Coldren, and D.D. Awschalom, Science 320 (2008), p. 349.
[237] I.A. Merkulov, A.L. Efros, and M. Rosen, Phys. Rev. B 65 (2002), p. 205309.
[238] A.S. Bracker, D. Gammon, and V.L. Korenev, Semicond. Sci. Technol. 23 (2008), p. 114004.
[239] C.W. Lai, P. Maletinsky, A. Badolato, and A. Imamoglu, Phys. Rev. Lett. 96 (2006), p. 167403.
[240] A.I. Tartakovskii, T. Wright, A. Russell, V.I. Fal'ko, A.B. Van'kov, J. Skiba-Szymanska, I. Drouzas, R.S. Kolodka, M.S. Skolnick, P.W. Fry, A. Tahraoui, H.-Y. Liu, and M. Hopkinson, Phys. Rev. Lett. 98 (2007), p. 026806.
[241] B. Eble, O. Krebs, A. Lemaitre, K. Kowalik, A. Kudelski, P. Voisin, B. Urbaszek, X. Marie, and T. Amand, Phys. Rev. B 74 (2006), p. 081306.
[242] P.-F. Braun, X. Marie, L. Lombez, B. Urbaszek, T. Amand, P. Renucci, V.K. Kalevich, K.V. Kavokin, O. Krebs, P. Voisin, and Y. Masumoto, Phys. Rev. Lett. 94 (2005), p. 116601.
[243] K. Ono and S. Tarucha, Phys. Rev. Lett. 92 (2004), p. 256803.
[244] L. Viola and S. Lloyd, Phys. Rev. A 58 (1998), p. 2733.
[245] L. Viola, E. Knill, and S. Lloyd, Phys. Rev. Lett. 82 (1999), p. 2417.
[246] L. Viola, S. Lloyd, and E. Knill, Phys. Rev. Lett. 83 (1999), p. 4888.
[247] L. Viola, E. Knill, and S. Lloyd, Phys. Rev. Lett. 85 (2000), p. 3520.
[248] P.W. Shor, Phys. Rev. A 52 (1995), p. 2493.
[249] A.M. Steane, Phys. Rev. Lett. 77 (1996), p. 793.
[250] C.H. Bennett, D.P. DiVincenzo, J.A. Smolin, and W.K. Wootters, Phys. Rev. A 54 (1996), p. 3824.
[251] R. Laflamme, C. Miquel, J.P. Paz, and W.H. Zurek, Phys. Rev. Lett. 77 (1996), p. 198.
[252] D. Gottesman, Phys. Rev. A 54 (1996), p. 1862.
[253] A.M. Steane, Phys. Rev. A 68 (2003), p. 042322.
[254] D. Brunner, B.D. Gerardot, P.A. Dalgarno, G. Wüst, K. Karrai, N.G. Stoltz, P.M. Petroff, and R.J. Warburton, Science 325 (2009), p. 70.

[255] B.D. Gerardot, D. Brunner, P.A. Dalgarno, P. Öhberg, S. Seidl, M. Kroner, K. Karrai, N.G. Stoltz, P.M. Petroff, and R.J. Warburton, Nature 451 (2008), p. 441.
[256] M. Atatüre, J. Dreiser, A. Badolato, A. Högele, K. Karrai, and A. Imamoglu, Science 312 (2006), p. 551.
[257] X. Xu, Y. Wu, B. Sun, Q. Huang, J. Cheng, D.G. Steel, A.S. Bracker, D. Gammon, C. Emary, and L.J. Sham, Phys. Rev. Lett. 99 (2007), p. 097401.
[258] R. Hanson and D.D. Awschalom, Nature 453 (2008), p. 1043.
[259] G. Balasubramanian, P. Neumann, D. Twitchen, M. Markham, R. Kolesov, N. Mizuochi, J. Isoya, J. Achard, J. Beck, J. Tissler, V. Jacques, P.R. Hemmer, F. Jelezko, and J. Wrachtrup, Nature Mater. 8 (2009), p. 383.
[260] Y.S. Park, A.K. Cook, and H.L. Wang, Nano Lett. 6 (2006), p. 2075.
[261] S. Schietinger, T. Schroeder, and O. Benson, Nano Lett. 8 (2008), p. 3911.
[262] K.M.C. Fu, C. Santori, P.E. Barclay, I. Aharonovich, S. Prawer, N. Meyer, A.M. Holm, and R.G. Beausoleil, Appl. Phys. Lett. 93 (2008), p. 234107.
[263] M. Barth, N. Nuesse, B. Loechel, and O. Benson, Opt. Lett. 34 (2009), p. 1108.
[264] P. Neumann, N. Mizuochi, F. Rempp, P. Hemmer, H. Watanabe, S. Yamasaki, V. Jacques, T. Gaebel, F. Jelezko, and J. Wrachtrup, Science 320 (2008), p. 1326.
[265] L. Jiang, J.S. Hodges, J.R. Maze, P. Maurer, J.M. Taylor, D.G. Cory, P.R. Hemmer, R.L. Walsworth, A. Yacoby, A.S. Zibrov, and M.D. Lukin, Science 326 (2009), p. 267.
[266] M. Steiner, P. Neumann, J. Beck, F. Jelezko and J. Wrachtrup, Phys. Rev. B 81 (2010). p. 035205.
[267] X. Wang, X. Ren, K. Kahen, M.A. Hahn, M. Rajeswaran, S. Maccagnano-Zacher, J. Silcox, G.E. Cragg, A.L. Efros, and T.D. Krauss, Nature 459 (2009), p. 686.
[268] M. Bayer, P. Hawrylak, K. Hinzer, S. Fafard, M. Korkusinski, Z. Wasilewski, O. Stern, and A. Forchel, Science 291 (2001), p. 451.
[269] H.J. Krenner, M. Sabathil, E.C. Clark, A. Kress, D. Schuh, M. Bichler, G. Abstreiter, and J.J. Finley, Phys. Rev. Lett. 94 (2005), p. 057402.
[270] R. Songmuang, S. Kiravittaya, and O.G. Schmidt, Appl. Phys. Lett. 82 (2003), p. 2892.
[271] J.V. Barth, G. Costantini, and K. Kern, Nature 437 (2005), p. 671.
[272] M. Schmidbauer, S. Seydmohamadi, D. Grigoriev, Z.M. Wang, Y.I. Mazur, P. Schafer, M. Hanke, R. Kohler, and G.J. Salamo, Phys. Rev. Lett. 96 (2006), p. 066108.
[273] N.H. Bonadeo, G. Chen, D. Gammon, D.S. Katzer, D. Park, and D.G. Steel, Phys. Rev. Lett. 81 (1998), p. 2759.
[274] J.I. Cirac, A.K. Ekert, S.F. Huelga, and C. Macchiavello, Phys. Rev. A 59 (1999), p. 4249.
[275] C.H. Bennett, F. Bessette, G. Brassard, L. Salvail, and J. Smolin, J. Cryptol. 5 (1992), p. 3.
[276] E. Knill, R. Laflamme, and G.J. Milburn, Nature 409 (2001), p. 46.
[277] J.I. Cirac, P. Zoller, H.J. Kimble, and H. Mabuchi, Phys. Rev. Lett. 78 (1997), p. 3221.
[278] K.J. Vahala, Nature 424 (2003), p. 839.
[279] E. Peter, P. Senellart, D. Martrou, A. Lemaître, J. Hours, J.M. Gérard, and J. Bloch, Phys. Rev. Lett. 95 (2005), p. 067401.
[280] A. Scherer, O. Painter, J. Vuckovic, M. Loncar, and T. Yoshie, IEEE Trans. Nanotechnol. 1 (2002), p. 4.
[281] A. Kress, F. Hofbauer, N. Reinelt, M. Kaniber, H.J. Krenner, R. Meyer, G. Böhm, and J.J. Finley, Phys. Rev. B 71 (2005), p. 241304.
[282] Y. Akahane, T. Asano, B.S. Song, and S. Noda, Nature 425 (2003), p. 944.
[283] B.S. Song, S. Noda, T. Asano, and Y. Akahane, Nat. Mater. 4 (2005), p. 207.
[284] T. Yoshie, A. Scherer, J. Hendrickson, G. Khitrova, H.M. Gibbs, G. Rupper, C. Ell, O.B. Shchekin, and D.G. Deppe, Nature 432 (2004), p. 200.

[285] K. Hennessy, A. Badolato, M. Winger, D. Gerace, M. Atature, S. Gulde, S. Falt, E. Hu, and A. Imamoglu, Nature 445 (2007), p. 896.
[286] J.P. Reithmaier, G. Sek, A. Loffler, C. Hofmann, S. Kuhn, S. Reitzenstein, L.V. Keldysh, V.D. Kulakovskii, T.L. Reinecke, and A. Forchel, Nature 432 (2004), p. 197.
[287] N.G. Stoltz, M. Rakher, S. Strauf, A. Badolato, D.D. Lofgreen, P.M. Petroff, L.A. Coldren, and D. Bouwmeester, Appl. Phys. Lett. 87 (2005), p. 031105.
[288] D. Press, S. Gotzinger, S. Reitzenstein, C. Hofmann, A. Loffler, M. Kamp, A. Forchel, and Y. Yamamoto, Phys. Rev. Lett. 98 (2007), p. 117402.
[289] A. Muller, C.K. Shih, J. Ahn, D. Lu, and D.G. Deppe, Opt. Lett. 31 (2006), p. 528.
[290] X.D. Fan, P. Palinginis, S. Lacey, H.L. Wang, and M.C. Lonergan, Opt. Lett. 25 (2000), p. 1600.
[291] B. Min, T.J. Kippenberg, and K.J. Vahala, Opt. Lett. 28 (2003), p. 1507.
[292] N. Le Thomas, U. Woggon, O. Schops, M.V. Artemyev, M. Kazes, and U. Banin, Nano Lett. 6 (2006), p. 557.
[293] D.K. Armani, T.J. Kippenberg, S.M. Spillane, and K.J. Vahala, Nature 421 (2003), p. 925.
[294] S.M. Spillane, T.J. Kippenberg, K.J. Vahala, K.W. Goh, E. Wilcut, and H.J. Kimble, Phys. Rev. A 71 (2005), p. 013817.
[295] M. Cai, O. Painter, and K.J. Vahala, Phys. Rev. Lett. 85 (2000), p. 74.
[296] S.M. Spillane, T.J. Kippenberg, O.J. Painter, and K.J. Vahala, Phys. Rev. Lett. 91 (2003), p. 043902.
[297] T.J. Kippenberg, S.M. Spillane, D.K. Armani, and K.J. Vahala, Appl. Phys. Lett. 83 (2003), p. 797.
[298] P. Barclay, K. Srinivasan, and O. Painter, J. Opt. Soc. Am. B 20 (2003), p. 2274.
[299] K. Srinivasan, P. Barclay, M. Borselli, and O. Painter, IEEE J. Sel. Areas Commun. 23 (2005), p. 1321.
[300] K. Srinivasan, P. Barclay, O. Painter, B. Lev, and H. Mabuchi, Appl. Phys. Lett. 89 (2006), p. 131108.
[301] A. Faraon, E. Waks, D. Englund, I. Fushman, and J. Vuckovic, Appl. Phys. Lett. 90 (2007), p. 073102.
[302] A. Badolato, K. Hennessy, M. Atature, J. Dreiser, E. Hu, P.M. Petroff, and A. Imamoglu, Science 308 (2005), p. 1158.
[303] S.M. Thon, M.T. Rakher, H. Kim, J. Gudat, W.T.M. Irvine, P.M. Petroff, and D. Bouwmeester, Appl. Phys. Lett. 94 (2009), p. 111115.
[304] A. Laucht, F. Hofbauer, N. Hauke, J. Angele, S. Stobbe, M. Kaniber, G. Bohm, P. Lodahl, M.C. Amann, and J.J. Finley, New J. Phys. 11 (2009), p. 023034.
[305] M. Kaniber, A. Neumann, A. Laucht, M.F. Huck, M. Bichler, M.C. Amann, and J.J. Finley, New J. Phys. 11 (2009), p. 013031.
[306] M.T. Rakher, N.G. Stoltz, L.A. Coldren, P.M. Petroff, and D. Bouwmeester, Appl. Phys. Lett. 93 (2008), p. 091118.
[307] M.T. Rakher, N.G. Stoltz, L.A. Coldren, P.M. Petroff, and D. Bouwmeester, Phys. Rev. Lett. 102 (2009), p. 097403.
[308] E.B. Flagg, A. Muller, J.W. Robertson, S. Founta, D.G. Deppe, M. Xiao, W. Ma, G.J. Salamo, and C.K. Shih, Nat. Phys. 5 (2009), p. 203.
[309] W. Yao, R.B. Liu, and L.J. Sham, J. Appl. Phys. 101 (2007), p. 081721.
[310] K. Bergmann, H. Theuer, and B.W. Shore, Rev. Mod. Phys. 70 (1998), p. 1003.
[311] C.E. Pryor and M.E. Flatte, Appl. Phys. Lett. 88 (2006), p. 233108.
[312] Y. Wu, E.D. Kim, X. Xu, J. Cheng, D.G. Steel, A.S. Bracker, D. Gammon, S.E. Economou, and L.J. Sham, Phys. Rev. Lett. 99 (2007), p. 097402.
[313] D. Press, K. De Greve, P.L. McMahon, T.D. Ladd, B. Friess, C. Schneider, M. Kamp, S. Hofling, A. Forchel, and Y. Yamamoto, Nat. Photo. 4 (2010), p. 347.

[314] D. Goswami, Phys. Report 374 (2003), p. 385.
[315] G. Ortner, M. Bayer, A. Larionov, V.B. Timofeev, A. Forchel, Y.B. Lyanda-Geller, T.L. Reinecke, P. Hawrylak, S. Fafard, and Z. Wasilewski, Phys. Rev. Lett. 90 (2003), p. 086404.
[316] H.J. Krenner, E.C. Clark, T. Nakaoka, M. Bichler, C. Scheurer, G. Abstreiter, and J.J. Finley, Phys. Rev. Lett. 97 (2006), p. 076403.
[317] B.D. Gerardot, S. Strauf, M.J.A. Doodde, A.M. Bychkov, A. Badolato, K. Hennessy, E. Hu, D. Bouwmeester, and P.M. Petroff, Phys. Rev. Lett. 95 (2005), p. 137403.
[318] M. Scheibner, M.F. Doty, I.V. Ponomarev, A.S. Bracker, E.A. Stinaff, V.L. Korenev, T.L. Reinecke, and D. Gammon, Phys. Rev. B 75 (2007), p. 245318.
[319] M. Scheibner, M. Yakes, A.S. Bracker, I.V. Ponomarev, M.F. Doty, C.S. Hellberg, L.J. Whitman, T.L. Reinecke, and D. Gammon, Nat. Phys. 4 (2008), p. 291.
[320] R.S. Judson and H. Rabitz, Phys. Rev. Lett. 68 (1992), p. 1500.
[321] W.S. Warren, H. Rabitz, and M. Dahleh, Science 259 (1993), p. 1581.
[322] H. Rabitz, R. Vivie-Riedlede, M. Motzkus, and K. Kompa, Science 288 (2000), p. 824.
[323] A. Shabaev, A.L. Efros, D. Gammon, and I.A. Merkulov, Phys. Rev. B 68 (2003), p. 201305(R).
[324] M. Friesen, C. Tahan, R. Joynt, and M.A. Eriksson, Phys. Rev. Lett. 92 (2004), p. 037901.
[325] C. Emary, X. Xu, D.G. Steel, S. Saikin, and L.J. Sham, Phys. Rev. Lett. 98 (2007), p. 047401.
[326] D. Kim, S.E. Economou, S.C. Badescu, M. Scheibner, A.S. Bracker, M. Bashkansky, T.L. Reinecke, and D. Gammon, Phys. Rev. Lett. 101 (2008), p. 236804.
[327] U. Bockelmann and G. Bastard, Phys. Rev. B 42 (1990), p. 8947.
[328] B. Ohnesorge, M. Albrecht, J. Oshinowo, A. Forchel, and Y. Arakawa, Phys. Rev. B 54 (1996), p. 11532.
[329] S. Cortez, O. Krebs, S. Laurent, M. Senes, X. Marie, P. Voisin, R. Ferreira, G. Bastard, J.M. Gérard, and T. Amand, Phys. Rev. Lett. 89 (2002), p. 207401.
[330] S. Trumm, M. Wesseli, H.J. Krenner, D. Schuh, M. Bichler, J.J. Finley, and M. Betz, Appl. Phys. Lett. 87 (2005), p. 153113.
[331] N.H. Bonadeo, *Nano-optics: Coherent Optical Spectroscopy of Single Semiconductor Quantum Dots*, Ph.D. diss., The University of Michigan, 1999.
[332] M. Atatüre, J. Dreiser, A. Badolato, and A. Imamoglu, Nat. Phys. 3 (2007), p. 101.
[333] M.H. Mikkelsen, J. Berezovsky, N.G. Stoltz, L.A. Coldren, and D.D. Awschalom, Nature Phys. 3 (2007), p. 770.
[334] D.F.V. James, P.G. Kwiat, W.J. Munro, and A.G. White, Phys. Rev. A 64 (2001), p. 052312.
[335] D.G. Cory, A.F. Hahmy, and T.F. Havel, Proc. Natl. Acad. Sci. USA 94 (1997), p. 1634.
[336] S. Takeuchi, J. Kim, Y. Yamamoto, and H.H. Hogue, Appl. Phys. Lett. 74 (1999), p. 1063.
[337] P. Barclay, K. Srinivasan, and O. Painter, Opt. Exp. 13 (2005), p. 801.
[338] K. Srinivasan, P.E. Barclay, M. Borselli, and O. Painter, Phys. Rev. B 70 (2004), p. 081306.
[339] P.E. Barclay, K. Srinivasan, M. Borselli, and O. Painter, Appl. Phys. Lett. 85 (2004), p. 4.
[340] M.J. Cryan, J. Lightwave Technol. 27 (2009), p. 4841.
[341] Y. Sugimoto, Y. Tanaka, N. Ikeda, Y. Nakamura, K. Asakawa, and K. Inoue, Opt. Exp. 12 (2004), p. 1090.
[342] J. Crisp and B. Elliott, *Introduction to Fiber Optics*, Newnes, Oxford, UK, 2005.
[343] A. Kuhn, M. Hennrich, and G. Rempe, Phys. Rev. Lett. 89 (2002), p. 067901.
[344] A.D. Boozer, A. Boca, R. Miller, T.E. Northup, and H.J. Kimble, Phys. Rev. Lett. 98 (2007), p. 193601.

[345] A.S. Parkins and H.J. Kimble, J. Opt. B: Quant. Semiclass. Opt. 1 (1999), p. 496.
[346] M. Fleischhauer, S.F. Yelin, and M.D. Lukin, Opt. Commun. 179 (2000), p. 395.
[347] W. Yao, R.B. Liu, and L.J. Sham, J. Opt. B: Quant. Semiclass. Opt. 7 (2005), p. S318.
[348] D. Fattal, R. Beausoleil, and Y. Yamamoto, quant-ph/0606204 (2006).
[349] X. Marie, T. Amand, P. Le Jeune, M. Paillard, P. Renucci, L.E. Golub, V.D. Dymnikov, and E.L. Ivchenko, Phys. Rev. B 60 (1999), p. 5811.
[350] M.D. Lukin, S.F. Yelin, and M. Fleischhauer, Phys. Rev. Lett. 84 (2000), p. 4232.
[351] R.J. Levis, G.M. Menkir, and H. Rabitz, Science 292 (2001), p. 709.
[352] H.M. Wiseman and G.J. Milburn, Phys. Rev. Lett. 70 (1993), p. 548.
[353] J.M. Geremia, J.K. Stockton, and H. Mabuchi, Science 304 (2004), p. 270.
[354] S.J. Enkvan, J.I. Cirac, and P. Zoller, Science 279 (1998), p. 205.
[355] H.J. Briegel, W. Dür, J.I. Cirac, and P. Zoller, Phys. Rev. Lett. 81 (1998), p. 5932.
[356] T. Chen and R.B. Liu (unpublished).
[357] F. Verluise, V. Laude, Z. Cheng, C. Spielmann, and P. Tournois, Opt. Lett. 25 (2000), p. 575.
[358] C.W. Hillegas, J.X. Tull, D. Goswami, D. Strickland, and W.S. Warren, Opt. Lett. 19 (1994), p. 737.
[359] X.Q. Li, T.H. Zhang, C.N. Borca, and S.T. Cundiff, Phys. Rev. Lett. 96 (2006), p. 57406.
[360] M. Cho, Chem. Rev. 108 (2008), p. 1331.
[361] S. Mukamel, Ann. Rev. Phys. Chem. 51 (2000), p. 691.
[362] P.F. Tian, D. Keusters, Y. Suzaki, and W.S. Warren, Science 300 (2003), p. 1553.
[363] P.Y. Yu and M. Cardona, *Fundamentals of Semiconductors*, 1st ed., Springer, Berlin, 1996.
[364] A.V. Koudinov, I.A. Akimov, Y.G. Kusrayev, and F. Henneberger, Phys. Rev. B 70 (2004), p. 241305.
[365] D. Paget, G. Lampel, and B. Sapoval, Phys. Rev. B 15 (1977), p. 5780.
[366] D. Paget, T. Amand, and J.P. Korb, Phys. Rev. B 77 (2008), p. 245201.
[367] P. Maletinsky, M. Kroner, and A. Imamoglu, Nat. Phys. 5 (2009), p. 407.
[368] S. Popescu, A.J. Short, and A. Winter, Nature. Phys. 2 (2006), p. 754.

Appendix A. Hole-mixing and selection rules in a QD

In the III–V bulk material, the top of valance band occurs at the Γ point of the Brillouin zone (Figure A1). The spin-orbit coupling of the *p*-orbit splits the *p*-type valance band to a quadruplet with Γ_8 symmetry (or a total angular momentum $J=3/2$) and a doublet with Γ_7 symmetry (or a total angular momentum $J=1/2$). The Γ-7 band lies much lower in energy than the Γ-8 bands. From now on, we focus on the bands derived from the $J=3/2$ quadruplet, which are described by the Luttinger Hamiltonian in the framework of effective-mass theory [363]

$$H_L = \frac{1}{2m_0}\begin{pmatrix} P_1 & Q & R & 0 \\ Q^* & P_2 & 0 & R \\ R^* & 0 & P_2 & -Q \\ 0 & R^* & -Q^* & P_1 \end{pmatrix}, \tag{A1}$$

expressed in a matrix form on the basis $\{|J_z=3/2\rangle, |J_z=1/2\rangle, |J_z=-1/2\rangle, |J_z=-3/2\rangle\}$, with

$$P_1 = (\gamma_1 - 2\gamma_2)k_z^2 + (\gamma_1 + \gamma_2)\left(k_x^2 + k_y^2\right), \tag{A2a}$$

$$P_2 = (\gamma_1 + 2\gamma_2)k_z^2 + (\gamma_1 - \gamma_2)\left(k_x^2 + k_y^2\right), \tag{A2b}$$

$$Q = -2\sqrt{3}\gamma_3 k_z\left(k_x - ik_y\right), \tag{A2c}$$

$$R = -\sqrt{3}\left[\gamma_2\left(k_x^2 - k_y^2\right) - 2i\gamma_3 k_x k_y\right], \tag{A2d}$$

where $\gamma_{1,2,3}$ denote the Luttinger coefficients. The $|J_z = \pm 3/2\rangle$ and $|J_z = \pm 1/2\rangle$ bands are usually referred to as the HH and LH bands, respectively, by their different effective mass in the z-direction.

Hole mixing effects are caused by the QD confinement potential $V_h(x, y, z)$. Here for simplicity, the growth direction z is assumed to be along the [001] direction. For other growth directions, the discussions below can be generalized straightforwardly, and the essential conclusions would not be changed. Strong quantum confinement in the growth (z) direction lifts the four-fold degeneracy at Γ point (Figure A2(a)). The LH states actually have a larger in-plane effective mass and therefore their dispersion tend to cross into the HH bands at finite in-plane wavevector $k_\perp$ (Figure A2(b)). Spin-orbit coupling thus results in anti-crossing and the mixture of the HH and LH bands (Figure A2(c)) [363].

Let us first consider the zeroth-order approximation for the hole-mixing. When the confinement size along the z-direction is much smaller than the lateral size, we have $\langle k_z^2\rangle \gg \langle k_x^2\rangle, \langle k_y^2\rangle$. If the off-diagonal couplings Q and R are neglected, the Hamiltonian is diagonal on the basis of the angular momentum quantized along the growth direction. The HH and LH, with kinetic energy P_1 and P_2, are characterized by their angular momentum states as $|\pm 3/2\rangle$ and $|\pm 1/2\rangle$, respectively. The HH and the LH are separated by an energy $\Delta_{HL} = 2\gamma_2\langle k_z^2\rangle/m_0$ [363]. The hole-mixing is induced by Q and R terms. The Q terms couple $|\pm 3/2\rangle$ to $|\pm 1/2\rangle$, and the R terms couple $|\pm 3/2\rangle$ to $|\mp 1/2\rangle$. As we usually have $\Delta_{HL} \gg \langle Q\rangle$, $\langle P\rangle$, the zeroth-order approximation and the corresponding selection rules determined by the angular momentum conservation are often adequate to understand the optical transitions.

For small QDs, the mixing may be important. Now let us consider the HH–LH mixing in different situations.

First, we consider a confinement potential with rotational symmetry about the growth direction. If we assume $\gamma_2 = \gamma_3$, the Hamiltonian has the rotational symmetry. The HH and LH states coupled by the Q and R terms must have different orbital angular momentum. So the LH components mixed into, e.g., the HH ground state are not optically active. In this case, the mixing has no effect on the optical transitions but a reduction of the dipole matrix element. The problem comes from the fact that in reality we usually do not have a cylindrical $V(x, y, z)$ or $\gamma_2 \neq \gamma_3$ (since the lattice has no spherical symmetry).

Let us still make the assumption that the confinement potential V has inversion symmetry in the z-direction, which is reasonably fulfilled in fluctuation QDs. Since the Q terms are linear

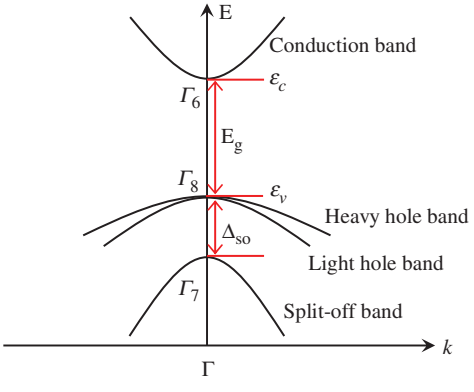

Figure A1. Bulk band structures of direct bandgap III–V semiconductors.

in the k_z, they couple HH and LH states with different parities which are separated by large energies due to the strong confinement in the z-direction. In the even parity ground state, the hole mixing effect caused by the Q terms is negligible, especially in optical transitions. Thus, we only need to consider the coupling induced by the R terms. Thus the optically active components of the HH ground states are

$$|H\pm\rangle = |\pm 3/2\rangle + \eta|\mp 1/2\rangle, \tag{A3}$$

where $\eta \sim L_z^2/L_{x,y}^2$ (with L_z and $L_{x,y}$ being the vertical and lateral confinement sizes, respectively) and normalization is understood. The dipole matrix elements between the electron spin states $|\pm 1/2\rangle$ and the trion states $|t\pm\rangle$ which contains the HH in $|H\pm\rangle$ are (in arbitrary units)

$$\langle t\pm|\mathbf{d}\cdot\sigma_\pm|\pm 1/2\rangle = 1, \tag{A4a}$$

$$\langle t\pm|\mathbf{d}\cdot\sigma_\mp|\pm 1/2\rangle = \eta', \tag{A4b}$$

$$\langle t\mp|\mathbf{d}\cdot\sigma_\pm|\pm 1/2\rangle = 0, \tag{A4c}$$

$$\langle t\mp|\mathbf{d}\cdot\sigma_\mp|\pm 1/2\rangle = 0, \tag{A4d}$$

where $\sigma_\pm$ is the circular polarization of a light normally propagating and $\eta' \sim \eta$. The selection rules are shown in Figure A3. The two subspaces $\{|+1/2\rangle, |t+\rangle\}$ and $\{|-1/2\rangle, |t-\rangle\}$ are disconnected under optical coupling, which means the electron spin along the growth direction is still conserved unless an external magnetic field is applied along an in-plane direction. With a magnetic field along the x-direction, we can choose a light with the polarization, e.g.,

$$\tilde{\sigma}_+ \equiv \sigma_+ - \eta'\sigma_-, \tag{A5}$$

which couples the electron spin eigenstates $|\pm x\rangle$ to the common trion state $|t+\rangle$ with renormalized dipole matrix elements $(1 \pm \eta'^2)$. The theories for the case without hole mixing can be generalized simply by replacing the dipole matrix elements there with the renormalized ones.

In systems without the inversion symmetry, which is often the case for InAs self-assembled QDs, the mixing would make the two ground HH states to be

$$|H+\rangle = |+3/2\rangle + \zeta|+1/2\rangle + \eta|-1/2\rangle + \xi|-3/2\rangle, \tag{A6}$$

$$|H-\rangle = |-3/2\rangle + \zeta|-1/2\rangle + \eta|+1/2\rangle + \xi|+3/2\rangle, \tag{A7}$$

where η and ζ are small numbers ($\lesssim$10% for typical self-assembled QDs), and $\xi \sim \eta\zeta$. Now the dipole matrix elements are

$$\langle t\pm|\mathbf{d}\cdot\sigma_\pm|\pm 1/2\rangle = 1, \tag{A8a}$$

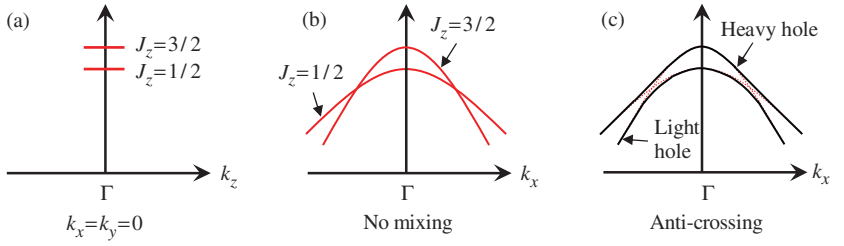

Figure A2. Dispersion relation of the $|J_z = 3/2\rangle$ and $|J_z = 1/2\rangle$ valence bands in a quantum well [363]. (a) Energy shift due to the confinement in the growth direction. (b) In-plane dispersion of the two valance bands when the 'off-diagonal' terms are neglected (without mixing). (c) Level anti-crossing when 'off-diagonal' terms are included.

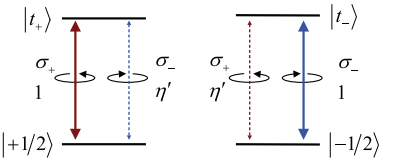

Figure A3. Selection rules of optical transitions in a doped QD with inversion symmetry along the growth direction. The solid lines denote the allowed transitions, and the dashed lines denotes the 'forbidden' transitions which have a relative dipole matrix element η'.

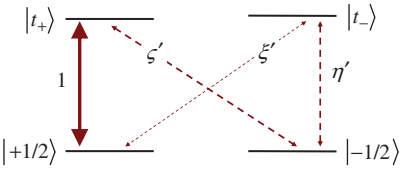

Figure A4. The relative dipole matrix elements in a doped QD with irregular shape but a large lateral to vertical size ratio. The light polarization is assumed to σ_+. The solid lines denote the allowed transitions, and the dashed lines denotes the 'forbidden' transitions which have relative dipole matrix elements η', ζ' and ξ'.

$$\langle t \pm |\mathbf{d}\cdot\sigma_{\mp}| \pm 1/2\rangle = \eta', \tag{A8b}$$

$$\langle t \mp |\mathbf{d}\cdot\sigma_{\mp}| \pm 1/2\rangle = \zeta', \tag{A8c}$$

$$\langle t \mp |\mathbf{d}\cdot\sigma_{\pm}| \pm 1/2\rangle = \xi', \tag{A8d}$$

with $\eta' \sim \eta$, $\zeta' \sim \zeta$ and $\xi' \sim \xi$, all being small numbers. Interestingly, all the states are now optically connected. Thus, it is possible to perform an arbitrary spin rotation by optical control without applying an external magnetic field or tilting the light beam from the normal direction. (For a QD without a symmetry axis, the normal direction is not special.) For example, if the light polarization is chosen to be $\mathbf{X} \equiv \sigma_+ + \sigma_-$, the dipole matrix elements between the spin states $|\pm x\rangle$ and the trion states $|t \pm x\rangle \equiv |t+\rangle \pm |t-\rangle$ are

$$\langle t + x|\mathbf{d}\cdot\mathbf{X}| + x\rangle = 1 + \eta' + \zeta' + \xi', \tag{A9a}$$

$$\langle t + x|\mathbf{d}\cdot\mathbf{X}| - x\rangle = 0, \tag{A9b}$$

$$\langle t - x|\mathbf{d}\cdot\mathbf{X}| + x\rangle = 0, \tag{A9c}$$

$$\langle t - x|\mathbf{d}\cdot\mathbf{X}| - x\rangle = 1 + \eta' - \zeta' - \xi'. \tag{A9d}$$

Thus the AC Stark effect induces an effective magnetic field along the x-direction, which, as compared the effective magnetic field along the growth direction induced by a circularly polarized light, is reduced by a factor $\sim(\zeta' + \xi')$. To realize an arbitrary rotation without a static magnetic field, the optical field would need to be much stronger than with a static magnetic field, unless the QD lateral size is comparable to the vertical size (such as in the case nanocrystals or spherical QDs formed by chemical deposition).

The HH–HL hole mixing coefficients ζ and η can be extracted using the polarization dependent absorption spectroscopy as described in Ref. [364]. For typical InAs self-assembled dots studied by Steel's group, ζ is negligible and η varies in the range $\sim$0.1–0.2 for different dots [147,257].

Appendix B. Theory of electron spin decoherence by interacting nuclear spins

In this appendix, we give the details on the theory of electron spin decoherence by interacting nuclear spins in a strong magnetic field (≥ 1 T), which was first formulated in Ref [127].

The mesoscopic system consists of an electron with a spin vector $\hat{\mathbf{S}}_e$ and N nuclear spins, $\hat{\mathbf{J}}_n$, with Zeeman energies Ω_e and ω_n under a magnetic field B_{ext}, respectively, where n denotes both positions and isotope types (e.g. ^{75}As, ^{69}Ga and ^{71}Ga in GaAs). The interaction can be separated as 'diagonal' terms which involve only the spin vector components along the field (z) direction and 'off-diagonal' terms which involve spin flips. Because the electron Zeeman energy is much larger than the strength of the hyperfine interaction, the off-diagonal term is eliminated by a standard canonical transformation, with the second-order correction left as the hyperfine-mediated nuclear interaction [127], called the extrinsic interaction in Section 2.4.1. For the same reason, the off-diagonal part of the nuclear interaction contributes only when the terms conserve the Zeeman energies (so-called secular terms in the NMR terminology). Hence, the non-secular terms are negligible. The total reduced Hamiltonian is obtained for the limit of long longitudinal electron spin relaxation time ($T_1 \to \infty$),

$$\hat{H}_{red} = \hat{H}e + \hat{H}N + \sum_{\pm} |\pm\rangle \hat{H}^{\pm} \langle\pm|, \tag{B1}$$

with $\hat{H}_e = \Omega_e \hat{S}_e^z$, $\hat{H}_N = \omega_n \hat{J}_n^z$, and the interaction terms,

$$\hat{H}^{\pm} = \pm \hat{H}_A + \hat{H}_B + \hat{H}_D \pm \hat{H}_E, \tag{B2}$$

given by

$$\hat{H}_A = \sum_{n \neq m}{}' \frac{a_n a_m}{4\Omega_e} \hat{J}_n^+ \hat{J}_m^- \equiv \sum_{n \neq m}{}' A_{n,m} \hat{J}_n^+ \hat{J}_m^-, \tag{B3a}$$

$$\hat{H}_B = \sum_{n \neq m}{}' B_{n,m} \hat{J}_n^+ \hat{J}_m^-, \tag{B3b}$$

$$\hat{H}_D = \sum_{n < m} D_{n,m} \hat{J}_n^z \hat{J}_m^z, \tag{B3c}$$

$$\hat{H}_E = \sum_n \frac{a_n}{2} \hat{J}_n^z \equiv \sum_n E_n \hat{J}_n^z, \tag{B3d}$$

where $|\pm\rangle$ are the eigenstates of $\hat{S}_e^z$, the summation with a prime runs only over the homonuclear pairs, the subscript A denotes the extrinsic hyperfine mediated interaction, B the off-diagonal part of the intrinsic nuclear interaction, D the diagonal part of the intrinsic interaction and E the diagonal part of the contact electron–nuclear hyperfine interaction. The hyperfine energy, determined by the electron wavefunction, has a typical energy scale $E_n \sim a_n \sim 10^6\,\mathrm{s}^{-1}$ for a dot with about 10^6 nuclei [365]. The sum, $\mathcal{A} \equiv \sum_n a_n$, is the *hyperfine constant* depending only on the material. The intrinsic nuclear spin-spin interaction has the near-neighbor coupling strength $B_{n,m} \sim D_{n,m} \sim 10^2\,\mathrm{s}^{-1}$. The extrinsic hyperfine-mediated interaction, which is unrestricted in range within the QD and associated with opposite signs for opposite electron spin states, has an energy scale dependent on the field strength, $A_{n,m} \sim 1$–$10\,\mathrm{s}^{-1}$ for field $\sim$40–1 T. Thus, the intrinsic interaction dominates local pair interactions, while non-local pairs are driven by the extrinsic mechanism.

B.1. Formal theory of decoherence in a nuclear spin bath

After the initialization step of the electron spin qubit, the electron-nuclear spin system is prepared in a product state with the nuclear spins in a thermal state with temperature T, described by the density matrix

$$\hat{\rho}(0) = \hat{\rho}^e(0) \otimes \hat{\rho}^N. \tag{B4}$$

The time evolution of the reduced density matrix of the electron spin,

$$\hat{\rho}^{\mathrm{e}}(t) = \mathrm{Tr}_{\mathrm{N}}\hat{\rho}(t), \tag{B5}$$

obtained by tracing over the nuclear spins, may be expressed in the form,

$$\rho^{\mathrm{e}}_{\mu,\nu}(t) = \sum_{\mu',\nu'} \mathcal{L}_{\mu,\nu;\mu',\nu'}(t)\rho^{\mathrm{e}}_{\mu',\nu'}(0), \tag{B6}$$

where $\rho^{\mathrm{e}}_{\mu,\nu} \equiv \langle\mu|\rho^{\mathrm{e}}|\nu\rangle$, and $|\mu\rangle$, $|\nu\rangle \in \{|+\rangle, |-\rangle\}$. The superoperator or correlation function $\mathcal{L}_{\mu,\nu;\mu',\nu'}$ can be expressed in terms of the evolution operator and contains the information on the electron spin relaxation and decoherence.

The Hamiltonians of Equation (B1) for the $T_1 \to \infty$ limit conserves the electron $\hat{S}^e_z$ quantum number: $[\hat{H}, \hat{S}^e_z] = 0$. Hence, the correlation function has the following properties,

$$\mathcal{L}_{\mu,\nu;\mu',\nu'}(t) = \mathcal{L}_{\mu,\nu}(t)\delta_{\mu,\mu'}\delta_{\nu,\nu'}, \tag{B7a}$$

$$\mathcal{L}_{\mu,\mu}(t) = 1, \tag{B7b}$$

$$\mathcal{L}_{+,-}(t) = \mathcal{L}^*_{-,+}(t), \tag{B7c}$$

and the specific expression for the FID,

$$\mathcal{L}_{+,-}(t) = e^{-i\Omega_e t}\mathrm{Tr}_{\mathrm{N}}\left[\hat{\rho}^N e^{+i\hat{H}^- t} e^{-i\hat{H}^+ t}\right], \tag{B8}$$

which can be straightforwardly extended to dynamics under pulse control.

The ensemble of nuclear spins, at temperature $T \gtrsim \omega_n \gg A_{n,m}$, $B_{n,m}$, $D_{n,m}$, E_n, may be approximated by the density matrix,

$$\hat{\rho}^{\mathrm{N}} \approx e^{-\hat{H}_{\mathrm{N}}/T} = \sum_{\mathcal{J}} P_{\mathcal{J}}|\mathcal{J}\rangle\langle\mathcal{J}|, \tag{B9}$$

where $|\mathcal{J}\rangle \equiv \bigotimes_n |j_n\rangle$, j_n being the quantum number of nuclear spin n in the magnetic field direction. $P_{\mathcal{J}}$ is the thermal distribution factor. While *single-system dynamics* (i.e. with the nuclear bath initially in a pure state $|\mathcal{J}\rangle$) could be the ultimate aim for quantum applications, we note that all experiments to date are performed under the ensemble scenario, either in a spatial ensemble of many dots [109,177,205] or in a single dot with repeated measurements [112,161,202], where the statistical average over the initial configurations is needed.

The correlation function $\mathcal{L}_{+,-}(t)$ can then be generally expressed as,

$$\mathcal{L}_{+,-}(t) = \sum_{\mathcal{J}} P_{\mathcal{J}} e^{-i\phi_{\mathcal{J}}(t)}\left|\langle\mathcal{J}^-(t)|\mathcal{J}^+(t)\rangle\right|. \tag{B10}$$

In FID, $|\mathcal{J}^{\pm}(t)\rangle = e^{-i\hat{\mathrm{H}}^{\pm}t}|\mathcal{J}\rangle$ and $\phi_{\mathcal{J}}(t) = (\Omega_e + \mathcal{E}_{\mathcal{J}})t$ where $\mathcal{E}_{\mathcal{J}} = \sum_n j_n a_n$ is the contribution to the electron Zeeman splitting from the Overhauser field in the nuclear configuration $|\mathcal{J}\rangle$.

B.2. Pair-correlation approximation and pseudo-spin picture

The solution to the single-system evolution $|\mathcal{J}^{\pm}(t)\rangle$ is key to both single spin decoherence and ensemble decoherence behaviors under FID and pulse controls. Due to the slowness of the nuclear spin interacting dynamics, this evolution is well-described by the pair-correlation approximation for the nuclear spin bath [127,129]. Within a time t much smaller than the inverse nuclear interaction strength, the total number of pair flip excitations N_{flip} is much smaller than the number of nuclei N. The probability of having pair flips correlated can be estimated to be $P_{\mathrm{corr}} \sim 1 - e^{-qN^2_{\mathrm{flip}}/N}$ (q being the number of homo-nuclear nearest neighbors), which is negligible in the relevant timescale of electron spin decoherence [127,129,130,134,220]. Thus, the pair flips as elementary excitations from the initial state can be treated as

independent of each other, with a relative error $\epsilon \lesssim P_{\rm corr}$. Then the single-system dynamics $|\mathcal{J}^{\pm}(t)\rangle$ can be described by the excitation of pair correlations as non-interacting quasi-particles from the 'vacuum' state $|\mathcal{J}\rangle$, driven by the 'low-energy' effective Hamiltonian,

$$\hat{H}^{\pm}_{\mathcal{J}} = \sum_k \hat{\mathcal{H}}^{\pm}_k \equiv \sum_k \mathbf{h}^{\pm}_k \cdot \hat{\sigma}_k/2, \tag{B11}$$

which has been written in such a way that the pair correlations are interpreted as 1/2-pseudo-spins, represented by the Pauli matrix $\hat{\sigma}_k$, with k labelling all possible flip-pairs [134]. The time evolution from the initial state $|\mathcal{J}\rangle$ can be viewed as the rotation of the pseudo-spins, initially all polarized along the $+z$ pseudo-axis: $\bigotimes_k |\uparrow_k\rangle$, under the effective pseudo-magnetic field,

$$\mathbf{h}^{\pm}_k \equiv (\pm 2A_k + 2B_k, 0, D_k \pm E_k), \tag{B12}$$

where, for the electron spin state $|\pm\rangle$, $\pm A_k$ and B_k are the pair-flip transition amplitudes contributed by the extrinsic nuclear interaction $\hat{\rm H}_A$ and the intrinsic nuclear interaction $\hat{\rm H}_B$, respectively, and D_k and $\pm E_k$ are the energy cost of the pair flip contributed by the diagonal nuclear coupling $\hat{\rm H}_D$ and the hyperfine interaction $\hat{\rm H}_E$, respectively. Then the decoherence can be analytically derived as

$$\mathcal{L}^{s}_{+,-}(t) = \prod_k \left|\langle\psi^{-}_k(t)|\psi^{+}_k(t)\rangle\right| \approx \prod_k e^{-\delta_k^2/2}, \tag{B13}$$

where $|\psi^{\pm}_k(t)\rangle$ are the two conjugated states of pseudo-spin k at time t conditioned on the electron spin state $|\pm\rangle$. In FID, $|\psi^{\pm}_k(t)\rangle \equiv e^{-i\hat{\mathcal{H}}^{\pm}_k t}|\uparrow_k\rangle$; while with a π pulse to flip the electron at $t=\tau$, $|\psi^{\pm}_k(t>\tau)\rangle \equiv e^{-i\hat{\mathcal{H}}^{\mp}_k (t-\tau)} e^{-i\hat{\mathcal{H}}^{\pm}_k \tau}|\uparrow_k\rangle$. $\delta^2_k \equiv 1 - \left|\langle\psi^{-}_k|\psi^{+}_k\rangle\right|^2$ possesses a simple geometrical interpretation: the squared distance between the two conjugate pseudo-spin states on the Bloch sphere, which quantifies the entanglement between the electron spin and the pseudo-spin.

A couple of justified simplifications can provide an understanding of the effects of various mechanisms on the spin decoherence. First, the energy cost by the diagonal nuclear coupling (D_k) can be neglected as it is by three orders of magnitude smaller than that by hyperfine interaction (E_k). Second, for near-neighbor pair flips, the intrinsic nuclear interaction is much stronger than the hyperfine mediated one for the field strength under consideration. Third, for non-local pair flips, the intrinsic interaction is negligible due to its finite-range characteristic. Thus we can separate the flip-pairs into two subsets, K_A, which contains $O(N^2)$ non-local flip-pairs driven by the effective pseudo-magnetic field $\mathbf{h}^{\pm}_k \approx (\pm 2A_k, 0, \pm E_k)$, and $\in K_B$, which contains $O(N)$ near-neighbor flip-pairs driven by $\mathbf{h}^{\pm}_k \approx (2B_k, 0, \pm E_k)$. The conjugate pseudo-spins will precess along opposite directions in the non-local subset K_A, and symmetrically with respect to the y-z plane in the near-neighbor subset K_B. The decoherence can be readily grouped by the two different mechanisms as

$$\mathcal{L}^{\rm s}_{+,-} \cong \prod_{k\in K_B} e^{-\frac{t^4}{2}E_k^2 B_k^2 {\rm sinc}^4\frac{h_k t}{2}} \prod_{k\in K_A} e^{-2t^2 A_k^2 {\rm sinc}^2(h_k t)}, \tag{B14}$$

where $h_k = |\mathbf{h}^{\pm}_k|$ and ${\rm sinc}(x) \equiv \sin(x)/x$.

In III–V QDs, because of the large number of nuclear spins, the loss of electron spin coherence is much faster than the build-up of higher order nuclear spin correlations. The decoherence is therefore well-described by the pair correlation approximation as given in Equation (B14). In other systems, such as Si or diamond NV centres with a dilute nuclear spin bath, corrections from higher order nuclear spin correlations become important [129,220–222].

Lattice distortion can result in local electric field gradients, inducing the quadrupole interaction for nuclear spins with moment greater than 1/2. Recent experimental works have indeed demonstrated signatures of quadrupolar interactions for nuclear spins in InAs self-assembled dot [366,367]. The quadrupolar interaction can be well-incorporated in the theory described in this appendix as contributions to energy cost for nuclear pair flips (i.e. the D_k term in Equation (B12)] when reliable parameter is extracted from experiments. We expect

that quadrupolar interaction does not affect electron spin free induction decay and Hahn echo decay where the D_k term is unimportant, but may affect Carr–Purcell echoes and spin echoes by complex pulse sequences when the D_k term plays a non-negligible role [127,130,134,221].

Appendix C. Quantum measurement in Shor's algorithm

We show the crucial role of QND measurement for quantum computation to be scalable by explicitly examining Shor's algorithm.

C.1. Order finding for Shor's algorithm

For the reader's convenience, we give a brief review of the algorithm for finding the order of a number, the core subroutine for Shor's algorithm. For a comprehensive description of the algorithm, the reader is referred to Ref. [172]. The order r of a number x with respect to a number N is defined by the relation $x^r = 1 \bmod N$. For $2^{L-1} \leq N < 2^L$ and $1 < x < N$, the task is to find r with resources at most polynomial to L.

The observation is that $f(n) \equiv x^n \bmod N$ is periodic with period r, i.e. $f(n+r) = f(n)$, indicating a QFT may be used to find the spectrum of this function and thus to find r. The algorithm is outlined as follows.

(1) Two registers with t and L qubits, respectively, are zeroed initially, and thus the initial state is,

$$|00\cdots0\rangle|00\cdots0\rangle.$$

(2) The QFT is applied to the first register to obtain the state,

$$\frac{1}{\sqrt{2^t}}\sum_{n=0}^{2^t-1}|n\rangle|00\cdots0\rangle,$$

where $n = b_1 b_2 \cdots b_t$ is a binary number with $b_i = 0$ or 1.

(3) With the advantage of quantum parallelism, one evaluation of the function $f(n)$ is added to the second register to reach the state

$$\frac{1}{\sqrt{2^t}}\sum_{n=0}^{2^t-1}|n\rangle|x^n \bmod N\rangle.$$

By $f(n) = f(n+r)$, the state can be rewritten as,

$$\frac{1}{\sqrt{2^t}}\sum_{k=0}^{r-1}\sum_{l=0}^{[(2^t-k)/r]}|k+lr\rangle|x^k\rangle,$$

where $[n/m]$ denotes the greatest integer not greater than n/m. Such an expression suggests a solution of the spectrum by QFT.

(4) After an inverse QFT applied to the first register, the state becomes,

$$\frac{1}{2^t}\sum_{j=0}^{2^t-1}\sum_{k=0}^{r-1}\sum_{l=0}^{[(2^t-k)/r]}e^{-i2\pi\frac{(k+lr)j}{2^t}}|k+lr\rangle|x^k\rangle.$$

If 2^t happens to be an integer multiple of r, the terminating state is just,

$$\frac{1}{r}\sum_{s=0}^{r-1}\sum_{k=0}^{r-1}e^{-i2\pi ks/r}|2^t s/r\rangle|x^k\rangle,$$

only for $j = 2^t(s/r)$ will the amplitude be nonzero. Generally, r would not divide 2^t, but if 2^t is much larger than r, the spectrum after the QFT will be distribution composed of peaks around $2^t(s/r)$ for $(0 \le s < r)$. The larger the first register, the sharper the peaks are. The probability of the state of the first register being away from $2^t\ s/r$ by a distance 2^p is calculated to be less than $1/(2^{p+1}-4)$, so with probability greater than $1-1/(2^{p+1}-4)$, the fraction s/r can be determined up to the first $t-p$ bits by a measurement of the first $t-p$ bits of the first register. If $t-p$ is chosen to be $2L+1 \equiv N$, r can be determined from the first N bits of the binary fraction number s/r, i.e. $[2^N\ s/r]$, by continued fraction.

C.2. Issues with the measurement

The key feature of Shor's algorithm is that, though the terminating state is a superposition of many computational basis states $\sum_x |x\rangle$ (where $|x\rangle = |b_1 b_2 \cdots b_t\rangle$ with $b_i = 0$ or 1), it is not necessary to know all the amplitudes to solve the problem. Actually, an ideal measurement on the computational basis will project the superposition state into an arbitrary basis state which has a nonzero amplitude, and with high probability, the fraction s/r can be determined up to $2L+1$ bits. If the measurement is performed in a single shot, the register may be read out bit by bit, and the superposition state will collapse in a cascade manner, so the resource required by the whole readout step is $O(L)$ and thus the measurement is scalable. The cascading readout can be illustrated by the example of reading the state $|000\rangle + |010\rangle + |110\rangle + |111\rangle$, in which the state collapse may follow the steps shown in Figure C1. Only N single-bit measurements are required to have an N-bit superposition state collapsed into a basis state and only N bits of classical memory are needed to record the measurement result. So a single-shot measurement on a single quantum register needs less resources than polynomial to the problem size in Shor's algorithm.

C.3. Ensemble measurement

Now we will show, that, in Shor's algorithm, an ensemble measurement requires resources increasing exponentially with the size of the problem. The terminating state of Shor's algorithm can be written as,

$$\frac{1}{r}\sum_{k=0}^{r-1}\sum_{s=0}^{r-1}\left|\widetilde{s/r}\right\rangle \otimes \left|R(s,k)\right\rangle \otimes \left|x^k\right\rangle,$$

where $\widetilde{s/r}$ denotes the first N binary bits of s/r, and $R(s, k)$ denotes the state of the last p bits of the first register which are not accurate in describing s/r. Only the first N bits of the first register need to be measured. The detected probability is uniformly distributed among the r states $|\widetilde{s/r}\rangle$, which are spaced almost equally by the distance $2^t/r$.

C.3.1. Correlated measurement

Suppose the first N qubits of the first register are measured with coincidence counting. Each basis state $|b_1 b_2 \cdots b_N\rangle$ could lead to a click in a corresponding channel. To accumulate confidence in an ensemble measurement, a channel should get at least two clicks. In each single-shot trial of the measurement ensemble, the state would collapse into different states. Each output has to be recorded and stored before one of them is confirmed. So the number of recording channels and the size of classical memories used for data storage scale as 2^N, exponentially increasing with the problem size in Shor's algorithm. This requires exponentially increasing physical resources such as spectral resolution or spectrometer bandwidth in spectroscopy.

If the number of available channels and classical memory registers are limited by C we may randomly or uniformly choose C x's from the 2^N possible numbers. What is the chance that we can receive a signal at any one of these C channels? As the probability of having a signal in an arbitrary channel is $\sim 2^{-N}$, the probability of having signal in any of the C

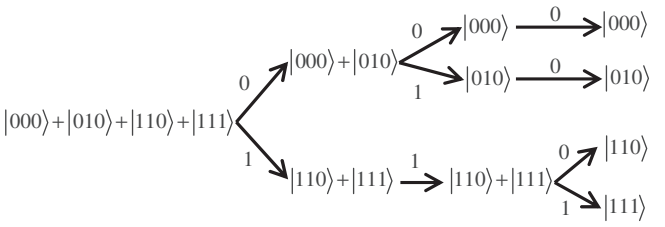

Figure C1. The collapse (quantum jump) of a multi-qubit state under a measurement of the qubits in sequence. The number associated with each arrow indicates the output of the measurement.

channels is $P_C = 2^{-N}\, C$. So, for any finite probability P_C, the number of channels needs to be $C \sim 2^N\, P_C$, increasing exponentially with the problem size.

C.3.2. Uncorrelated measurement

In an uncorrelated measurement of an N-qubit register, the ensemble is first divided into $4^g(N/g)$ portions (g is a fixed small integer), and every 4^g portions can be used for 4^g independent g-qubit measurements to obtain the density matrix of these g qubits. Once the reduced density matrices for all the g-qubit subsystems have been obtained, one could apply some classical algorithm to re-construct the density matrix of the N qubits. The re-construction, of course, could not be certain, but the uncertainty nonetheless does not exclude the possibility that one might search for a correct result from all possible states which give the reduced matrix elements. The number of measurements, the number of recording channels and the size of storage, all these resources scale only linearly with the problem size.

However, there is a fundamental problem underlying the uncorrelated measurement strategy: to yield an N-qubit output, essentially N bits of information have been generated. To generate the same amount of information, the g-qubit reduced density matrices have to be measured with $N - \ln(N/g)$ bit accuracy. By the rule of thumb in experimental physics, measuring any physical quantity with N-qubit precision would require resources scaling as 2^N. Only in exceptional cases may the register state be derived from the knowledge of the reduced density matrices. For instance, if all one-qubit density matrices are pure states, the register state is obviously the outer product of all of them. But in general, it is difficult to determine the register state from the one-qubit density matrices. For example, if all the N qubits are maximally entangled with other qubits, such as in the states,

$$|0000\rangle + |0011\rangle + |0110\rangle + |1001\rangle + |1100\rangle + |1111\rangle,$$

and

$$|0000\rangle + |0101\rangle + |1010\rangle + |1111\rangle$$

the uncorrelated measurement would turn out to be N maximally mixed density matrices in both cases, from which little information can be obtained about the register state. To determine the order r, one has to search from all possibilities, of which the number is $\sim 2^N$.

Below we will show that, for the first N qubits in Shor's algorithm, there are $\sim 2^N$ possible terminating states which would produce almost the same one-qubit reduced density matrix.

Lemma C.1: *For a state* $\sum_{l=0}^{[(2^N-1)/k]} |lk\rangle$ (k *is an odd number greater than* 1), *the reduced density matrix of any qubit has no off-diagonal term in the computational basis.*

Proof: If there is an off-diagonal term $\langle 0|\rho|1\rangle$ for the jth qubit, there have to be at least two states $|x\rangle$ and $|x'\rangle$ in the superposition, which are different only at the jth bit. So we have that $|x - x'| = 2^{n-j}$ is divided by k, which is impossible since k is an odd number □

Corollary C.2: *For the state* $\sum_{l=0}^{\lceil (2^N-1)/(2^p k)\rceil} |l2^p k\rangle$ (k *is an odd number greater than* 1), *the reduced density matrix of any qubit has no off-diagonal term in the computational basis, and the reduced density matrices of the last p qubits are all* $|0\rangle\langle 0|$.

Corollary C.3: *For the state* $\sum_{l=0}^{\lceil (2^N-1)/2^p\rceil} |l2^p\rangle$, *the reduced density matrices of the first* $n-p$ *qubits are all* $(|0\rangle+|1\rangle)\frac{1}{2}(\langle 0|+\langle 1|)$, *and the reduced density matrices of the last p qubits are all* $|0\rangle\langle 0|$.

Lemma C.4: *For the state* $\sum_{l=0}^{\lceil (2^N-1)/k\rceil} |lk\rangle$, *if the odd number* $k < 2^{\alpha N/2}$ *for a specific number* $\alpha \in (0,1)$, *the states* $|x\rangle$ *with* $x_j = 0$ *or 1 have the same probability up to cN-bit precision to occur in the superposition, where c is a constant less than 1.*

Proof: The integer numbers $x = \{x_1 x_2 \cdots x_N\}$ with $x_j = 0$ or 1 form alternatively 2^j segments with length 2^{N-j}. For an arbitrarily chosen number $\beta \in (\alpha, 1)$, the segment length 2^{N-j} is either less or greater than $2^{\beta N/2}$. If $2^{N-j} > 2^{\beta N/2}$, as the number of the multiples of k in a segment is greater than $2^{(\beta-\alpha)N/2}$. The numbers of multiple k in two neighboring segments differ by at most 1. So the occurring probability of $x_j = 0$ is different from that of $x_j = 1$ by at most $1/2^{(\beta-\alpha)N/2}$. If $2^{N-j} \le 2^{\beta N/2}$, we observe that the first x of every k segments is $k2^{N-j}$, a multiple of k. As k is an odd number, each k segments starting with $x_j = 0$ will be followed by k segments starting with x_j=1, and vice versa, until the end of all segments. So, in every $2k$ segments, the numbers of lk's with $x_j = 0$ or 1 are exactly the same. As the difference of the occurring numbers in 2 neighboring segments is at most 1, the difference in k segments is at most $(k+1)/2$. So, the difference of the occurring probability in all the segments is at most $(k+1)2^{N-j}/2^{N+1} < 1/2^{N(1-\alpha/2-\beta/2)}$. Let $c = \min(1-\alpha/2-\beta/2,\ \beta/2-\alpha/2)$, we have the probability of occurring of $x_j = 0$ is the same as that of occurring of $x_j = 1$, accurate up to cN bits □

From Lemmas 1 and 2, we directly have the following theorem.

Theorem C.5: *For all states* $\sum_{l=0}^{\lceil (2^N-1)/k\rceil} |lk\rangle$ (k *is an odd number, and* $k < 2^{\alpha n/2}$ *for a specific number* $\alpha \in (0,1)$), *all one-qubit reduced density matrices obtained by uncorrelated measurements are the same up to cN significant bits.*

Corollary C.6: *For all states* $\sum_{l=0}^{\lceil (2^N-1)/(2^p k)\rceil} |l2^p k\rangle$ (k *is an odd number, and* $k < 2^{\alpha N/2}$ *for a specific number* $\alpha \in (0,1)$), *all one-qubit reduced density matrices obtained by uncorrelated measurements are the same with cN significant bits.*

The theorem and corollary above are consistent with a theorem recently proved by Popescu *et al.* [368]: almost all N-qubit states would give almost the same g-qubit reduced density matrix, as long as N is large and $N \gg g$.

The terminating states of the register to be measured in Shor's algorithm have the form of the superposition states in the theorem above, with at most one-bit deviation. So, unless at least the density of matrix of one qubit is measured with $O(N)$ effective bits, there are $\sim 2^N$ possible superpositions corresponding to the same set of one-qubit reduced density matrices. On the one hand, searching the correct one from all those possibilities needs resources $\sim 2^N$ in all known classical or quantum algorithms. On the other hand, determining the density matrix of a qubit with $O(N)$-bit accuracy also requires resources $\sim 2^N$. So uncorrelated single-qubit ensemble measurement is provably unscalable for Shor's algorithm. Though there is no proof in general cases, it would be rather surprising that some ensemble measurement scheme is scalable for Shor's algorithm.

C.4. Single-object measurement with error

In general, scalable quantum computation needs to be performed on a single quantum object (rather than an ensemble) with single-shot measurement. In reality, detectors used in the readout procedure have unavoidable inefficiency or errors. Thus, the Kraus operators [172] for a POVM of a certain qubit can be written as

$$A_0 = \sqrt{1-d}|0\rangle\langle 0| + \sqrt{1-e}|1\rangle\langle 1|, \tag{C1a}$$

$$A_1 = \sqrt{d}|0\rangle\langle 0| + \sqrt{e}|1\rangle\langle 1|, \tag{C1b}$$

with detector efficiency e and dark count rate d. For a state $|\psi\rangle$, the probability and the resultant state for the output 0 and 1 are, respectively,

$$P_0 = \langle\psi|A_0^\dagger A_0|\psi\rangle \quad \text{and} \quad A_0|\psi\rangle, \tag{C2a}$$

$$P_1 = \langle\psi|A_1^\dagger A_1|\psi\rangle \quad \text{and} \quad A_1|\psi\rangle. \tag{C2b}$$

Suppose that the detecting error rate at each qubit is greater than a finite number ε, the probability of reading out a N-qubit register is less than $(1-\varepsilon)^N$, exponentially small with increasing size of the register. A single-shot measurement is then insufficient for scalable quantum computation. Thus, if there exist detector errors as always, the measurement has to be repeated enough times to obtain sufficient confidence in a readout result. Furthermore, if the measurement is destructive, the quantum computation has to be rewound from the very beginning of the algorithm, making the measurement equivalent to an ensemble measurement.

In an uncorrelated measurement, different qubits of the register are measured and recorded independently, and the error rate at each bit is finite, so the density matrices of each qubit of the register can be measured by repeating the quantum computation for a number of times proportional to the register size. But the problem here is the same as discussed for the uncorrelated measurement in the previous section.

In a correlated measurement, the probability of correctly reading out the projected state is exponentially small [$\sim (1-\varepsilon)^N$], and yet the probability of the terminating state collapsing into the same basis state is also exponentially small ($<1/r$). So before a readout result is repeated once for accumulating sufficient confidence, the quantum computation has to be repeated a number of times which increases exponentially with the problem size.

C.5. QND measurement

In a QND measurement, the state will remain unchanged after the projection into the measurement basis (which is also the computational basis). So the readout can be repeated many times in every qubit to accumulate confidence of the readout result, without rewinding the whole algorithm from the beginning.

Now we calculate the resources required in reading out the state of an N-qubit register. If the error rate in reading out each qubit by an M-shot QND measurement is ε_M, the probability of successfully reading out the register is $(1-\varepsilon_M)^N$. To have a finite success probability, we require $s_N \equiv (1-\varepsilon_M)^N > s$ where s is a finite number smaller than 1. When ε_M is small, $s_N \approx e^{-N\varepsilon_M}$, so we require the error rate of a M-shot QND measurement $\varepsilon_M < -(1/N)\ln s$.

To obtain the error rate of a M-shot measurement, we define its POVMs. The Kraus operators for the POVM of a M-shot measurement giving m photon counts can be derived as,

$$\begin{aligned} A_{M,m} &= \binom{M}{m}^{1/2} (1-d)^{(M-m)/2} d^{m/2} |0\rangle\langle 0| \\ &\quad + \binom{M}{m}^{1/2} (1-e)^{(M-m)/2} e^{m/2} |1\rangle\langle 1| \\ &\equiv \sqrt{d_{M,m}}|0\rangle\langle 0| + \sqrt{e_{M,m}}|1\rangle\langle 1|. \end{aligned} \tag{C3}$$

When $d_{M,m} < e_{M,m}$, it is more probable that the qubit is in the state $|1\rangle$, and vice versa. As

$$d_{M,m}/e_{M,m} = \left(\frac{1-d}{1-e}\right)^M \left[\frac{d(1-e)}{e(1-d)}\right]^m \tag{C4}$$

monotonically decreases with m, we can define a m_0 so that all $A_{M,m<m_0}$ are indicators of $|0\rangle$ and all $A_{M,m>m_0}$ are indicators of $|1\rangle$, with the m_0 given by $d_{M,m_0}/e_{M,m_0}=1$ or,

$$m_0 = \frac{M \ln \frac{1-d}{1-e}}{\ln \frac{1-d}{1-e} + \ln \frac{e}{d}} \equiv \alpha M. \tag{C5}$$

As $d_{M,m}$ and $e_{M,m}$ as functions of m have peaks at dM and eM, respectively, we have,

$$d < \alpha < e. \tag{C6}$$

Now the POVM can be calculated from,

$$P_0^{(M)} \equiv \sum_{m<m_0} A_{M,m}^{\dagger} A_{M,m} \equiv (1-d_M)|0\rangle\langle 0| + (1-e_M)|1\rangle\langle 1|,$$
$$P_1^{(M)} \equiv \sum_{m\geq m_0} A_{M,m}^{\dagger} A_{M,m} \equiv d_M|0\rangle\langle 0| + e_M|1\rangle\langle 1|,$$

where

$$\begin{aligned} d_M &= \sum_{m\geq m_0} d_{M,m} = \sum_{m\geq m_0} \binom{M}{m} (1-d)^{M-m} d^m \\ &= \frac{M!}{(M-m_0)!(m_0-1)!} \int_{1-d}^{1} t^{M-m_0} (1-t)^{m_0-1} \mathrm{d}t \\ &< \frac{M!(1-d)^{M-m_0} d^{m_0}}{(M-m_0)!(m_0-1)!} \\ &\sim \sqrt{\frac{\alpha M}{2\pi(1-\alpha)}} \left[\frac{(1-d)^{1-\alpha} d^{\alpha}}{(1-\alpha)^{1-\alpha} \alpha^{\alpha}} \right]^M, \end{aligned} \tag{C7}$$

and similarly,

$$1 - e_M < \sqrt{\frac{\alpha M (1-e)^2}{2\pi(1-\alpha)e^2}} \left[\frac{(1-e)^{1-\alpha} e^{\alpha}}{(1-\alpha)^{1-\alpha} \alpha^{\alpha}} \right]^M. \tag{C8}$$

The error rate is defined as $\varepsilon_M = \max(d_M, 1-e_M)$, so the number of required QND measurements per qubit $M \sim \ln N$, and the total number of measurement is proportional to $N \ln N$. So a QND is scalable. In experiment, e and d cannot be determined exactly, but fortunately α need not be determined exactly and whenever it is between d and e, the results for d_M and e_M are unchanged in the equations above.

Note that with the aid of entanglement gates and a supply of fresh qubits, a destructive measurement can be converted into a QND one. The idea is based on the transformation of a qubit and M zeroed auxiliary qubits into an entangled state by M entanglement gates:

$$(\alpha|0\rangle + \beta|1\rangle) \bigotimes_{m=0}^{M-1} |0\rangle \Longrightarrow \alpha|0\rangle \bigotimes_{m=0}^{M-1} |0\rangle + \beta|1\rangle \bigotimes_{m=0}^{M-1} |1\rangle.$$

The M auxiliary qubits are to be read out. As all these qubits are entangled, once one qubit is collapsed into a basis state $|0\rangle$ or $|1\rangle$, all the qubits will be collapsed into the same state. So even a destructive measurement with detecting error can be used to read out the qubit.

How about a QND measurement with back-action noise, i.e. reaction to measurement that disturbs the state after a measurement cycle? With the idea above for converting destructive measurement into a QND one, we can employ the concept of *fault-tolerant measurement* to deal with this problem. In the so-called fault-tolerant measurement, a qubit is first encoded into a stabilizer code, after a single measurement, any back-action noise will be diagnosed and corrected using the error syndrome since this noise acts only on a single qubit (by assumption). After the error correction, another measurement would be performed, and so on.

The fault-tolerant measurement thus allows an imperfect QND measurement to read out the result of a quantum algorithm with polynomial resources.

Appendix D. Elementary quantum gates

Here we define a series of elementary quantum gates used in the quantum circuits presented in Section 8.1. The quantum gates of interest are defined in Figure D1 and D2. The Hadamard gate can be realized by the spin rotation operations up to a trivial global phase, as the transformation operator for the Hadamard gate can be expressed in terms of spin rotations as $H = e^{i\pi/2}\, e^{i\pi s_z}\, e^{i\pi s_y/2}$. The CNOT gate can be realized by the controlled π-phase gate together with two Hadamard gates. The CNOT gate on two remote bits can be realized by a local CNOT gate plus some SWAP gates. The doubly controlled NOT (Toffoli) gate can be realized by six CNOT gates plus some single-qubit gates. The controlled π-phase gate and the CNOT gate can be realized by two $\sqrt{\text{SWAP}}$ gates plus some single-spin rotations. As any controlled phase gate can be realized by two CNOT gates plus some single-qubit gates, the circuits in Figure 38 and 39 can be alternatively realized with $\sqrt{\text{SWAP}}$ gates as well.

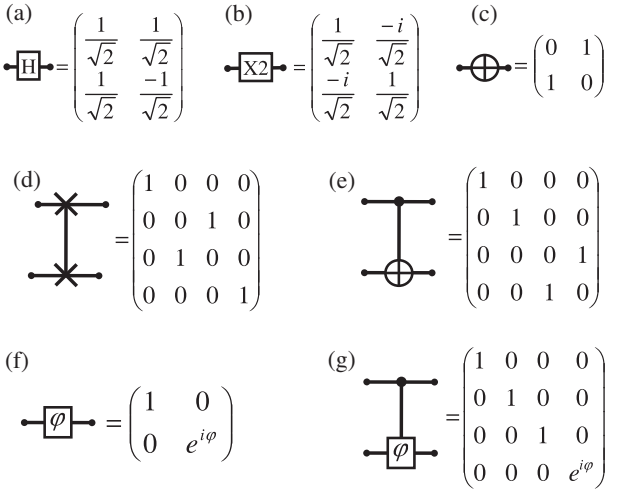

Figure D1. Some elementary quantum gates and their matrix representation, including (a) Hadamard (H), (b) rotation of 90° about the x-axis ($X2$), (c) NOT (N), (d) SWAP (W), (e) controlled NOT (C), (f) single-bit phase-shift (S_ϕ) and (g) controlled phase-shift (P_ϕ).

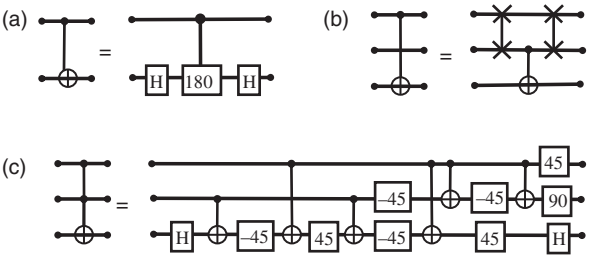

Figure D2. Realization of several control gates, including (a) CNOT, (b) remote CNOT and (c) Toffoli (C_2).